

N72-25755-804

NASA SP-295

# SIGNIFICANT ACCOMPLISHMENTS IN TECHNOLOGY

*Goddard Space Flight Center, 1970*

## CASE FILE COPY

A symposium held at  
**GODDARD SPACE FLIGHT CENTER**

January 13, 1971



**NATIONAL AERONAUTICS AND SPACE ADMINISTRATION**

# SIGNIFICANT ACCOMPLISHMENTS IN TECHNOLOGY

GODDARD SPACE FLIGHT CENTER, 1970

The proceedings of a symposium held at NASA  
Goddard Space Flight Center, January 13, 1971

*Prepared by Goddard Space Flight Center*



Scientific and Technical Information Office  
NATIONAL AERONAUTICS AND SPACE ADMINISTRATION  
Washington, D.C.

1972

---

For sale by the National Technical Information Service,  
Springfield, Virginia 22151  
Price \$3.00

## **PREFACE**

The requirement that SI (metric) units be employed in NASA Publications has been waived by the Director, GSFC, under the authority of subparagraphs 5.b and 5.d of NASA Policy Directive 2220.4.

## FOREWORD

This document presents the collection of papers on technological achievements delivered at the annual science and technology review at Goddard Space Flight Center (GSFC) on January 13, 1971. The overall objective of the technology review was the presentation, to a selected audience, of a summary of the major technological advances achieved at GSFC during the past year. The specific objectives of the individual papers varied; but in most cases, they were dedicated to the description of advances which have unique applications. The texts of the papers here are substantially as given; but in some cases, where the subjects were more complex and where more detailed papers have been prepared for publication, the more detailed papers are included.

The audience to whom this presentation was made was comprised of technologically oriented engineers and scientists who have interest in and, in many cases, responsibility for the direction of space application research and development. In addition to the many GSFC scientists and engineers who had an interdisciplinary interest in the progress reported, members of the audience came from the NASA Headquarters Organization, other NASA centers, and other government laboratories.

The 50 papers presented were selected competitively from a center-wide submission of some 115 candidate papers. The selection criteria employed included (1) significance of accomplishment, (2) currentness of accomplishment, i.e., the work was accomplished during the past year, (3) uniqueness of accomplishment, (4) relative immediacy of application, and (5) the extent to which the author was involved. Selection was made during a series of oral reviews by the Technology Review Committee, chaired by Mr. Robert J. Mackey, Jr., and including Mr. Eugene W. Wasielewski, Mr. William G. Stroud, Dr. Henry H. Plotkin, Mr. Raymond Kruger, Mr. John Mangus, Dr. William S. West, and Mr. James M. Bridger.

Mr. Bridger was responsible for coordination of paper selection operations and for documentation and editing of the review proceedings.

## CONTENTS

Preface . . . . .	iii
Foreword . . . . .	v
Opening Remarks <i>John F. Clark</i> . . . . .	1
Introduction to the Technology Section <i>Daniel G. Mazur</i> . . . . .	2
Radio Wave Propagation Experiments to Probe the Ionosphere <i>P. E. Schmid</i> . . . . .	3
Comparison of Satellite Theories <i>H. G. Hertz</i> . . . . .	10
An Analysis of the Expected Eccentricity Perturbations for the Second Radio Astronomy Explorer (RAE B) <i>James P. Murphy</i> . . . . .	14
Dynamical In-Orbit Behavior of the Radio Astronomy Explorer Satellite <i>Harvey Walden</i> . . . . .	18
Future Techniques for Tracking of Synchronous Satellites <i>James L. Cooley</i> . . . . .	23
The Geopotential at Synchronous-Orbit Altitudes <i>C. A. Wagner</i> . . . . .	26
In-Orbit Flexible Spacecraft Dynamics Program <i>Joseph V. Fedor</i> . . . . .	30
Structural-Thermal-Optical Program (STOP) <i>H. P. Lee</i> . . . . .	36

Two-Dimensional Finite-Element Temperature Variance Analysis <i>J. S. Heuser</i> . . . . .	41
A Rotary Actuator for Space Missions <i>E. J. Divine</i> . . . . .	45
Hybrid Circuit Modules for Motor Commutation and Control <i>C. deKramer</i> . . . . .	48
Automatically Activated, 300 Ampere-Hour Silver-Zinc Cell <i>Thomas J. Hennigan</i> . . . . .	52
Screening and Selection of Nickel and Cadmium Cell Plates to Improve Uniformity <i>Gerald Halpert</i> . . . . .	56
The Degradation of Alzak by Short Wavelength Ultraviolet Radiation <i>Martin J. Donohoe, Roy McIntosh, Jr., and John H. Henninger</i> . .	59
Spacecraft Radiation Analysis <i>Dale W. Harris</i> . . . . .	67
A 10.6-Micrometer Laser Receiver RF Subsystem <i>D. E. Santarpia</i> . . . . .	71
Ku-Band High Gain Antenna <i>Leonard F. Deerkoski</i> . . . . .	74
Discrete Component S-Band Power Amplifier <i>Arthur F. Block</i> . . . . .	79
Flight Data Subsystems Using LSI P-Channel MOSFETS <i>James H. Trainor</i> . . . . .	82
Telemetry Remote Modules <i>J. R. Silverman</i> . . . . .	87
An On-Board Processor (OBP) for OAO C <i>Raymond Hartenstein</i> . . . . .	90

The Nimbus 4 IRLS Meteorological Experiment <i>Charles E. Cote</i> . . . . .	96
Millimeter Wave Propagation Measurements Using the ATS 5 Satellite <i>Louis J. Ippolito</i> . . . . .	100
Glancing Incidence Telescopes for Space Astronomy <i>John D. Mangus</i> . . . . .	103
A Computer Program to Evaluate Optical Systems <i>Daphne Innes</i> . . . . .	107
Multispectral Image Dissector Camera System <i>Bernard L. Johnson</i> . . . . .	111
Precision Digital Solar Aspect Sensor <i>H. P. Scherer</i> . . . . .	115
An Adaptive Narrow Band Frequency Modulation Voice Communication System <i>Sheldon Wishna</i> . . . . .	119
Computer-Aided CO <sub>2</sub> -Laser Cavity-Length Selection for Reduced Line Competition <i>G. Schiffner</i> . . . . .	122
Results of FM-TV Threshold Reduction Investigation for the ATS F TRUST Experiment <i>James P. Brown</i> . . . . .	126
Radiation Damage Effects on Solid State Detectors <i>James H. Trainor</i> . . . . .	129
Revised Standards for the Solar Constant and the Solar Spectrum <i>M. P. Thekaekara</i> . . . . .	133
A Computer Program to Automate Residual Gas Analysis <i>H. Shapiro</i> . . . . .	138

Experimental Thermal Mechanics of Deployable Boom Structures <i>Roamer Predmore</i> . . . . .	140
Design and Development of a Micropound Extended Range Thrust Stand (MERTS) <i>Kenneth W. Stark</i> . . . . .	145
Ultra-Precise Attitude Test Facility for Flight Spacecraft <i>E. J. Devine</i> . . . . .	148
Improved Laser Ranging Accuracy Through Dynamic Threshold Compensation <i>T. S. Johnson</i> . . . . .	152
STADAN Antenna Gain Calibration Using Radio Stars <i>Ralph E. Taylor</i> . . . . .	156
Computer Controlled Antenna System <i>Nicholas A. Raumann</i> . . . . .	159
Dichroic Subreflector for Rosman II <i>Julius A. Kaiser</i> . . . . .	163
Signal Coherence Studies in Multiaperture Arrays <i>Leonard F. Deerkoski</i> . . . . .	167
The NAS-PAK Logic System <i>James Billingsley</i> . . . . .	171
Simulation of Mass Storage Systems Operating in a Large Data Processing Facility <i>Richard Holmes</i> . . . . .	181
Feasibility Model of a Video Instrumentation Record/Reproduce System <i>J. L. Tinsley</i> . . . . .	183
ART/SRT Report on APL <i>Cyrus J. Creveling</i> . . . . .	187

Automated Detection of Bacteria in Urine <i>Albert J. Fleig, Grace L. Picciolo, Emmett W. Chappelle, and Burton N. Kelbaugh</i> . . . . .	188
The Heart Sound Preprocessor <i>Wayne T. Chen</i> . . . . .	193
Long Range Laser Traversing System <i>Louis O. Caudill</i> . . . . .	196
Using the Scanning Electron Microscope on the Production Line to Assure Quality Semiconductors <i>John W. Adolphsen and Robert J. Anstead</i> . . . . .	199
Ultraprecision Tool Positioner <i>Ewald E. Schmidt</i> . . . . .	203

## **OPENING REMARKS**

**Dr. John F. Clark, Director**

Good morning, ladies and gentlemen. Welcome to our annual review of accomplishments in technology. The organization of our presentation is quite similar to that employed last year; we have taken the liberty of switching the order of the Science and Technology portion of the presentation: the Technology portion will be presented today, the Science portion tomorrow. As in previous years, some of the fruits of our technological efforts are exhibited around the walls of this room and in the foyer. These exhibits will be manned during the intermissions to answer any questions you may have.

We believe that we have organized a program for today which you will find to be both interesting and informative. It is a very full program, so without further ado, I am introducing Mr. Daniel Mazur, our Director of Space Applications and Technology, who will chair today's session.

## INTRODUCTION TO THE TECHNOLOGY SESSION

**Daniel G. Mazur**

Good morning, ladies and gentlemen. We have selected about 50 papers for presentation in today's session. These 50 papers have come from all those divisions of GSFC that are engaged in technological development and should give you a fairly good overview of our effort during the past year. These papers have been scheduled to allow for questions from the floor. We hope that you will ask questions; we ask that they be held until the end of the paper so as not to interrupt the development of the author's thought.

The papers have been grouped by technological areas insofar as possible. The technological areas included are much the same as we employed last year. "Spinoff" or "fallout" or, to use the official term, technology utilization is assuming an increasingly important aspect in our effort to achieve maximum utilization of our technological advances. We have included at the end of today's session five papers that are representative of our technology utilization effort.

## **RADIO WAVE PROPAGATION EXPERIMENTS TO PROBE THE IONOSPHERE**

**P. E. Schmid**

The Earth's ionosphere biases all measurements associated with radio tracking of spacecraft because the velocity of radio waves in the ionosphere differs from that in free space. The integrated effect of this velocity difference is directly proportional to the total number of electrons in a unit cross-section tube along the ray path connecting spacecraft and tracking station. All tracking measurement ionospheric biases can be shown to be directly proportional to this "integrated electron content" and inversely proportional to the square of transmission frequency. This paper briefly discusses three techniques which have proved highly successful in measuring integrated electron content.

The three techniques are

1. Faraday rotation measurements from an Earth synchronous satellite.
2. Ranging measurements at two frequencies.
3. Group and phase velocity measurements obtained from tracking data.

The third scheme (see Reference 1) is the most desirable because measured corrections pertain directly to the spacecraft whose orbit or trajectory is being determined. Similar work has been performed for deep space applications at the Jet Propulsion Laboratory (JPL) where group and phase velocity differences through ionized media are used in their so-called "charged particle calibrations" (Reference 2).

Such ionospheric corrections are of special importance in the case of VHF tracking. From the standpoint of spacecraft and ground antenna simplicity and the related ease of signal acquisition (because of antenna beamwidth relationships), 136 to 148 MHz is still a highly desirable

frequency range for tracking and subsequent orbit computation of low-power, low-data-rate, Earth and near-Earth orbiting spacecraft. Such approved future VHF missions include the Radio Astronomy Explorer B (RAE B), the Synchronous Meteorological Satellite (SMS), and the continuing Explorer series of spacecraft.

Figure 1 shows Faraday rotation data recorded at Goddard Space Flight Center from an Earth synchronous satellite, ATS 3, during the March 7, 1970, solar eclipse. The measured polarization twist is a function of both the integrated electron content and the Earth's magnetic field. Since the Earth's magnetic field is well established, the observed Faraday rotation from ATS 3 at 137.350 MHz is directly related to changes in integrated electron content and hence to changes in ionospheric biases in tracking data. By the use of ionosphere bottom sounding data from Wallops Island, the absolute (i.e., total unambiguous) number of polarization rotations was noted during the eclipse. These data indicated that the content dropped from  $6 \times 10^{17}$  to  $4.5 \times 10^{17}$  electron/m<sup>2</sup> as the lunar shadow passed through the ionosphere. This corresponds to a range bias change of approximately 500 m at 140 MHz.

The lower portion of Figure 1 shows a normal buildup in ionization peaking at approximately 3:15 p.m. local time at a level on the order of  $10^{18}$  electron/m<sup>2</sup>. The upper portion of Figure 1 shows the same type of display with the exception of the abrupt decrease in electron content (phase reversal at approximately 12 noon), which then recovered to the normal diurnal cycle at 2:20 p.m. to reach the afternoon peak integrated density at 3:30 p.m. All times are local (i.e., Eastern Standard Time).

Figure 2 shows a comparison of range bias determined by Faraday rotation from ATS 3 and that determined by ranging to ATS 3 at two widely separated frequencies. In this case, the frequencies are nominally 140 MHz and 6000 MHz. The range bias is given by

$$\Delta R = \frac{40.3I}{f^2} - \frac{40.3I_v}{f^2 \sin E} \quad (\text{m}), \quad (1)$$

where

$I$  = total integrated electron content along ray path (electron/m<sup>2</sup>),

$f$  = frequency (Hz),

$E$  = local elevation angle of ray intercept point at 300-km height (i.e., height of maximum ionization),

$I_v$  = vertical integrated content in column intersecting 300-km intercept point (electron/m<sup>2</sup>).

For elevation angles above 45 deg,  $E$  can usually be taken as the ground-measured elevation angle to the spacecraft. For lower angles, Earth curvature should be taken into account:

$$E = \arccos \left( \frac{a}{a+h} \cos E' \right), \quad (2)$$

where

$a$  = Earth radius,

$h$  = 300 km (or height of maximum electron density if known more accurately),

$E'$  = elevation angle as measured by tracking station.

Figure 2 shows clearly the diurnal variation in electron content at Rosman, North Carolina, with the typical midafternoon peak occurring at approximately 2:00 p.m. local time. The difference between Faraday data and range difference data in this preliminary test is attributed primarily to the ATS 3 VHF transponder time delay uncertainty. Further tests are being conducted to improve calibration techniques.

The most desirable way to obtain group and phase velocity information, from an operational standpoint, is to extract integrated electron content information and hence ionospheric bias corrections directly from the tracking data. Figure 3 shows that this can be achieved by the comparison of range-rate measurements based on carrier Doppler shift with differentiated range measurements based on tone delay.

Simply stated, the ionosphere biases range-rate in one direction and biases the differentiated range an equal amount in the opposite direction. Thus, the true range rate is halfway between the two curves shown in Figure 3. The reason for this phenomenon is that the Doppler phase is altered by the phase velocity and the range delay is altered by the group velocity. In a

dispersive media like the ionosphere, the group and phase velocities differ in a predictable manner.

The same technique is used by JPL in their charged particle calibration, with one important difference. In our work, the angle rate of near-Earth spacecraft is high, and an absolute measure of integrated electron content is possible over the roughly 50-second observation-time arc. The deep space angle rates are primarily Earth rotation ( $\sim 7 \times 10^{-3}$  rad/s), and integration over long periods of time (hours) are used to obtain changes in integrated electron content rather than absolute content.

The measurability of the electron content can be seen from the following relation:

$$I_v = \left( \frac{1}{80.6} \right) \left( \frac{f^2}{\dot{E}} \right) \left( \frac{\sin^2 E}{\cos E} \right) \left( \dot{r} - k_s - \frac{dR}{dt} \right) \quad (\text{electron/m}^2), \quad (3)$$

where

$I_v$ ,  $f$ , and  $E$  are as defined previously and

$\dot{r}$  = range-rate from tracking data (m/s),

$\frac{dR}{dt}$  = differentiated range from tracking data (m/s),

$k_s$  = spacecraft range-rate bias due to spacecraft spin\* (m/s),

$\dot{E}$  = rate of change of local elevation angle at ray intercept point at 300-km height (rad/s).

The angle rate  $\dot{E}$  is linked to the tracking station measurements of elevation  $E'$  and elevation rate  $E'$  by

$$\dot{E} = \left\{ \frac{\sin E'}{\left[ 1 - \left( \frac{a}{a+h} \right)^2 \cos^2 E' \right]^{1/2}} \right\} \left( \frac{a}{a+h} \right) \dot{E}' \quad (4)$$

\*If spin stabilized, see Marini, J. W., "The Effect of Satellite Spin on Two-Way Doppler Range Rate Measurements", Goddard Space Flight Center Document X-551-69-104, March 1969, Goddard Space Flight Center, Greenbelt, Maryland.

As seen in Figure 3, the results show excellent agreement between the vertical content extracted from Explorer 41 tracking data,  $I_v = (2.4 \pm 0.1) \times 10^{17}$  electron/m<sup>2</sup>, and that based on ESSA  $f_0F_2$  data,  $I_v = 2.45 \times 10^{17}$  electron/m<sup>2</sup>. This happened to be during a stable period (local night) with no solar disturbance. However, daytime estimates based on average monthly  $f_0F_2$  predictions are often in error by a factor of 2 to 4 throughout the month.

This particular scheme for extracting integrated electron content directly from tracking data is therefore shown to be both feasible and highly desirable for corrections to near-Earth as well as deep space tracking data. In some cases, simultaneous range and range-rate data may not be available or elevation angle rates may be too small for determining corrections in the desired observation time. In such cases, measurements involving synchronous spacecraft such as ATS 1 and ATS 3 can be used to update the presently used ionospheric profiles, which are based on monthly predictions that are available three months in advance.

#### REFERENCES

1. Schmid, P. E., Rangaswamy, S., and Murray, C. W., "Ionospheric Corrections Based on VHF Range and Range Rate Measurements", Proceedings of the GEOS-2 Program Review Meeting 22-24 June 1970, Vol. II, November 1970.
2. Mulhall, B. D. "Charged-Particle Calibration System Analysis", JPL Space Programs Summary 37-64, Vol. II, pp. 13-21, August 31, 1970, Jet Propulsion Laboratory, Pasadena, California.

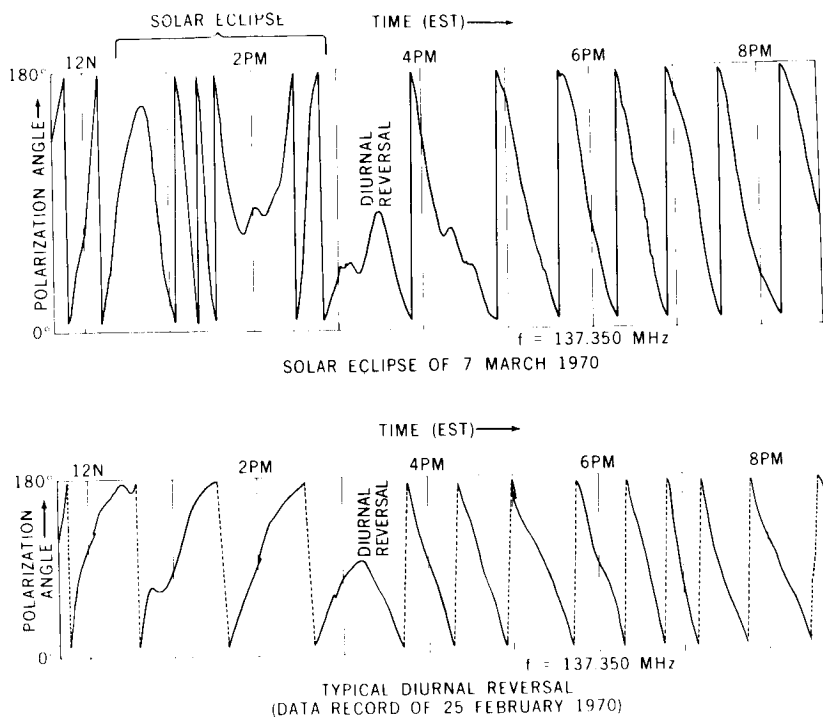


Figure 1—Faraday rotation data from ATS 3.

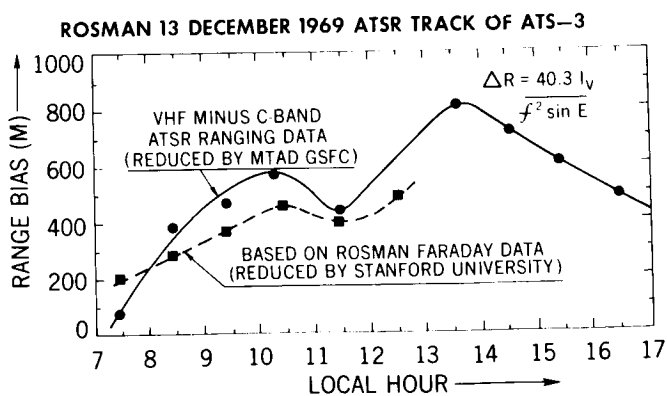


Figure 2—Zenith ionospheric range bias.

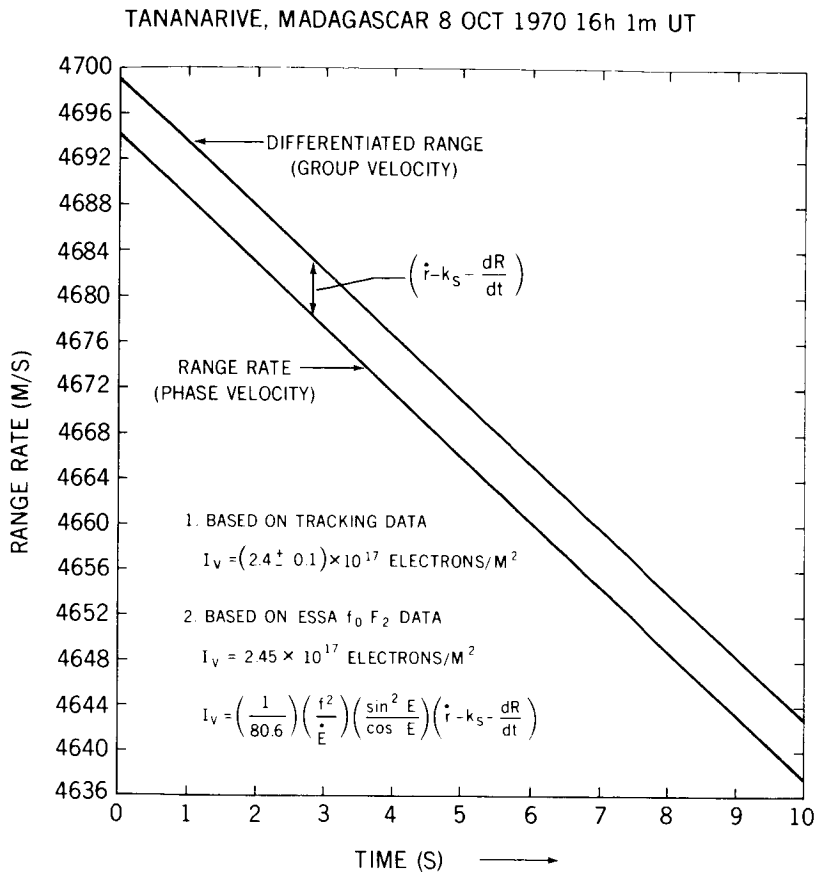


Figure 3—Explorer 41 track by VHF GSFC range and range-rate system.

## COMPARISON OF SATELLITE THEORIES

H. G. Hertz

Goddard Space Flight Center is engaged in computing orbits of artificial satellites on a routine basis. For that reason it is appropriate to examine the mathematical models used with respect to accuracy and efficiency. Here, results of an investigation concerning the accuracy only will be discussed.

To determine the motion of an artificial satellite mathematically, one must start out with a position-velocity vector at a specified time, called the epoch, or use six equivalent quantities and specify a force model. This model may have various degrees of complexity. In the simplest case, one may consider merely the attraction of a spherical Earth. More complex models would imply the attraction of an Earth with a potential due to zonal harmonics only or due to zonal and tesseral harmonics. The complexity would be increased by adding drag or solar radiation pressure or both.

Various mathematical methods used in determining the motion (using one of the possible force models) lead to various mathematical models. There are two types of such models: numerical integration theories and analytical theories.

In numerical integrations the solution is constructed stepwise, while analytical theories permit the solutions to be constructed for individual points. Numerical integrations therefore tend to be slow; furthermore, they offer no physical insight. Analytical theories allow quick determinations for the points required and also offer physical insight into the structure of the solution. On the other hand, it is fairly easy to add forces to the force model employed in the numerical integration. It is also easy to attain a specified accuracy in a numerical integration. The addition of additional forces and the attainment of a specified accuracy in case of analytical theories, on the contrary, may be a very involved process.

Since the accurate solution for the motion is not known, only indirect tests of the accuracy are possible. The solution for one particular model

may be used as a standard, and solutions based on other models may be compared with the standard solution. If the force model is restricted to the forces due to a potential consisting of zonal harmonics only, two integrals exist. One implies that the total energy is constant, and the other that the z-component of the angular momentum is constant. Because of numerical inaccuracies, strict constancy cannot be achieved. The amounts of spread in the values of the total energy and the z-component of the angular momentum for a set of times may be considered as measures of the accuracy of the mathematical models with which these values are computed.

Five mathematical models have been constructed using a position-velocity vector which is associated with a nominal orbit for the Vanguard 2 satellite. In all models the same force model was used, namely the one which corresponds to a potential with the zonal harmonics to order four. Models 1 and 2 are numerical integrations with step sizes of 1 min and 0.5 min, respectively. The integrations are based on programs created by Juergensmeyer.\* Models 3, 4, and 5 are analytical theories. Model 3 corresponds to the Brouwer theory as originally published (Reference 1) and is a first-order theory. A modification of this theory, which is still of the first-order, is used in routine GSFC operations. Model 4 incorporates a modification introduced by the author (Reference 2) to the original Brouwer theory. Model 5 is the second-order theory by Aksnes (Reference 3).

The orbit based on model 1 (i.e., the 1-min numerical integration) was taken as a standard orbit.\*\* The rectangular coordinates in the orbits based on models 2 through 5 were compared with the standard orbit every 40 min in the case of model 2 and every 4 hr for models 3 through 5 for an arc of 60 days. The largest maximum absolute values of the corresponding differences are shown in Table 1. The two integrations differ thus only by a few meters. The original Brouwer differs from the 1-min integration by as much as nearly 27 km. The modification inherent in model 4 reduces the maximum difference to less than 200 m. The maximum differences between Aksnes and the 1-min numerical integration are even smaller.

---

\*Juergensmeyer, C. H., "A Double Precision Cowell Integration Program", Goddard Space Flight Center Document X-542-63-139, July 1962, Goddard Space Flight Center, Greenbelt, Maryland.

\*\*This is reasonable, since numerical integrations tend to be more accurate.

Table 2 shows that the spreads in the values of the total energy and the z-component of the angular momentum are much less for model 2 than for model 1. This suggests that it might have been better to have taken the 0.5-min numerical integration as the standard orbit.

The modification introduced in model 4 reduced the spread in the values of the energy but increased the spread in the values of the z-component of the angular momentum. The spread of the corresponding values for the Aksnes theory is less than that for the Brouwer theory. It is remarkable that the spread in the values of the z-component of the angular momentum is even less than it is in the case of the numerical integrations. Part of the results presented here were published previously (Reference 4).

This investigation shows that a considerable increase in the accuracy for the Vanguard 2 orbit may be obtained by the use of models different from the ones used in the Goddard Space Flight Center routine operations. It is planned to continue these investigations with other orbits and other theories.

#### REFERENCES

1. Brouwer, Dirk, "Solution of the Problem of Artificial Satellite Theory without Drag", *Astronomical Journal*, 64: 378, 1959.
2. Hertz, Hans G., "A Computer Program Version of the Brouwer Orbital Theory with Optional Modifications", NASA Technical Memorandum X-63749, August 1969.
3. Aksnes, Kaare, "A Second Order Artificial Satellite Theory Based on An Intermediate Orbit", *Astronomical Journal*, 75: 1066, 1970.
4. Hertz, Hans G., "Numerical Integration Orbits and Brouwer and Modified Brouwer Orbits", NASA Technical Memorandum X-63809, August 1969.

Table 1—Comparison of mathematical models with Cowell 1-min integration  
(60-day arc)  
(nominal Vanguard 2 orbit).

POINTS	0.5 MINUTE INTEGRATION 40 MIN (m)	ORIGINAL BROUWER 4 HR (m)	MODIFIED BROUWER 4 HR (m)	AKSNES 4 HR (m)
$\Delta X$	3	26840	121	94
$\Delta Y$	2	23378	76	82
$\Delta Z$	1	13870	161	48

Table 2—Maximum relative changes in the constancy of integrals.

	INTEGRATION		BROUWER		AKSNES
	1-MIN	0.5-MIN	ORIGINAL	MODIFIED	
ENERGY	$8 \times 10^{-9}$	$8 \times 10^{-12}$	$5 \times 10^{-6}$	$1 \times 10^{-8}$	$1 \times 10^{-8}$
Z-COMP.	$3 \times 10^{-9}$	$3 \times 10^{-12}$	$9 \times 10^{-7}$	$2 \times 10^{-6}$	$< 1 \times 10^{-12}$
ANG. MOM.					

## **AN ANALYSIS OF THE EXPECTED ECCENTRICITY PERTURBATIONS FOR THE SECOND RADIO ASTRONOMY EXPLORER (RAE B)**

**James P. Murphy**

The second spacecraft in the Radio Astronomy Explorer series, RAE B, is to be placed in a nearly circular lunar orbit. The orbit is to remain circular, with an eccentricity constraint of less than 0.005 for a period of a year or more, if possible. This constraint is made because of factors concerning the dynamical stability of this gravity gradient spacecraft and the economical reduction of the experimental data. Other constraints upon the orbit are the result of sunlight conditions and the precession of the orbital plane. Thus, original plans called for a circular orbit about 1100 m above the lunar surface with a selenographic inclination between 120 and 130 deg and an initial longitude for the ascending node of 282 deg. The initial values of the argument of perilune and the eccentricity were arbitrary so long as the latter was less than 0.005.

Past experience with the Lunar Orbiter and Apollo missions has shown that eccentricity perturbations have been quite severe. The Apollo orbits were close, circular, and nearly equatorial; the Lunar Orbiter spacecraft flew more distant elliptical orbits with either low or nearly polar inclinations. The RAE B orbit is to be circular, as in the Apollo missions, but more distant, as in the Lunar Orbiter missions, and with a moderate inclination unlike either of these two previous missions. Nevertheless, eccentricity histories for these missions can be useful in planning for RAE B. One such history is presented in Figure 1. The dots in this figure are the actual elements determined from the tracking data. The solid line represents a numerical integration that used the current operational Apollo field, the L1 model. Two points can be made: First, the eccentricity perturbations are large relative to the RAE B eccentricity constraint, and second, the L1 model predicts this eccentricity variation quite well. It should be mentioned at this point that the results presented in this study were obtained by the use of eight different lunar gravity models developed at the Jet Propulsion Laboratory, the Langley Research Center, and GSFC. The main results of this study are essentially independent of the gravity field chosen. All the

results are documented in a GSFC report, but because of time limitations we will concentrate on the results obtained from the L1 model.

Eccentricity perturbations for RAE B are of two types: The first type has a monthly period, while the second type has a period of the order of many years and hence appears to be linear during the course of a year. An analytical development of these perturbations follows.

The monthly eccentricity variation is

$$\delta e = -\frac{3}{16} \frac{n}{n} \left(\frac{b}{a}\right)^3 C_{3,1} \left\{ \left[ 5 \sin^2 i (1 + 3 \cos i) - 4(1 + \cos i) \right] \cos(\omega + \Omega) \right. \\ \left. - \left[ 5 \sin^2 i (1 - 3 \cos i) - 4(1 - \cos i) \right] \cos(\omega - \Omega) \right\}$$

It can be seen that the amplitude is a function only of the semimajor axis and inclination of the orbit and of certain physical parameters such as the rotation rate, mean radius, and gravity coefficients of the Moon. If one evaluates this amplitude for various orbits within the RAE B nominal range and for various lunar models, it will be observed that this amplitude hardly changes. For instance, if  $a = 2838$  km, and  $i \approx 120$  deg then from the L1 model,

$$\delta e = .00185 \cos \omega \cos \Omega \approx .00185 \cos \Omega.$$

It should be noted that this would result in a peak-to-trough variation of 0.0037. In other words, 74 percent of the eccentricity constraint would be reached in a month or less. Therefore, any appreciable long term perturbation would be most unwelcome. Unfortunately, for any value of the inclination in the originally proposed range and for any of eight lunar gravity models tested, the envelope of the eccentricity variation had a very substantial positive slope. After tabulating the results of some parametric inclinations studies and after performing an analysis of the perturbation equations in analytical form, we discovered that the positive slope would vanish for an inclination of 116.565 deg, just a few degrees under the nominal inclination range. This value is that of the so-called retrograde "critical inclination", which was given much attention in the literature during the early stages of the development of artificial satellite theories. As an approximation, one may write for the long-term perturbations:

$$\dot{e} = -A \cos \omega$$

$$\dot{\omega} = (A/e) \sin \omega,$$

where

$$A = \frac{3}{8} \left( \frac{b}{a} \right)^3 n C_{3,0} \sin i (1 - 5 \cos^2 i).$$

When these equations are solved, the results are

$$e \sin \omega = e_0 \sin \omega_0$$

$$e \cos \omega = e_0 \cos \omega_0 - A t.$$

It can be deduced from these equations that, regardless of the sign of  $C_{3,0}$ , the eccentricity will grow linearly in time so long as  $A$  is nonzero. However,  $A$  vanishes at the recommended inclination of 116.565 deg. The results of this analytical treatment were confirmed by numerical integration of an RAE B orbit. One set of integrations is shown in Figure 2. After considering all the results of a lowering of the value of the nominal inclination, the RAE project accepted the recommendation for a new nominal inclination.

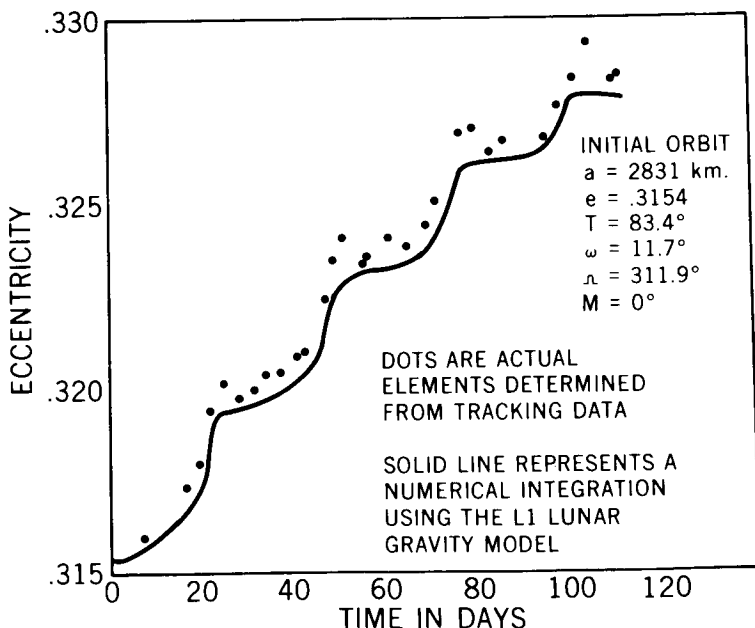


Figure 1--Eccentricity versus time for Lunar Orbiter 5 (arc 4).

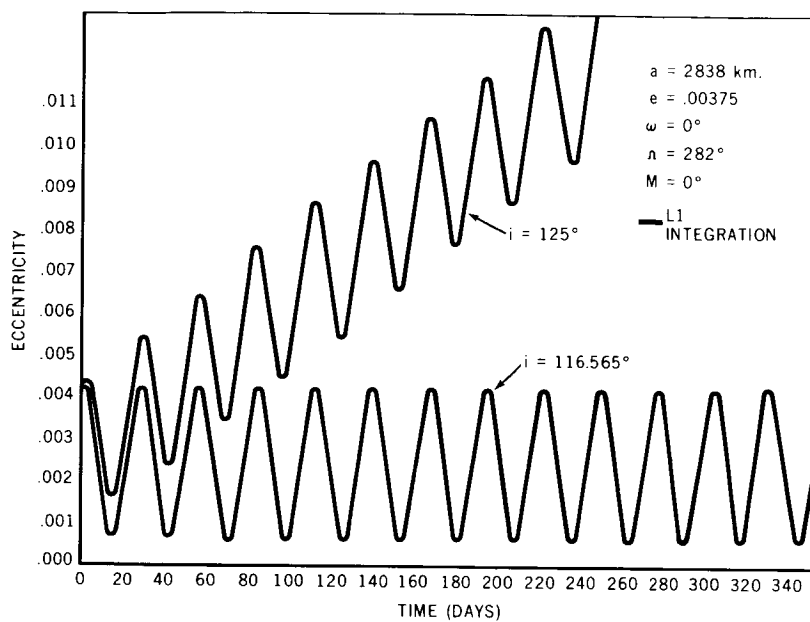


Figure 2—Eccentricity versus time for RAE B.

## **DYNAMICAL IN-ORBIT BEHAVIOR OF THE RADIO ASTRONOMY EXPLORER SATELLITE**

**Harvey Walden**

The Radio Astronomy Explorer satellite, or the RAE 1 as it is commonly known, was launched 2½ years ago and is presently in a near-circular Earth orbit at an altitude of almost 6000 m. Aside from its impressive achievements in the field of radio astronomy, the RAE satellite is of interest because it is the first system to deploy successfully a directive antenna array. Another distinctive feature which enhances the interest in its actual in-orbit dynamical behavior is the length of its primary antenna booms, which measure almost 0.5 m tip to tip. These booms are far longer than the appendages of any other spacecraft orbited to date, and for this reason, the RAE satellite is the largest array yet placed in space, in terms of longitudinal dimensions.

From a dynamical point of view, the objective of the RAE mission is the attainment of a stable orbital capture by gravity-gradient forces. This is a method of completely passive three-axis attitude stabilization. The purpose of this stable capture is twofold: to permit modest pointing accuracies by the directive antennas and to achieve small antenna deformations. Such deformations create antenna pattern distortions in the measurement of long-wavelength radio emissions from extraterrestrial sources, and it is for this reason that the antenna boom flexural motions must be minimized. Because of their extreme length, 460 m tip to tip, the RAE booms are, in effect, much more flexible than those of other satellites. The natural bending frequencies of the booms are very low, and the amplitudes of the bending motions have the potential of becoming very large. This introduces problems of stability and dynamics not encountered previously in other satellite missions. Static bending of the booms due to gravity-gradient and inertial forces and boom vibration due to time-varying thermal, solar, and dynamic effects can have a significant influence on RAE spacecraft stabilization. Hence, the success of the radio astronomy experiments depends, in large part, on the dynamical in-orbit behavior of the satellite.

The main sensing apparatus of the RAE spacecraft consists of four flexible antenna booms extending outward from a rigid central hub in a double "Vee" configuration. The spacecraft is stabilized in a nonspin mode about the local vertical. In this way, one "Vee" antenna is continuously directed toward the Earth, while the other antenna scans the celestial sphere. The four main sensing antenna booms each extend 230 m from hub center to tip when fully deployed. A damper mechanism, consisting of a torsion wire suspension with magnetic hysteresis damping and two additional booms, is also included on the spacecraft. The damper attenuates rotational oscillations of the spacecraft hub and the resulting indirect vibration of the primary antennas.

Knowledge of the spacecraft dynamical in-orbit behavior is obtained from several on-board sensors and the associated ground-based processing systems. An on-board attitude determination system, consisting of a solar aspect sensor and a triaxial magnetometer, measures the orientation of the central hub. Four television camera systems enable the lateral displacements of the tips of the main booms from their straight-line locations to be computed. In practice, only one of the four vidicons has provided useful boom tip information in this regard.

The passive attitude control system of the RAE satellite has maintained a well stabilized attitude condition during the more than 2 years that the main antenna booms have been at full lengths. Figure 1 shows typical central hub attitude motions, in this case on a date about 3 months after the final boom deployments and during an extended interval of full sunlight conditions. None that the pitch and roll angles of the central hub usually remain within  $\pm 2$  deg of the ideal zero-degree equilibrium condition. Deviations as large as  $\pm 4$  deg occur comparatively rarely. Central hub motions in yaw only occasionally exceed  $\pm 4$  deg about an equilibrium value of about  $-13$  deg. The nonzero equilibrium value for yaw is due to the fact that the two damper booms are skewed from the plane of the primary double "Vee" antenna. This so-called yaw bias value was anticipated in prelaunch mathematical simulations. The motions of all three attitude angles are well bounded but quite erratic, although a definite correlation in the motions of all three angles exists. (The break in the otherwise continuous curves is caused by operational difficulties in receiving observational data.) Almost all three-axis attitude motions observed since the first few weeks after the final deployments has been similar to that shown in

Figure 1, i.e., small and erratic. It is virtually impossible to distinguish between actual central hub rotations and sensor system noise and inaccuracies.

Figure 2 displays the measured boom tip displacements (from straight-line positions) of the one observable boom on the day after the final deployments. In this figure, "in-plane" refers to tip displacements in the direction parallel to the ideal plane formed by the four main booms when they are straight; "out-of-plane" indicates deflections perpendicular to this plane. The in-plane deflection is much larger because by far the larger component of the gravity-gradient force occurs in this direction. The out-of-plane deflections are further minimized by very low boom cross-section temperature gradients. The oscillatory short-period motions shown in Figure 2 probably are due in large part to the boom deployment operations on the preceding day. Prelaunch computer simulation studies had predicted average static in-plane tip deflections of about 40 m. This value is only slightly greater than the average value displayed by the data in Figure 2, which includes only a fractional portion of a long-period boom motion.

Most boom tip pictures have been taken only over time durations which are too short to permit much useful analysis. The basic purpose in taking these pictures has been to monitor the satellite rather than to obtain data for dynamics investigations. Table 1 summarizes the results of a large number of boom tip pictures taken between January and October of 1969. Three convenient data blocks, labeled "A", "B", and "C", were formed with varying numbers of picture sets in each block, as shown. The mean values in this table should be approximately the average value of the boom tip deflection during each respective time interval shown. The three in-plane mean values are all in reasonably close agreement with the predicted average value of 40 m. During the time interval covered by data block A, the satellite was being eclipsed from the sun for a portion of each orbit. Blocks B and C, however, were taken during full sunlight conditions. The standard deviations include both actual boom tip motion relative to the average displacement and also any time-varying inaccuracies that may be present in the measurements. The resolution of each tip deflection measurement is about 1 m in both the in-plane and the out-of-plane directions. The average out-of-plane tip deflection is difficult to predict from mathematical models since it is very sensitive to central hub yaw angle, boom warpage, boom temperature gradients, and solar pressure. The variation in the orbit-sunline

geometry during the later intervals may have produced solar pressure effects responsible for the indicated decrease in the average out-of-plane tip deflection.

In conclusion, the dynamical in-orbit behavior of the RAE satellite demonstrates that the large boom vibrations and major attitude stability problems anticipated prior to launch have not materialized. In the more than 2 years since full deployment of the antenna booms in October 1968, the RAE spacecraft has remained well stabilized in local orientation and has continued to transmit valuable radio astronomy data.

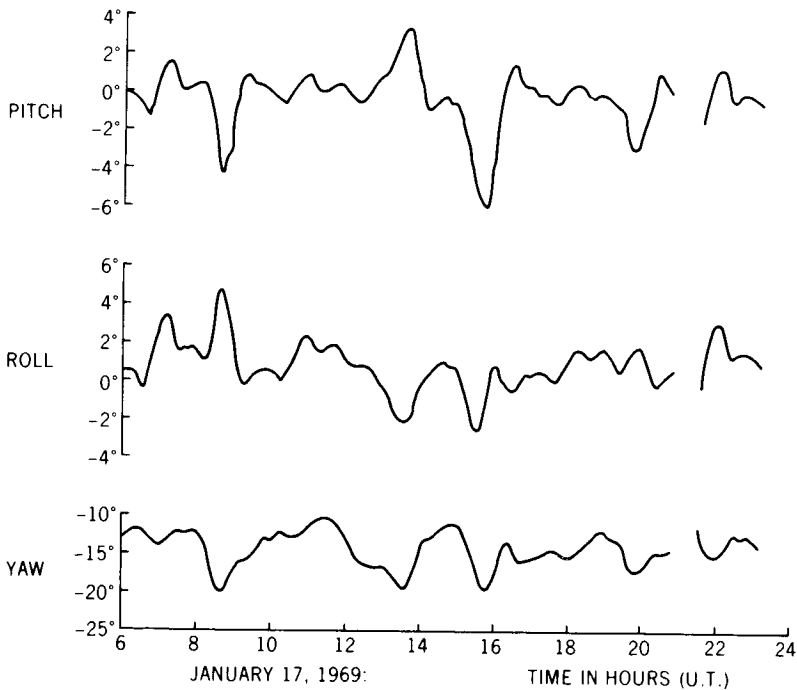


Figure 1—Central hub attitude motions on January 17, 1969.

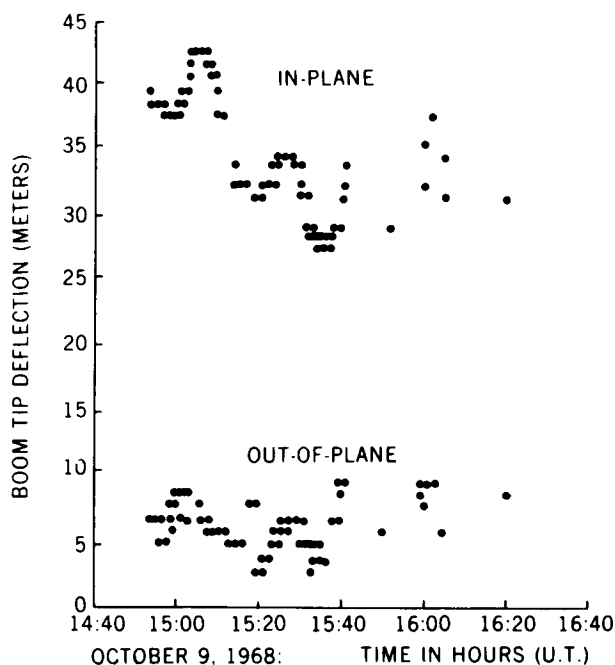


Figure 2—Main boom tip deflections on October 9, 1968.

Table 1—In-orbit tip deflections of upper trailing main boom.

DATA BLOCK	TIME PERIOD COVERED IN DATA BLOCK (1969)	NO. OF PICTURE SETS IN DATA BLOCK	TIP DEFLECTIONS (METERS)			
			IN-PLANE		OUT-OF-PLANE	
			MEAN VALUE	STANDARD DEVIATION $\sigma_i$	MEAN VALUE	STANDARD DEVIATION $\sigma_o$
A	JAN. 29 TO MARCH 24	15	42	11	4.3	2.2
B	JULY 9 TO SEPT. 6	14	36	7	-0.1	0.7
C	SEPT. 7 TO OCT. 7	27	40	1	-0.2	0.7

## FUTURE TECHNIQUES FOR TRACKING OF SYNCHRONOUS SATELLITES

James L. Cooley

The study of the Tracking and Data Relay Satellite System, in which synchronous satellites would be used for tracking and data relay purposes, provides an opportunity to consider future techniques for tracking of synchronous satellites. The desire to minimize the number of ground stations used and to utilize the tracking and data relay measurement system itself, leads to the consideration of new techniques, other than the conventional ground to synchronous satellite tracking, for determining and refining the orbits of synchronous satellites. Two measurements will be considered here:

- (1) Range sum and range-rate sum measurements through a synchronous satellite to a user satellite.
- (2) Range sum and range-rate sum measurements through a synchronous satellite to a ground-based transponder.

The tracking link (see Figure 1) originates at a main ground station, is relayed through the synchronous satellite to a user satellite, and is returned to the main ground station via the same link, thus providing range sum measurements ( $r_1 + r_2$ ) and range-rate sum measurements ( $\dot{r}_1 + \dot{r}_2$ ) to a user satellite. Similarly, the transponder measurement link originates at the main ground station, is relayed through the synchronous satellite to a ground-based transponder, and is returned via the same link to the main ground station, thus providing range sum and range-rate sum measurements to a ground-based transponder.

A tracking system error analysis computer program is used to study the feasibility of these measurements. Error analysis transforms expected uncertainties in the measurement system itself, namely the measurement noise and bias, and uncertainties in the locations, namely ground station location uncertainty and *a-priori* uncertainties in the orbits of the

synchronous satellite and user satellite, into expected uncertainties in each of the orbits after tracking. The orbit determination technique employed will be to simultaneously update the orbits of both the user satellite, taken here to be in a Nimbus orbit, and the synchronous satellite, taken to be in an ATS orbit. It is the orbit determination for the synchronous satellite that is of concern here. The measurements are simulated at the rate of one per 10 s for 1, 2, and 3 Nimbus passes. Resulting uncertainties expected for the ATS orbit, when the range sum and range-rate sum measurements to the Nimbus satellite are processed, are given in Table 1.

The results show that the 500-m ATS *a priori* position uncertainty can be reduced to 150 m after 3 Nimbus passes. One reason for this reduction is the dynamic nature of this tracking situation, where the range sum and range-rate sum measurements vary due to the Nimbus motion. This is in contrast to the nearly static situation with conventional ground to synchronous satellite tracking where the range and range-rate measurements are nearly constant.

The next case adds the ground-based transponder range sum and range-rate sum measurements. These measurements have an effect after 3 passes and further reduce the ATS position uncertainty to 100 m.

In conclusion, both of the measurement types considered here, the range sum and range-rate sum measurements through a synchronous satellite to a user satellite, and the range sum and range-rate sum measurements through a synchronous satellite to a ground-based transponder, would prove useful in the future for determining and refining the orbits of synchronous satellites.

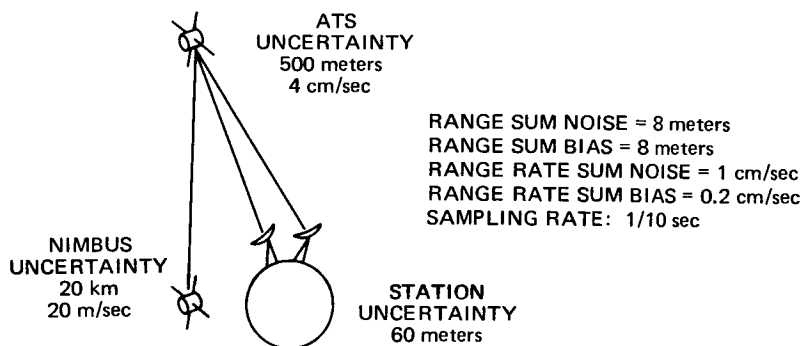


Figure 1—ATS/Nimbus error analysis modeling.

Table 1—Solving for ATS and Nimbus orbits.

NIMBUS PASSES	ATS POSITION UNCERTAINTY ( $1\sigma$ ) USING RANGE SUM & RANGE RATE SUMS
1	350 meters
2	200 meters
3	150 meters
NIMBUS PASSES	ATS POSITION UNCERTAINTY ( $1\sigma$ ) USING RANGE SUM & RANGE RATE SUM + TRANSPONDER MEASUREMENTS
1	350 meters
2	170 meters
3	100 meters

## THE GEOPOTENTIAL AT SYNCHRONOUS-ORBIT ALTITUDES

C. A. Wagner

I would like to discuss briefly the latest solution I have obtained for the Earth's gravity potential at synchronous-orbit altitudes.

As you may know, a distant satellite in a synchronous orbit is affected significantly by only a few low degree terms in the conventional spherical harmonic representation of the field. These terms include the oblateness of the Earth and, because of the commensurability of the synchronous orbit, all the longitude-dependent terms as well.

It has been 7 years since the first such satellite was put into orbit. Since that time, about 50 others have followed, making synchronous orbits probably the most popular variety of orbit. However, only about 15 of these objects are close enough to exact commensurability to be really useful in studies of the small but persistent effects of the so-called resonant harmonics of gravity.

I have obtained the present solution for these harmonics from the most representative sample of tracking data from eight of these satellites in 21 distinct free-drift arcs. The length of time for these arcs ranges from 6 weeks to 3½ years (Table 1).

The observations I use in my solution are the mean Kepler elements for the satellites reported by the various responsible tracking agencies, including GSFC. The element most sensitive to the resonant effect is the mean geographic longitude or equator crossing of the satellite. This is a simple combination of the Kepler orbit arguments and the position of the Earth and is the principal observable recovered in the solutions. The quality of this observable varies from arc to arc, but in no case does it approach the fine precision of the tracking required for geodetic recovery from nonresonant satellites. The geodetic solutions with these data demonstrate conclusively that we are at last getting absolute determinations of the low-degree field.

This can be seen from the answers to three questions concerning these sensitive resonant data. First, if there were no resonant gravity harmonics, what kind of recovery of these data would we get? Figure 1 shows the evolution of the longitude of Syncom 2 between 1965 and 1969. Without resonant harmonics, this evolution would be almost linear, and, since the data in this arc have an accuracy of about 0.05 deg, the mean weighted residual in a best-fit trajectory would be over 100. Second, how well can the data be recovered with the use of recent gravity models that include resonant harmonics but not the data itself? Table 2 gives results of orbits for these satellites calculated with recent fields through fourth degree. The first two rows show the overall recovery with two recent Smithsonian geopotentials. From about 100 without low degree coefficients, the mean weighted residual (rms) comes down to below 3 with the latest SAO field, which includes ground gravity information. An improvement in the fit to less than 2 is found with a 1969 all-satellite SAO field, very little different in these critical harmonics from the 1970 field.

Third, what field adjustment is necessary for complete recovery of the data? This question is answered in the last two rows of Table 2. In the unconstrained solution, the dominant harmonics of second and third degree were freely derived along with the orbits. The residuals were lowest, but the (3,1) harmonic was not realistic and many correlation coefficients were large. The last row shows the most satisfactory solution obtained from the 24-hour data. Here, all five significant harmonics were derived with reasonable *a priori* constraints from the SAO COSPAR coefficients. This constrained field shows adequate data recovery with realistic coefficients that are only moderately correlated.

There should be little doubt that we can now predict the long term drift of these satellites to considerable accuracy even over periods of many months. In fact, a dramatic test of this proposition came in September 1970 when Syncom 3 was reacquired by GSFC within 0.4 deg of its predicted position after being silent for almost 2 years. This prediction was made with the constrained field.

The economics of computing these fields from mean element data is also interesting. Only 279 observations were used, compared with over 50,000 for the SAO solutions. The solutions themselves involved about five differential corrections to both orbits and field parameters or a total of 60

orbit years of calculation, and took less than 4 min of computing time on an IBM 360/95 machine.

The overall results of this study of the geopotential for synchronous satellites are as follows:

1. Absolute accuracy of second-degree coefficients has been established to better than 3 percent. Coefficients through fourth degree have been established to better than 15 percent.
2. The positions of equilibrium points for geostationary satellites have been established to better than  $\frac{1}{2}$  deg.
3. Accuracy in prediction of orbits for 24-hour satellites has been established to better than 1 deg for periods greater than 2 years.

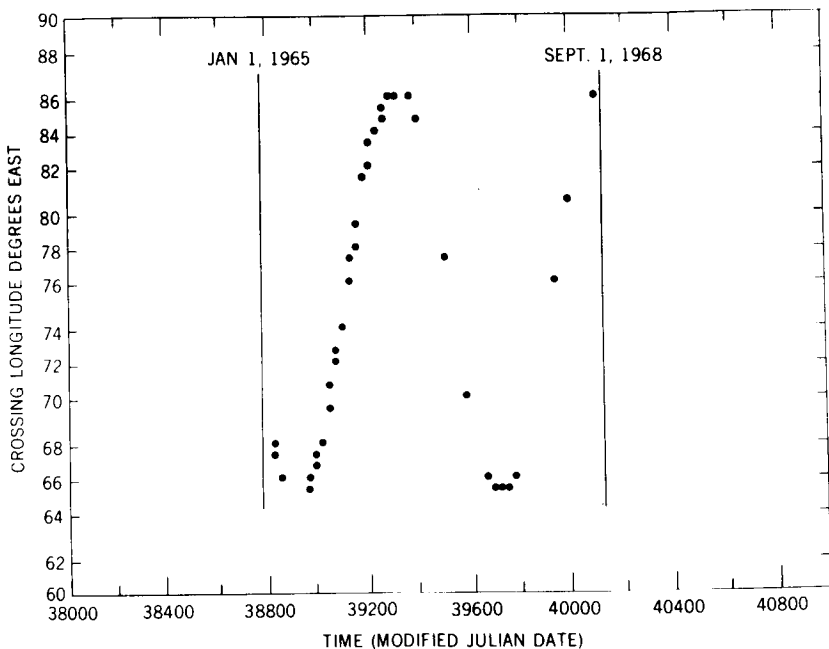


Figure 1—Equator crossings for SYNCOM 2, 1965-1968.

Table 1—Twenty-four hour satellite arcs in 1970 resonant geopotential solutions.

SATELLITE	ARC	NUMBER OF KEPLER ELEMENT SETS USED	SPAN OF DATA (modified Julian Days)	GEOGRAPHIC LONGITUDE SPAN IN ARC (degrees)	ORBIT INCLINATION (degrees)	ESTIMATE OF QUALITY OF DETERMINATION OF THE GEOGRAPHIC LONGITUDE, $\sigma$ , (s), IN ARC FROM INDIVIDUAL ARC ANALYSES (degrees)	RMS RESIDUALS IN LONGITUDE FROM COMBINED ARC SOLUTIONS (degrees)		
							WITH 24 HOUR SATELLITES ALONE, SOLVING FREELY FOR 6 RESONANT COEFFICIENTS	WITH 24 HOUR SATELLITES COMBINED WITH SAO 1969 COSPAR DATA, IN CONSTRAINED SOLUTION FOR 10 RESONANT COEFFICIENTS	WITH SAO 1969 COSPAR FIELD ALONE
SYNCOM 2	1	16	38263-38351	302-305	33.0	0.025	0.013	0.013	0.013
SYNCOM 2	2	11	38361-38443	296-301	32.8	0.025	0.034	0.034	0.035
SYNCOM 2	4	9	38510-38570	196-243	32.5	0.020	0.015	0.014	0.014
SYNCOM 2	5	24	38596-38697	72-189	32.3	0.036	0.039	0.038	0.035
SYNCOM 2	8	15	38816-38918	65-68	31.8	0.020	0.018	0.018	0.018
SYNCOM 2	D=0	42	38816-40104	65-65	29-32.0	0.040	0.037	0.038	0.103
SYNCOM 3	6	9	38699-38750	178-180	0.0	0.015	0.014	0.015	0.013
SYNCOM 3	7	10	38775-38835	174-181	0.0	0.055	0.054	0.055	0.052
SYNCOM 3	11	16	39075-39262	165-172	0.5	0.020	0.012	0.014	0.013
SYNCOM 3	13	4	39385-39491	160-161	1.3	0.015	0.005	0.006	0.010
SYNCOM 3	14	15	39663-40175	146-160	2.3.0	0.045	0.061	0.061	0.110
ATS 1	1	12	40204-40248	210-211	1.2	0.005	0.001	0.001	0.001
ATS 3	1	12	40197-40241	288-312	0.8	0.005	0.002	0.003	0.003
ATS 3	2	13	40267-40337	283-288	0.3	0.005	0.004	0.003	0.002
ATS 3	3	10	40524-40577	313-315	0.3	0.005	0.002	0.003	0.003
INTELSAT 2-F3	1	12	39607-39605	349-352	1.0	0.025	0.028	0.028	0.030
INTELSAT 2-F3	2	10	40406-40642	346-348	1.0	0.020	0.011	0.012	0.015
INTELSAT 2-F4	1	8	40323-40608	179-194	1.0	0.040	0.043	0.046	0.062
EARLY BIRD	1	11	38897-39080	324-332	0.5	0.025	0.025	0.028	0.028
EARLY BIRD	2	6	39096-39218	321-331	0.8	0.010	0.007	0.009	0.009
ATS 5	1	14	40476-40558	253-256	2.6	0.005	0.004	0.006	0.006

Table 2—Resonant geopotential coefficients for 24 hour satellites and rms fits to 21 arcs.

FIELD	OVERALL WEIGHTED RMS IN 21 ARC SOLUTION	2,2		3,1		3,3		4,2		4,4	
		C	S	C	S	C	S	C	S	C	S
STANDARD SAO EARTH II (1970)	2.46	1.558	-0.881	2.128	0.281	0.096	0.199	0.074	0.158	-0.0017	0.0072
SAO COSPAR (1969)	1.38	1.566	-0.896	2.040	0.262	0.096	0.198	0.073	0.148	-0.0028	0.0078
WAGNER (UNCONSTRAINED) 2,2-3,1-3,3 (1970)	0.849	1.568	-0.907	1.687	0.483	0.103	0.204	0.074	0.158	-0.0017	0.0072
WAGNER SAO COSPAR (CONSTRAINED) (1970)	0.896	1.570	-0.908	2.029	0.289	0.098	0.205	0.075	0.150	-0.0028	0.0078

UNNORMALIZED COEFFICIENTS IN UNITS OF  $10^{-6}$

## **IN-ORBIT FLEXIBLE SPACECRAFT DYNAMICS PROGRAM**

**Joseph V. Fedor**

A continuous flexible body nonlinear dynamics computer program has been developed in support of flight programs such as IMP I, IMP H, and IMP J and RAE 1 and RAE B. A version of this program successfully predicted the performance of the RAE 1 spacecraft, the world's largest satellite in orbit, in every major respect. The most recent version (for IMP I) can simulate up to ten arbitrarily oriented flexible antennas attached to a spinning or nonspinning satellite (gravity gradient or three-axis control) and compute the spacecraft and antenna motion as a function of time for predeployment, deployment, and in the orbital environment. This computer program promises long-term utility in the analysis of flexible spacecraft dynamics and attitude control.

Prior to the RAE flight program, satellites were considered essentially rigid in the analysis of satellite attitude dynamics. However, the RAE spacecraft (Figure 1 shows an artist's conception of it in orbit), with its 0.05-mm thick, 1.27-cm diameter, 225-m-long antennas, making it 450 m from tip to tip, no longer satisfies the rigid body assumption. Forces previously ignored in regard to the distorting of spacecraft, such as gravity gradient forces, orbit centrifugal force, thermal bending, and solar pressure, had a profound effect on the shape and stability of the satellite. As is known, the RAE spacecraft was a rousing scientific and technological success. Further, the computer program developed specifically for the RAE spacecraft predicted its performance in every major respect.

Recently, the IMP I, IMP H, and IMP J program emerged, and GSFC was confronted with the analysis of another type of flexible spacecraft. This time, the spacecraft was a spinning one with the added complexity of applied control torques. Figure 2 shows the IMP I spacecraft. It has six orthogonal booms for the electric field measurement experiment: two booms along the spin axis and four radial booms. The radial booms are 60 m long and 120 m from tip to tip; the spin axis booms are each 6 m long. From the experience of the RAE program development, a concept for a

second-generation generalized flexible body dynamics program evolved. The intention was to come up with a program that could handle not only spinning flexible spacecraft but also gravity gradient and three-axis control. The computer program was developed by a contractor and has been operational here at GSFC for the past year in the support of in-house flight programs.

The computer simulation of the spinning mode should be capable of handling the following aspects of the problem:

Effects of deployment of up to 10 antennas in any arbitrary direction,

Behavior of flexible antennas (open and closed cross section),

Nonlinear motion of spacecraft in all three dimensions,

Structural damping,

Thermal bending,

Solar pressure,

Magnetic torques,

Gravity gradient torques,

Aerodynamic forces,

Attitude control torques,

Viscous nutation damper,

Four-body calculated orbit or simple Keplerian orbit,

Precession of orbit,

Occultation by earth,

Convenient input-output routines (for parameter study).

A few key terms should be noted here. They are *continuous flexible body* and *practical computer running time*. The computer program takes into account the continuous flexible nature of the antennas or booms by representing deflections in terms of shape functions. By integration of the spatial dependence in the formulation of the equations of motion, a large amount of algebraic simplification is obtained. This results in a significant reduction in computer running time when compared to the time required for the segmented approach to flexible body analysis. Further, boom deployment presents no problem in the continuous simulation, while it does present a problem in the segmented approach.

Figure 3 shows a comparison of RAE flight data of roll, pitch, and yaw with the predictions of the computer program in the gravity gradient mode. The time span of the data is 12 hr, which corresponds to approximately three orbits; the solid curve represents the flight data, and the dashed curve represents computer predictions. It will be observed that there is fair to good agreement in roll and pitch and excellent agreement in the yaw angle.

The computer program is currently being used in the IMPI flight program, the Lunar RAE program, the IMP J program, and several GSFC in-house studies.

In conclusion, it is of value to point out that, based on current usage and adaptability, the computer program promises long-term utility in the analysis of flexible spacecraft dynamics and attitude control.



Figure 1—Artist's conception of the RAE spacecraft.

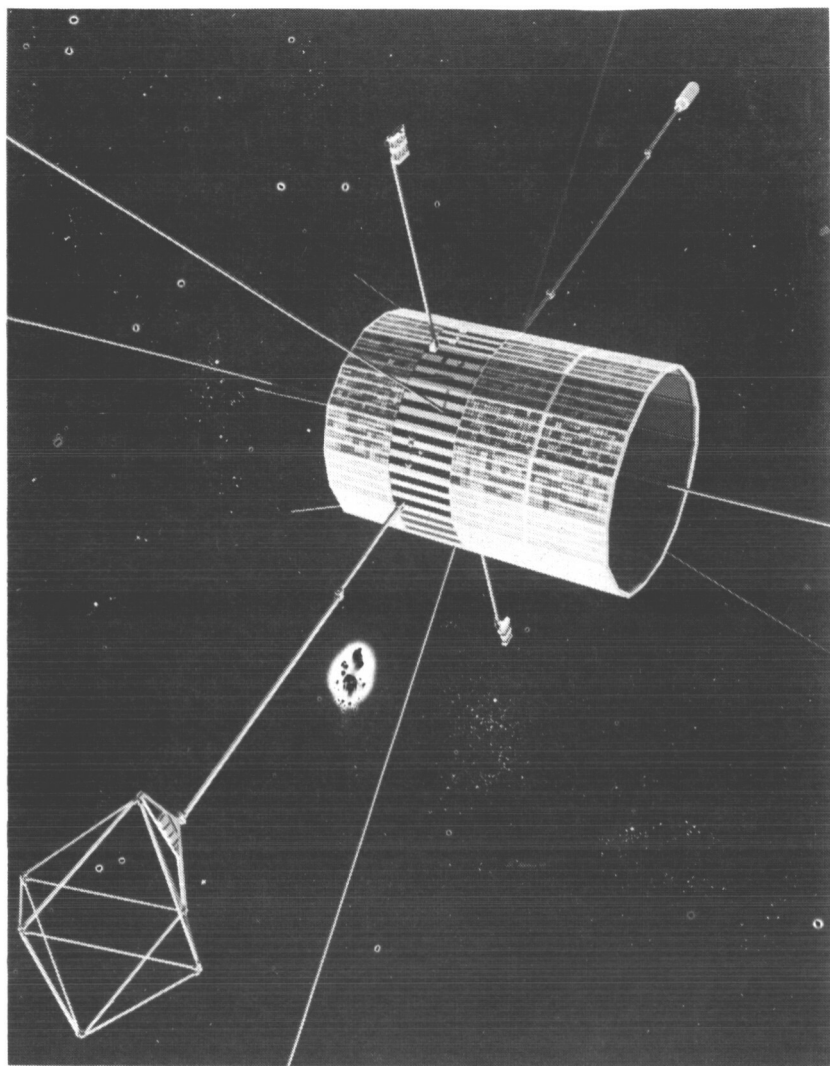


Figure 2—The IMP spacecraft.

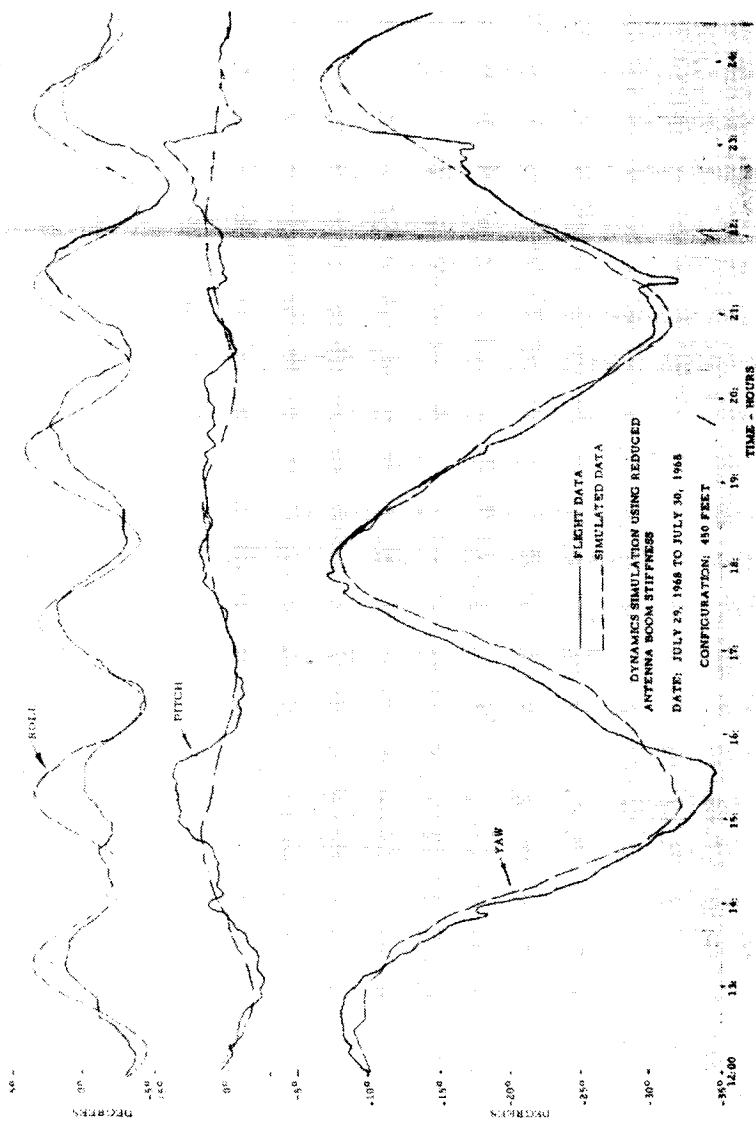


Figure 3—Comparison of RAE flight data with computer-predicted data.

## **STRUCTURAL-THERMAL-OPTICAL PROGRAM (STOP)**

**H. P. Lee**

The Structural-Thermal-Optical Program (STOP) is intended to coordinate technical disciplines and develop methods which exist in various areas and in their interfaces, as shown in Figure 1. This program primarily concerns the optical performance or alignment problem because of the structural deformation due to changing thermal conditions in the space environment. Applications exist in areas such as the OAO, LST, SAS, and any complex system where alignments are critical. It must be emphasized, however, that the methods developed in various areas can be used independently for many engineering applications.

When NASTRAN is used for structural analysis in computing thermally induced deflections or stresses, accurate input data of temperature distribution in the structural members are required. Unfortunately, the existing thermal computer programs using the lumped-node method are limited in size and are incompatible with the basic format of the structural model; the locations of the thermal nodes and the grid points of the NASTRAN structure program generally do not conform.

For this reason, and in order to have a unified computer program, we attempted to develop methods in four areas, which are represented by four tasks in Figure 1. They are all centered around the finite-element method NASTRAN structure program. With respect to task 1, the feasibility of using NASTRAN to solve heat transfer problems is attributed to the mathematical analogy existing between the two systems. This analogy is made clear when both systems are cast in the matrix form via the variational principle (by introducing finite elements and applying the Ritz method).

When variables or terms are properly interpreted, heat transfer problems can be solved by using the familiar vibration equation or the structural dynamics equation shown in Figure 2. The two diagrams in Figure 3 show the basic difference between the lumped-node method and the finite-element method. Average temperature of each area (volume) is

represented by the lumped node at the center in the case of the lumped-node method, but temperatures are represented at the vertices of each element in the case of the finite-element method.

An important advantage of the finite-element approach is that the output of one segment of the program is compatible with the input to the next. Another advantage is the ability to expand the size of the thermal analysis. Example problems solved by the finite-element method have been successfully demonstrated either by direct formulation or by the NASTRAN solution. A few selected examples are illustrated in Figure 4.

The convective and radiating fins of regular and tapered shape are shown in Figures 4(a) and 4(b). Figure 4(c) shows a radiating disk which has internal heat generation  $\dot{q}$  (J/s-m<sup>2</sup>) and circumferential heat input  $q$  (J/s-m). Figure 4(d) shows an L-shaped configuration that was adopted because it was suitable for the application of a number of different sets of boundary conditions. All solutions of the example problems by the finite-element method are in close agreement with the results obtained by the conventional methods of either exact or numerical solutions.

Task 2 is to develop a method of interpolating, through NASTRAN grid points, the displacements which yield deformations at any point on the surface. In Figure 5, the incoming ray hits the deformed surface at  $i'$ , which must be related to the undeformed position  $i$  through the grid point displacements. The problem is then reduced to determining the direction cosines and coordinates at  $i$ . Consequently, the available ray-trace program can be used to obtain information about optical performance.

The method developed allows consideration of the case of an asymmetrically deformed optical surface. The uncertainties in input data in either the case of thermal or structural analysis naturally lead us to doubt the reliability of the computed results.

Task 3 is the thermal variance analysis, and the details of this analysis will be presented in the paper by J. S. Heuser. Task 4 is the structural variance analysis. In summary, STOP has been employed in four areas of investigation. The feasibility of using the finite-element method or of using NASTRAN directly in solving heat transfer problems has been demonstrated successfully. The resulting equations for the interface problem existing

between the structural deformation program and the ray-trace program (which indicates optical performance) are currently being coded into a computer program.

Both the thermal and structural variance problems have been explored and tackled, and work is still continuing. Since the successful results demonstrate the feasibility of this approach, pilot programs are to be implemented that will lead to a group of bona fide general purpose, large-capacity, working, and unified computer programs—the objectives of STOP.

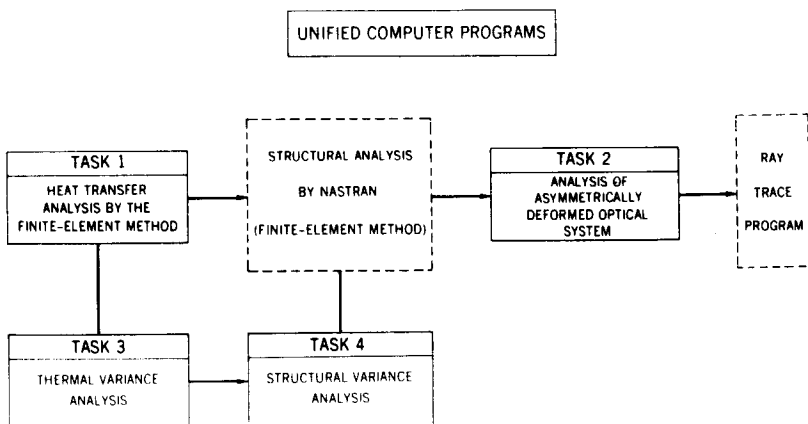


Figure 1—Structural-Thermal-Optical Program (STOP).

$$\begin{array}{c}
 \underbrace{[M] \ddot{X} + [C] \dot{X} + [K] X = F(t)}_{\text{STEADY-STATE HEAT TRANSFER PROBLEM}} \\
 \underbrace{\hspace{10em}}_{\text{TRANSIENT CONDUCTION HEAT TRANSFER PROBLEM}} \\
 \underbrace{\hspace{15em}}_{\text{FICTITIOUS } \begin{Bmatrix} [M] \\ [M] \text{ AND } [C] \end{Bmatrix} \text{ MUST BE USED FOR } \begin{Bmatrix} \text{TRANSIENT-STATE} \\ \text{STEADY-STATE} \end{Bmatrix} \text{ RADIATION-CONDUCTION}} \\
 \text{PROBLEMS WHEN } F(t) = G(t) + N(t) \text{ IS SUBSTITUTED IN NASTRAN} \\
 \text{WHERE } G(t) \text{ REPRESENTS LINEAR TERM AND } N(t) \text{ REPRESENTS NON-LINEAR TERM}
 \end{array}$$

## STRUCTURAL SYSTEM

 $\{X\}$  DISPLACEMENT $\{F\}$  APPLIED LOAD $[K]$  STIFFNESS $[C]$  DAMPING $[M]$  MASS

(EQUIVALENCE)

## THERMAL SYSTEM

TEMPERATURE

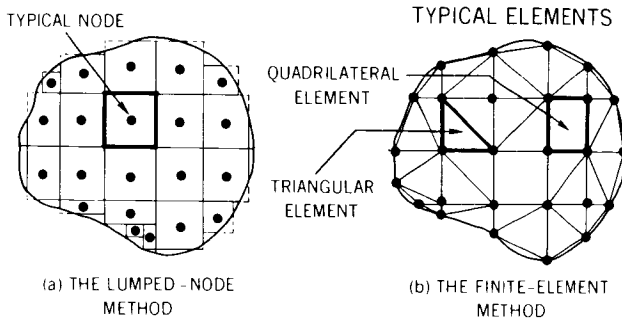
HEAT SOURCE

CONDUCTIVITY

THERMAL CAPACITY

NO EQUIVALENCE

Figure 2—Similarity between structural and thermal systems.



## ADVANTAGES OF USING THE FINITE-ELEMENT METHOD

- COMPATIBILITY
- CAPACITY

Figure 3—Distinction between the lumped-node method and the finite-element method.

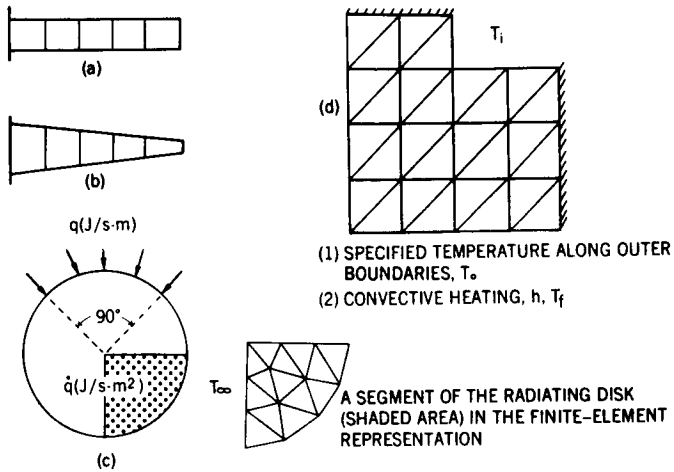


Figure 4—Typical heat transfer problems being solved by the finite-element method.

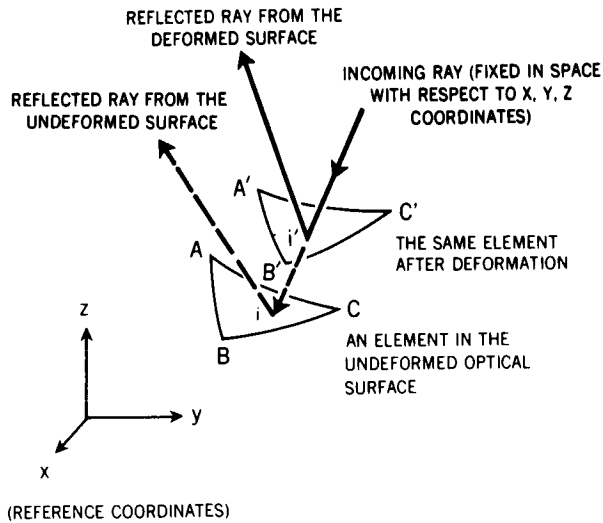


Figure 5—Deviation of reflected rays from an undeformed optical surface and from a deformed optical surface.

## **TWO-DIMENSIONAL FINITE-ELEMENT TEMPERATURE VARIANCE ANALYSIS**

**J. S. Heuser**

The finite-element method (FEM), already used in structural analysis, can be extended to thermal analysis. What I have done is to apply this method to thermal analysis and to formulate a variance analysis of the temperature results. This variance analysis determines the sensitivity of predicted temperatures to uncertainties in input variables.

Conceptually, FEM involves the division of the continuum into a finite number of elements—triangles, for example (see Figure 1). The temperature field within each triangle is described in terms of the temperatures at the vertices. By the use of the variational principle, the integral equation describing thermal potential energy is minimized, yielding a system of algebraic equations. This system may be solved by a computer to yield the desired solution matrix of predicted temperatures.

FEM already has been applied to conductive heat transfer problems, but one important area, essential to space applications, which has received little attention is radiation. I have been able to formulate the radiation equations for two-dimensional elements and have written a computer program for generalized two-dimensional heat transfer which includes this radiation capability. Currently, this program handles 100 finite elements; soon it will be expanded to 300 elements.

The availability of a working thermal finite-element computer program led to an analysis of the effect of input data errors upon the computed results. A temperature variance analysis was undertaken. This study resulted in a sensitivity computer program which uses information about the initial thermal parameters and their associated errors to produce an analysis of the overall temperature variance of the system.

Consider, for example, the simple geometry shown in Figure 2. FEM was applied to this symmetric problem, and the computer program

produced the temperature predictions shown in Figure 3 for the variable nodes 1 to 5. Then the sensitivity computer program was used, with initial and fixed temperature errors of 5, 10, and finally 15 percent assumed. Figure 3 contains the predicted results. For example, the error in the predicted temperature of node 1 may be up to 13.02 K for the 5 percent case. One may draw the conclusion that in order to have less than a 23.0-K error in all predicted temperatures, it is necessary that each of the initial temperature specifications have an error of 10 percent or less.

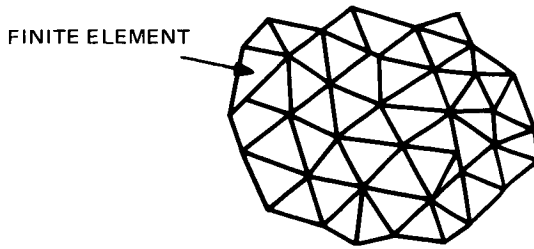
In addition, the sensitivity program produced information showing the relative influence of each thermal parameter upon each predicted temperature. For example, for the sample problem in the 10 percent case, the sensitivity program yielded the values shown in Figure 4.

The following conclusions can be drawn:

(1) In general, all predicted temperatures were influenced most by the values of those temperatures along the fixed boundaries. Errors in thermal simulations, therefore, can be reduced by more accurate specification of these temperatures.

(2) In particular, the temperature error of fixed node 8 greatly affected the temperatures of nodes 1 and 2, affected somewhat node 3, but hardly affected nodes 4 and 5 at all. Likewise, the predicted temperature at node 3 was most affected by the error of node 9.

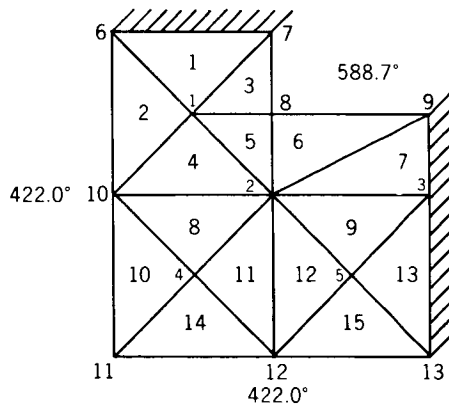
The sensitivity analysis program can be used by the thermal analyst to determine which input parameters contribute most to error in temperatures predicted by the FEM. It can show him how various levels of accuracy in the input data affect the accuracy of the final answers. It is thus a powerful analytical tool that assists one in deciding exactly how close each parameter must be calculated or measured in order to achieve effective results. It also can be used by the spacecraft designer to pinpoint weak links in a thermal design.



## INTEGRAL EQUATION OF THERMAL POTENTIAL ENERGY

$$\begin{aligned}
 \chi = & \iint_A \left[ \frac{1}{2} k_x \left( \frac{\partial T}{\partial x} \right)^2 + \frac{1}{2} k_y \left( \frac{\partial T}{\partial y} \right)^2 - QT + \rho c \frac{\partial T}{\partial t} T \right] dx dy \\
 & + \int_r qT d\Gamma + \int_r \frac{1}{2} hT^2 - T_\infty T d\Gamma \\
 & + \int_r \sigma F_{rs} \left[ \frac{1}{5} \epsilon T_r^5 - \alpha T_s^4 T_r \right] d\Gamma
 \end{aligned}$$

Figure 1—Application of FEM to thermal analysis.

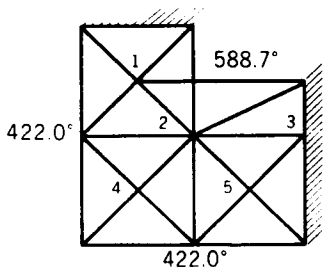


INITIAL TEMPERATURE = 310.9 K

 $K_x = K_y = 1.566 \text{ W/m-K}$        $\rho c = 6.706 \times 10^4 \text{ J/m}^3\text{-K}$  $\Delta K = 0.1566 \text{ (10\%)}$        $\Delta \rho c = 6.706 \times 10^3 \text{ (10\%)}$ 

Figure 2—Heat pipe problem—quarter of a symmetric pipe.

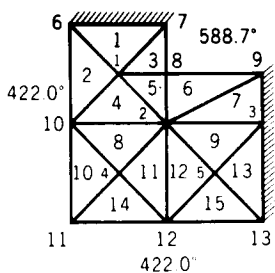
## RESULTS



i	$T_i$ (t=0.0) °K	$T_i$ (t=1.0) °K	$\Delta T_i$ for 5% case K°	$\Delta T_i$ for 10% case K°	$\Delta T_i$ for 15% case K°
1	310.9	482.8	13.02	22.91	33.41
2	310.9	453.5	9.30	17.50	25.93
3	310.9	471.7	10.27	18.84	27.75
4	310.9	421.4	10.75	20.49	30.43
5	310.9	425.1	9.31	17.43	25.78

Figure 3—Comparison of  $\Delta T_i$  for initial variance of cases 5, 10, and 15 percent.

## RESULTS



$s_{ij}$	$T_1$	$T_2$	$T_3$	$T_4$	$T_5$
$K_{y7}$	.00	.04	10.90	.00	.07
$K_{y9}$	.00	.37	2.59	.00	1.52
$\rho_{C9}$	.00	.08	.48	.00	.20
$T(t, \Delta t)1$	43.65	3.94	.07	.01	.00
$T(t, \Delta t)5$	.05	4.97	3.63	.01	21.75
$T(t, \Delta t)8$	81.06	78.20	1.45	.29	.18
$T(t, \Delta t)9$	.26	27.10	197.84	.04	2.21
$T(t, \Delta t)12$	.12	13.13	2.82	108.08	112.82
$T(t)9$	.35	37.17	1.96	.14	.06
$T(t)13$	.00	.15	22.67	.01	7.92

Figure 4—Typical  $[(\partial T / \partial s_{ij}) \Delta s_{ij}]^2$  values.

## A ROTARY ACTUATOR FOR SPACE MISSIONS

E. J. Devine

Since gear reducers have been used for so many years in so many applications, any substantial advance in gear-reduction technology will find widespread application in government and in industry. Within NASA, control moment gyros for space stations are a prime application. Actuators for the Large Space Telescope and planetary missions are others. In industry, the numerical control of machine tools would be one of several logical fields of application.

Presently available rotary actuators (motor-driven gear reducers) do not meet the performance and reliability requirements for the long life space missions of the next decade. Table 1 compares the performance of state-of-the-art rotary actuators to the desired parameters. It may be noted that significant improvements are required in all areas. A new actuator is being developed which promises to meet or exceed these requirements. The design of the actuator is complete, and a breadboard has been fabricated.

The actuator is a unique integrated motor and epicyclic gear reducer. It differs from previous epicyclic reducers in that the motor is functionally integrated with the transmission. (Figure 1 shows the breadboard actuator.)

Figure 2 illustrates the operating principle of the device. The armature of the motor and the ring gear of the transmission are combined in a single element which is driven by the attractive force of a rotating magnetic vector in the stator. For each vector rotation, the ring gear completes an eccentric cycle. Because the number of teeth on the ring gear is different from that on the fixed ground gear, the ring gear rotates a fraction of a revolution. The ring gear simultaneously engages the output gear, which in one eccentric cycle is rotated a fraction of a revolution in the opposite direction. Since the pitch diameters of the two meshes are not the same, there is a resultant differential motion of the output gear.

The advantages of the design are—

Only two bearings are required, and these are on the low speed output shaft.

The fixed ground gear and the output are bridged by a single stiff member (the ring gear), resulting in extremely low windup.

The gear meshes are floating, which allows them to self-center. Since allowance for fixed shaft center distance tolerances is not required, an inherent minimum backlash configuration is achieved.

A high reduction ratio per number of meshes is obtained; for example, 818 to 1 with only 2 meshes.

The new actuator can be driven digitally for ultraprecise numerical control systems, or it may be driven as a brushless dc motor with ideal characteristics for use in linear servomechanisms. This actuator represents a significant advancement in the art of gear reduction.

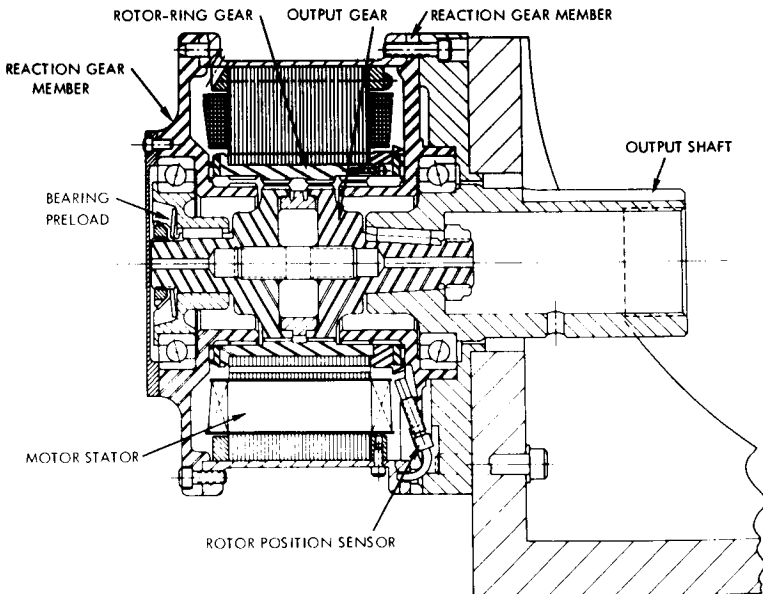


Figure 1—Breadboard actuator.

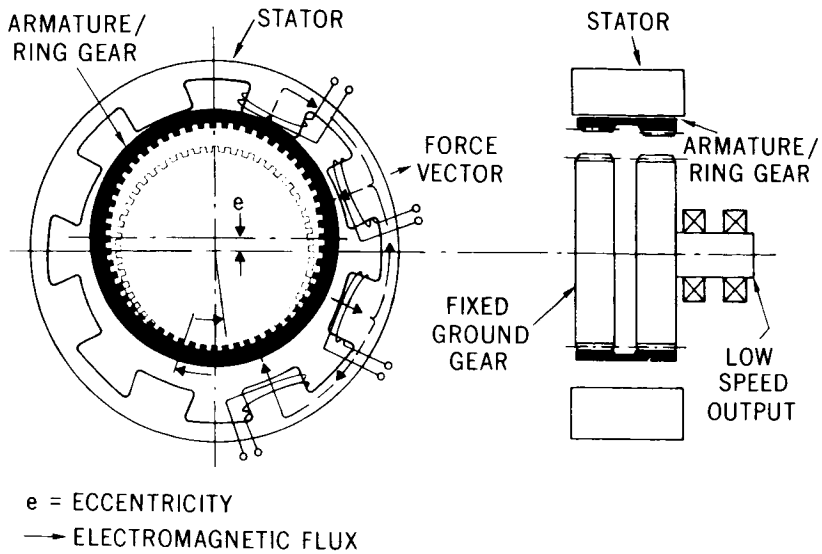


Figure 2—Operating principle of rotary actuator.

Table 1—Performance of rotary actuator compared with requirements.

Parameter	Available*	Required
Inertia ( $\text{kg-m}^2$ )	0.826	0.0826
arc-sec		
Windup	7	3
0.21 N-m		
Backlash (arc-sec)	180	5
Life (yr)	~0.2	1

\*Planetary reducer.

## **HYBRID CIRCUIT MODULES FOR MOTOR COMMUTATION AND CONTROL**

**C. deKramer**

Since the advent of space flight, we have been involved in the development of electromechanical torque systems for the space environment. We felt that three major areas required additional development to assure proper and long-life operation of hardware. These areas are (1) bearings, (2) torque multipliers, and (3) motors (Figure 1).

(1) Since standard contacting bearings present lubrication problems in a hard vacuum, we have developed magnetic bearings which eliminate physical contact between members.

(2) Although direct drive systems are feasible in certain applications, gear reducers have weight and size advantages when used as torque multipliers. We now have developed a rotary actuator which greatly reduces the windup and backlash normally encountered in gear reducers; in addition, the device has an integral motor.

(3) The two motors most widely used with torque-producing devices in space missions are the synchronous hysteresis motor and the permanent-magnet dc motor. The commutator for brushless dc motors will be discussed in this paper.

Since permanent-magnet dc motors normally incorporate brushes and brushes generate electrical noise and have limited life, we developed techniques which eliminate these problems. Although we have made contributions to flight programs in the past in an advisory capacity, we are now prepared to support this advice with space-qualified designs. Brushless motors and torquers have been used in existing programs. Various techniques have been developed on an application-by-application basis. No standard approach or hardware exists and every new application demanded its own development program and flight qualification process.

This past year we have developed circuitry, covering a wide power range, which can be easily qualified to a particular flight specification. We have done this by packaging circuitry, successfully employed in the laboratory, using "thick film" hybrid techniques. It was decided to use a modular approach. The modules developed will be tested in a set of environmental conditions to establish the reliability of the approach.

Figure 2 shows the basic building blocks required for a brushless motor. The power commutator contains the driving circuit for the motor armature and an amplifier that controls the armature current. The position decoder contains digital integrated circuits which receive the signals from the armature position sensors and generate the driving signals for the power commutator in the proper sequence.  $V_{in}$  is the input voltage, which controls the motor current, and the CW and CCW commands determine the rotational direction of the motor. These two blocks are each packaged in a square package, 2.5 cm on a side. Photographs of the units are shown in the upper portion of Figure 2. This is all the hardware required to drive motors with stall currents up to approximately 400 mA, which represents at least a 4:1 weight and volume advantage over previous methods.

To extend the range to about 2.5 A, only two more similar units need to be added. To extend the range to 20 A, these four units should be employed, and the analog mode of current control used in the 2.5 A configuration should be changed to a switching mode of current control. To control the motor in a feedback configuration, one more unit of the same dimensions should be added, and full bidirectional control is obtained.

This approach has resulted in a total system efficiency of 70 percent from 45 mA to 20 A, representing a current ratio of 450:1. Figure 3 shows the three current regions covered. It indicates the load-dependent and the load-independent losses encountered and shows that through the proper choice of system configuration 70 percent efficiency can be maintained.

Again it should be emphasized that we are now prepared to support the advice we have provided in the past with space-flight-qualified designs. This has been accomplished by packaging standard electronic circuitry in hybrid form which can be readily qualified to any required space-flight specification.

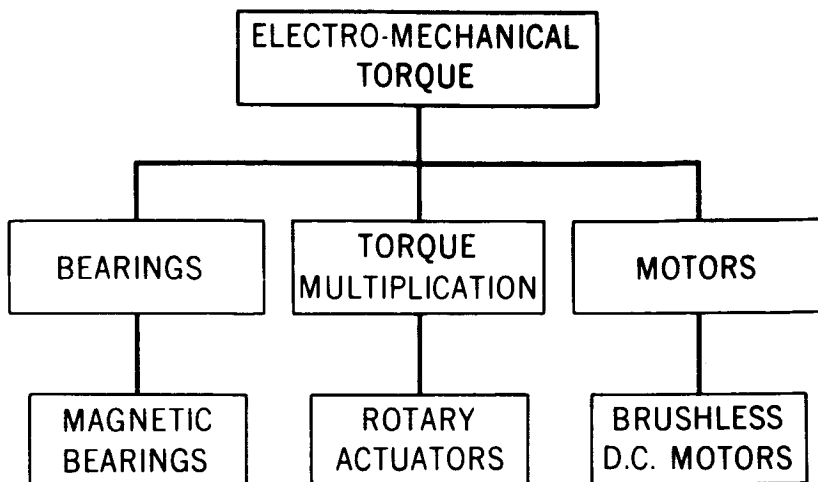


Figure 1--Systems under development.

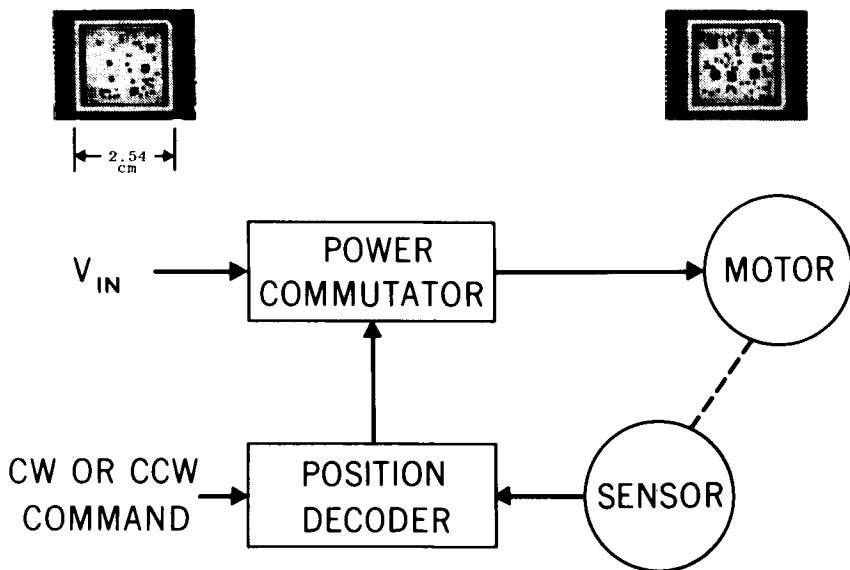


Figure 2--Hybrid circuit commutator.

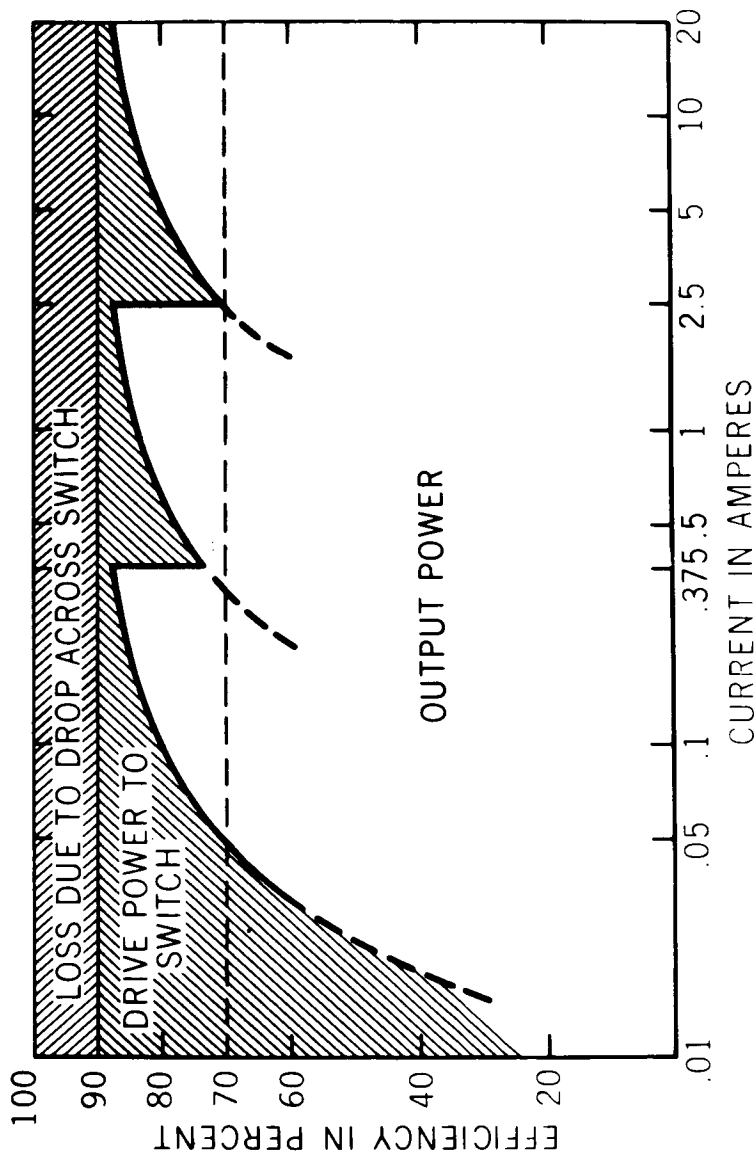


Figure 3—Efficiency versus load current.

## **AUTOMATICALLY ACTIVATED, 300 AMPERE-HOUR SILVER-ZINC CELL**

**Thomas J. Hennigan**

In many long term planetary applications, it is necessary to have additional power available for experiments during planet encounter or landing. To fulfill this requirement, it has been the practice to include some type of battery, usually nickel-cadmium or silver-zinc, for this additional power. Four major problems have arisen:

- (1) Maintenance of the battery during long periods of storage.
- (2) Lack of reliability of the battery with respect to cells in series.
- (3) Degradation of the cells of the battery during the portion of the flight prior to encounter or landing.
- (4) Internal gassing because of chemical or electrochemical reactions, especially in silver-zinc cells.

Development has been geared toward solving these problems. Silver-zinc cells can now be stored for at least five years in the dry state, i.e., without electrolyte. The purpose of our program has been to develop a large, single silver-zinc cell for which the electrolyte would be stored in a separate tank. The cell would be filled with electrolyte, i.e., activated, when the additional power was required.

Figure 1 shows the prototype unit, which consists of a 300-A-hr cell and the electrolyte storage tank. The tank contains approximately 900 cm<sup>3</sup> of electrolyte. Plastic tubing was used on the prototype to permit the flow of electrolyte to the cell. The two terminals on the tank are for activating the filling mechanism.

Figure 2 is a schematic of the cell/tank system, which is referred to as the Unicell. The electrolyte is contained in a collapsible neoprene bellows.

Fluid flow is indicated by arrows. The operation of the unit is as follows:

- (1) When additional power is required, a 3-A pulse is applied to the terminals on the tank.

- (2) The pulse activates an explosive device which forces the knife through a copper diaphragm and at the same time releases the spring which applies force to the piston.

- (3) The piston moves down, thereby collapsing the bellows and forcing the electrolyte into the cell through the hole cut in the diaphragm.

- (4) Any air or gas in the cell is forced into the spring enclosure. However, it is proposed to have a soft vacuum in the cell to eliminate any interference with cell filling.

The purpose of the membranes, or discs shown on the cell assembly, is to diffuse any gases, such as hydrogen or oxygen, that may evolve during cell filling or cell operation.

The proposed application is shown in Figure 3. The main power source would be a solar array or RTG coupled to the load through a conventional converter regulator. Additional power, when required, would be supplied by the Unicell and the low-voltage converter regulator. A converter has been developed to regulate 50 to 100 W at 28 V. The regulation is accurate to 1 percent, and the efficiency is approximately 75 percent (Reference 1). This development eliminates the problems previously discussed:

- (1) The cell does not have to be maintained during flight.

- (2) The control of a single cell is simpler; it is possible to obtain ten times as many cycles from a single cell as from a series of five cells.

- (3) Degradation of the cell before encounter is negligible.

- (4) Internal gassing is essentially eliminated by the excellent charge control afforded by single cell operation. The diffusion membranes control any gassing that may occur.

In addition, it is estimated that the use of a large capacity single cell will result in a 50 percent reduction of battery weight.

#### REFERENCE

1. Pasciutti, Edward R., "Low Voltage Conversion Regulation From Unconventional Primary and Secondary Sources", NASA Technical Memorandum X-63118, January 1968.



Figure 1--Prototype unit.

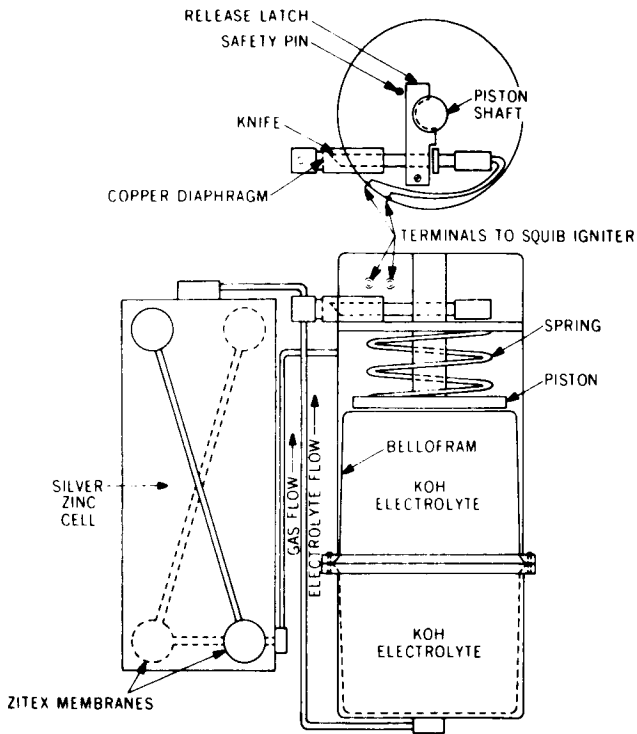


Figure 2—Schematic of Unicell.

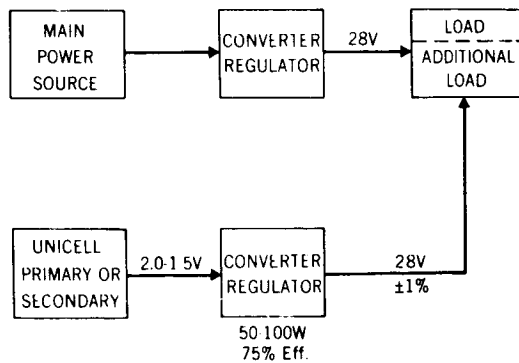


Figure 3—Application of Unicell.

## **SCREENING AND SELECTION OF NICKEL AND CADMIUM CELL PLATES TO IMPROVE UNIFORMITY**

**Gerald Halpert**

The nickel-cadmium battery has long been the backbone of the satellite's power supply. The cells which make up the battery, however, have suffered for a long time from operational problems and lack of uniformity. These problems can be tied to the materials within the cell—plates, separator, electrolyte, etc.—which until recently have been neglected. A study of the plate materials was initiated in which the purpose was to determine which factors affect operation—which could be predicted prior to cell assembly, and which could be determined nondestructively.

From the early measurements and statistical analyses, it became obvious that there was a strong plate-weight to plate-capacity relationship. This was not altogether expected because the complex manufacturing process involves many variables and the active material constitutes only a portion of the weight. However, if processing is controlled, the plate capacity, which is a function of quantity of active material, will also be a function of the plate weight.

Plate weight distribution was determined for plates from a number of manufacturers. The negative plate weight distribution is given in Figure 1. As can be seen, some manufacturers have controlled processing, e.g., Type T-A; others are not as well controlled, e.g., Type E-N. The distribution shown in Figure 1 is similar to the positive plate weight distribution. In order to determine the weight/capacity relationship for a given batch of plates, ten plates were selected at random, physically and chemically characterized, and subjected to electrochemical capacity test. As an example, characteristics of negative plates from OAO Battery 32-33 are given in Figure 2, in which weight versus capacity is plotted. The correlation coefficient is 0.97, which is close to a perfect 1.0, indicating a very close relationship. The low weight plate is not as unusual as it may seem, in that 5 percent of the plates from the group exhibited a low weight. The standard deviation in capacity can be significantly reduced from 0.22 to 0.06 by

removal of this plate. From these data, a regression equation can be determined which allows one to calculate the capacity of a plate without testing, by knowing the weight alone.

The technique was used in the OAO Battery 34-35 cell construction in which a  $\pm 3\frac{1}{2}$  percent weight tolerance limitation was utilized. In Figure 3, a comparison is made between Battery 32-33, in which there was no plate screening, and Battery 34-35. The variation in the 20-A-hr nominal cell capacities is 2.8-A-hr for Battery 32-33 and 1.5 A-hr for Battery 34-35.

In conclusion, the method of weight screening of plates is practical, has the advantage of predicting capacity nondestructively before assembly, utilizes 100 percent sampling, and, hopefully, will result in cost savings. The procedure has been used in the building of batteries for OAO, Viking, the NASA space station, and other satellites, and is an integral part of the interim model specification for high reliability nickel-cadmium cells.

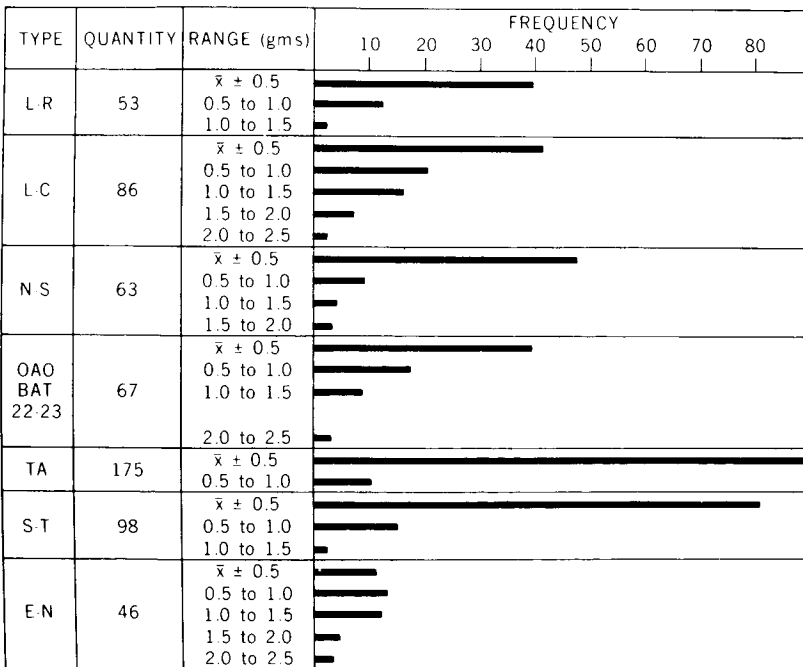


Figure 1—Negative plate weight distribution.

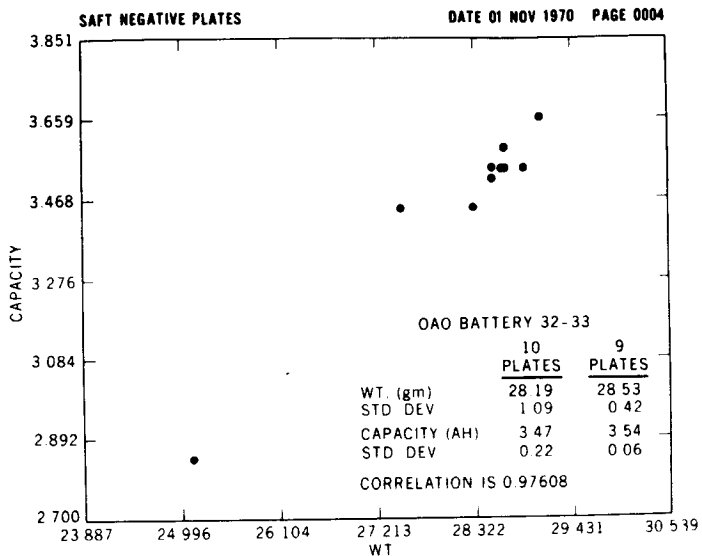
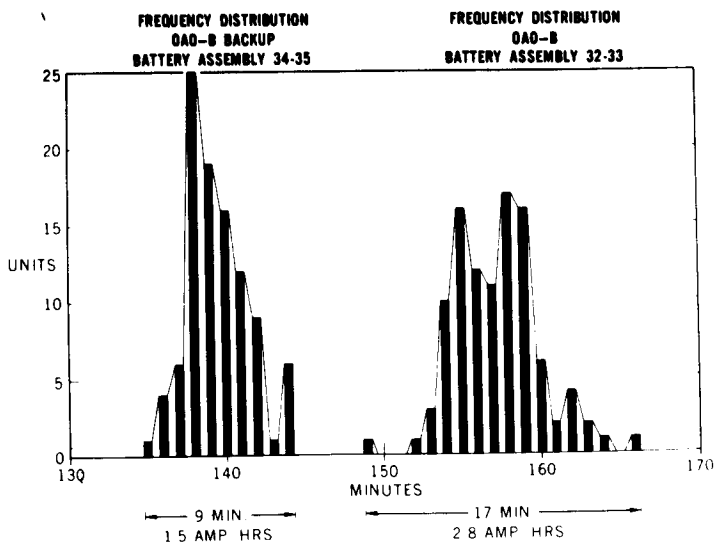


Figure 2—OA0 Battery 32-33 characteristics.

Figure 3—OA0 cell selection cycle (discharge rate  $C/2 = 10$  A).

## THE DEGRADATION OF ALZAK BY SHORT WAVELENGTH ULTRAVIOLET RADIATION\*

Martin J. Donohoe

Roy McIntosh, Jr.

John H. Henninger

There has recently been increasing interest in the damage to thermal control coatings caused by short wavelength ultraviolet radiation. This interest has occurred, in part, as a result of an apparent discrepancy in data returned from a coatings experiment aboard ATS 1 (Reference 1). In addition, certain other findings indicate that, at least for some coatings, degradation appears to be inversely proportional to the wavelength of irradiation (Reference 2). Since the solar spectrum is rich in the vacuum and extreme ultraviolet regions, some experimenters have postulated that this could be a matter of great importance (Reference 3). If such a hypothesis could be demonstrated, it would mean that one more factor should be added to the growing list of requirements for synergistic ground-based testing of spacecraft coatings.

At Goddard Space Flight Center, work has been underway for some time in an attempt to fully characterize the ultraviolet degradation of one of the important thermal coatings, Alzak. Alzak is the designation given to a particular type of anodized and chemically polished aluminum sheet. This material was chosen for the outer skin of the OAO spacecraft because it can be easily worked by ordinary sheet metal techniques and because it has an attractively low ratio of solar absorptance ( $\alpha_S$ ) to hemispherical emittance ( $\epsilon_A$ )—approximately 0.22. Work has been reported previously which showed that the degradation of Alzak was strongly dependent upon the wavelength of irradiation, at least down to  $\approx 220$  nm (Reference 4). The experiments which are described here were designed to provide data down to the solar Lyman- $\alpha$  region (121.6 nm).

The experimental apparatus used in this study is shown in Figure 1. It consists of an irradiation cell and three UV sources with wavelengths at

\*Paper delivered by Martin J. Donohoe.

123.6 nm, 185 nm, 206.2 nm, and 240 nm. Not shown is a DK-2 spectro-reflectometer with an Edwards-type integrating sphere used for in-air reflectance measurements on the sample. A 1½ liter stainless steel vacuum chamber with a side port forms the irradiation cell. The cell is ion pumped with a trapped mechanical roughing pump. All vacuum seals are the copper gasket type, and the valves have Viton elastomer seats. Irradiations take place in the  $10^{-7}$  torr region, measured by an ionization gauge. The irradiation port is either a 5.08-cm diameter sapphire window or a 2.54 cm diameter lithium fluoride window, depending upon the wavelength of irradiation.

The sample was screw mounted on a temperature controlled copper substrate opposite the irradiation port. Sample reflectance measurements were made before, during, and after the irradiations by removing the sample from the chamber. The sample could be removed, replaced, and pumped down within 30 min. No detectable recovery in Alzak took place during this time interval. During the earlier studies, *in situ* reflectance measurements of Alzak damaged by irradiations from a 123.6 nm source and a xenon arc indicated that recovery of damage was negligible when measurements were made within 8 hr after exposure to air. Reflectance measurements were made with an estimated error of  $\pm\frac{1}{2}$  percent due to variations across the sample face.

The UV irradiation sources were two low pressure microwave discharge lamps (krypton and iodine) and a high pressure xenon arc lamp with a bandpass filter centered at 240 nm. The relative spectral outputs of the three sources are shown in Figure 2, together with a solar UV irradiance curve for reference.

The krypton lamp emits three lines, 117 nm, 123.6 nm, and 247 nm. The 117 nm line is weak, being approximately 10 percent of the 123.6 nm line intensity. The 123.6 nm line is the primary irradiating wavelength and is used to simulate the solar Lyman- $\alpha$  line at 121.6 nm. The 2 nm difference between the two lines is assumed to have a negligible effect on the results. The 247 nm line contribution to sample degradation is evaluated by masking half the sample with a sapphire filter to eliminate the 123.6 nm line and pass the 247 nm line. A reflectance measurement on both sample halves then isolates the 247 nm line contribution. The krypton lamp output spectrum is blank from 247 nm to approximately 330 nm. The lamp is

normally run gettered with a cold finger immersed in liquid nitrogen to eliminate contaminant lines. Krypton lamp intensities could be varied by the microwave generator from a fraction of an equivalent Lyman- $\alpha$  sun (i.e., one equivalent Lyman- $\alpha$  sun =  $5 \times 10^{-7}$  W/cm<sup>2</sup>) to approximately 20 equivalent Lyman- $\alpha$  suns. The lithium fluoride window life was greatly reduced at the higher intensities because of the window sealing technique used.

The iodine lamp has a sapphire window and emits a group of lines centered at 185 nm and a strong line at 206.2 nm. The lamp is normally run with a cold finger immersed in ice to maintain the proper pressure in the iodine reservoir shown in Figure 1. The lamp spectrum above 206.2 nm is blank up to 400 nm. Elimination of the degrading contribution of the 185 nm lines, so that only the 206.2 nm line has effect, is achieved with the use of a gas filter of butene-1 (Reference 5). The butene-1 cell absorbs the 185 nm lines while reducing the 206.2 nm line intensity by only 10 percent. The iodine lamp output was variable up to one-half an equivalent sun at 185 nm and 206.2 nm (i.e., 40 Lyman- $\alpha$  suns). The 185 nm lines contributed approximately one-half of the total intensity, the balance being contributed by the 206.2 nm line.

The xenon arc lamp used had a continuum at 240 nm, and the filter centered at 240 nm had a bandpass of 30 nm. Maximum output was approximately equal to one-half an equivalent sun at 240 nm (i.e., 75 Lyman- $\alpha$  suns).

The intensity monitor for all the lamps was a sodium-salicylate-coated photomultiplier (1P28) referenced against a calibrated nitric oxide ionization chamber using the 123.6 nm krypton line. The photomultiplier could be rotated to a position between the sample and the irradiating source. The calibration measurements were performed with the ionization chamber in the sample position as shown in Figure 1. The sodium salicylate quantum efficiency was assumed constant over the wavelength region of interest. This assumption is supported by the literature (Reference 6). The photomultiplier calibration was checked periodically during the experiments and found to remain within 5 percent of the original calibration.

Calculation of equivalent sun irradiance for each source was based on Johnson's data, using a 10 nm bandwidth of each line. The 185 nm lines were treated as one line between 180 nm and 190 nm. Actually the

bandwidth of each line was known from the vacuum monochrometer measurements. Use of the actual bandwidth, 2.5 nm, just increases the equivalent sun hour exposures. Since line sources were used to simulate the Sun's continuum spectrum at select wavelengths, the 10 nm interval was used. Another convenient way of looking at the data would be in terms of Lyman- $\alpha$  suns, since part of the experiment is aimed at studying the effect of Lyman- $\alpha$  radiation.

Figure 3 shows the changes in reflectance at 295 nm of Alzak samples exposed to different irradiating wavelengths. Exposure to 123.6 nm light used to simulate solar Lyman  $\alpha$  produces the slowly developing damage shown in the lowest curve. Exposure to combined 185-206.2 nm light produces the steep curve shown at the left. This curve was constructed from three samples as indicated by the legend.

Shown in Figure 4 is a plot of the percentage of  $\Delta R$  at 295 nm versus wavelength for constant incident energy.

Before discussing the data in Figure 3 and Figure 4, two additional experiments should be mentioned. The first is a single Alzak exposure to 123.6 nm irradiation at an intensity equivalent to that for the 185 nm to 206.2 nm irradiations shown in Figure 3. For a 36.5 hour exposure at  $1.4 \times 10^{-5}$  W/cm<sup>2</sup> (i.e.,  $\approx 30$  times Lyman  $\alpha$ ), Alzak showed a 4 percent  $\Delta R$  at 295 nm compared to the 11 percent shown in Figure 3. The second result is a UV screening test on Alzak using a filtered 2.5 kW Xenon arc lamp (Spectrolab Solar Simulator model X-25). The UV irradiation tests performed through quartz vacuum chamber ports produced at 12 percent  $\Delta R$  in Alzak after 57 equivalent sun hours at a one sun rate. Therefore this sample saw the complete solar spectrum starting at the quartz cutoff of the simulator and vacuum system optics. The UV content (i.e., below 220 nm) for this test was not known, but the point is presented to emphasize the damaging effects of short wavelength UV. The energy output ratio (in W/cm<sup>2</sup>) of the simulator to the microwave discharge lamp is approximately 10,000 to 1.

Two conclusions can be drawn from the data presented. First, on a solar irradiance basis, Alzak is damaged faster and further by 180 to 210 nm radiation than by Lyman  $\alpha$  (see Figure 3). Second, on an equivalent incident energy basis, Lyman  $\alpha$  does less damage than 180-210 nm radiation (see Figure 4). These two points, coupled with the previous studies of Alzak

with radiation above 220 nm, provide a general behavior picture for Alzak degradation: Above approximately 300 nm no degradation is observed for long exposures (100 hr), and below 300 nm increasing degradation with decreasing wavelength is observed. This degradation peaks somewhere between 150-210 nm (on a solar irradiance basis) and reaches a lower value at Lyman- $\alpha$  wavelengths. In addition, most of the damage caused by 180-210 nm radiation occurs within the first 50 hours of exposure and may approximate the damage observed under standard solar irradiation tests.

From the standpoint of solar environmental testing of Alzak, it is evident that Lyman- $\alpha$  radiation need not be included in laboratory testing. Every effort should be made, however, to include radiation between 150-200 nm. Other materials may behave differently and should at least be checked for their behavior under Lyman- $\alpha$  radiation.

At this point in the studies it is only of academic interest to determine the precise shape of the Alzak damage curve because of the large reflectance changes observed when an iodine lamp is used. However, efforts are being made to develop a bromine resonance lamp to provide a line source at 163 nm, a wavelength that will bridge the wavelength interval between the iodine and krypton irradiation sources.

## REFERENCES

1. Reichard, P. J., and Triolo, J., "Progress in Astronautics and Aeronautics", Vol. 20, New York: Academic Press, 1967, p. 491.
2. McIntosh, R., "The Degradation of Alzak as a Function of the Wavelength of Irradiance", Symposium on Coatings in Space, Cincinnati, Ohio, December 1969.
3. Swofford, D. D., Johnson, S. W., and Mangold, V. L., "The Effects of Extreme Ultraviolet on the Optical Properties of Thermal Control Coatings", AIAA Thermophysics Conference, Paper No. 68-783, Los Angeles, Calif., June 1968.
4. McIntosh, R., "The Degradation of Alzak as a Function of the Wavelength of Irradiance", Symposium on Coatings in Space, Cincinnati, Ohio, December 1969.
5. Liuti, G., and Mentall, J. E., "Monochromatic Iodine Lamp", *Rev. Sci. Instr.* 39(11): 1767, Nov. 1968.
6. Samson, J. A. R., "Techniques of Vacuum Ultraviolet Spectroscopy", New York: John Wiley and Sons, 1967, p. 212.

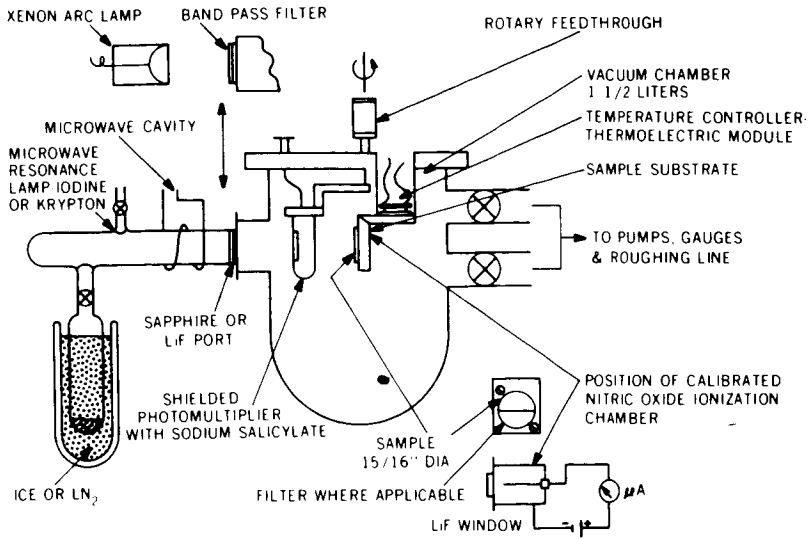


Figure 1—Experimental apparatus.

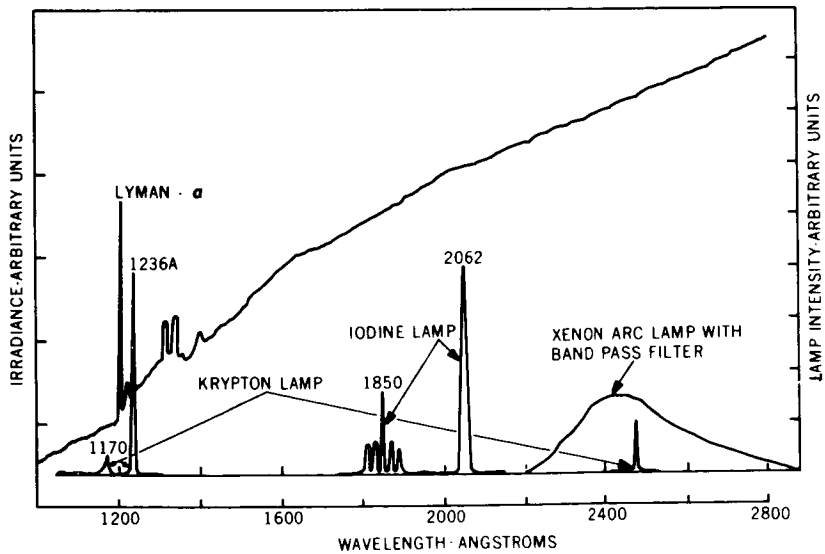


Figure 2—Solar UV spectral irradiance and UV irradiation source spectra.

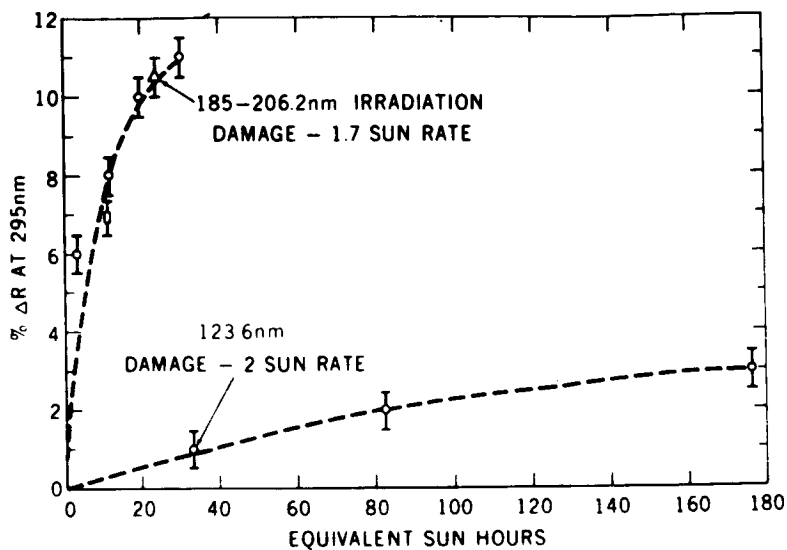


Figure 3—Comparison of Alzak degradation produced by 123.6 nm with 185- to 206.2-nm irradiation.

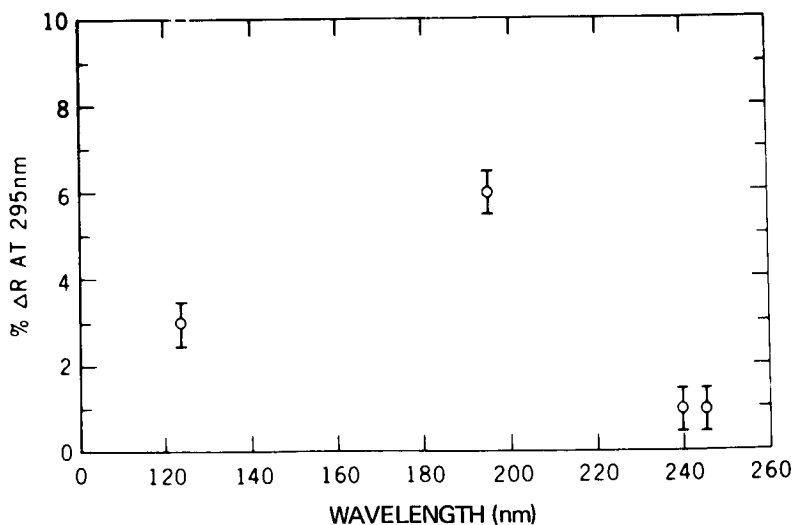


Figure 4—Irradiation damage as a function of wavelength for constant incident energy ( $1 \times 10^{-4} \text{ W/cm}^2 \times \text{time}$ ).

## SPACECRAFT RADIATION ANALYSIS

Dale W. Harris

Radioisotope thermoelectric generators (RTG's) are being used as the primary power supply for the Pioneer F and G spacecraft and for the Viking Lander System. RTG's have also been proposed for deep space missions. The inherent nuclear radiation from the RTG's, which consists of neutrons and gamma photons, will probably have a detrimental effect on the spacecraft electronic systems and the scientific experiments. Consequently, the radiation interface must be accurately defined to minimize its impact on spacecraft design.

To demonstrate the capability for defining the radiation interface, an analysis of an RTG-powered spacecraft was performed. Analyses of this type have been used prior to this calculation to characterize the radiation fields of other spacecraft concepts. However, the accuracy of these analyses is questionable, since analytical methods suitable only for very thick shields were used. Additionally, radiation scattered by the spacecraft structure was not considered previously. In this analysis, the scattered radiation was included, and a Monte Carlo technique was employed to increase the accuracy of the results. The accuracy of this analysis is dependent only on the statistics of the Monte Carlo method and the uncertainty of the material cross sections used in the calculation.

The spacecraft model assumed for the analysis is shown in Figure 1. It is a spin stabilized spacecraft powered by four SNAP-27-type RTG's, and each RTG contains 1300 W of fuel in the form  $\text{PuO}_2$ . The scientific experiment package is positioned 6.1 m from the RTG's to take advantage of the decrease of the radiation field with distance. A magnetometer experiment is similarly located on the opposite side of the spacecraft to provide spin balance. The RTG's are positioned at an angle to the spacecraft so that they "point" toward the experiment package.

The first step in the analysis is to isolate a pair of RTG's from the spacecraft and determine the uncollided (unscattered) radiation fields as a

function of distance from the RTG center line. These results for both neutrons and gamma photons are shown in Figure 2 (dashed lines) as isoflux contours (lines of constant flux). The photon flux results are shown by solid lines. As can be seen in the figure, the photon flux is significantly depressed in the RTG axial direction because of self-shielding. Based on this result, the RTG's were "pointed" toward the science package as shown in Figure 1.

The total flux values (scattered plus unscattered) are then determined by converting the uncollided flux values of Figure 2 into an equivalent RTG surface source and then performing a Monte Carlo analysis for each specific dose point. Three of the dose points considered and the results for each point are shown in Figure 3. Point 1 is located at the geometric center of the spacecraft, point 2 is located at the center of an electronics compartment, and point 3 is located at the science package. For points 1 and 2, the total flux values are listed in the table of Figure 3. The scattered and unscattered flux values are shown separately for point 3 to aid the determination of shield requirements.

These results and the energy distribution of the particle spectra completely define the radiation interface for this spacecraft model. These results can then be used to determine shield requirements. The method of analysis used in this study can also be used to determine shield thicknesses as well as the radiation interface for other spacecraft models.

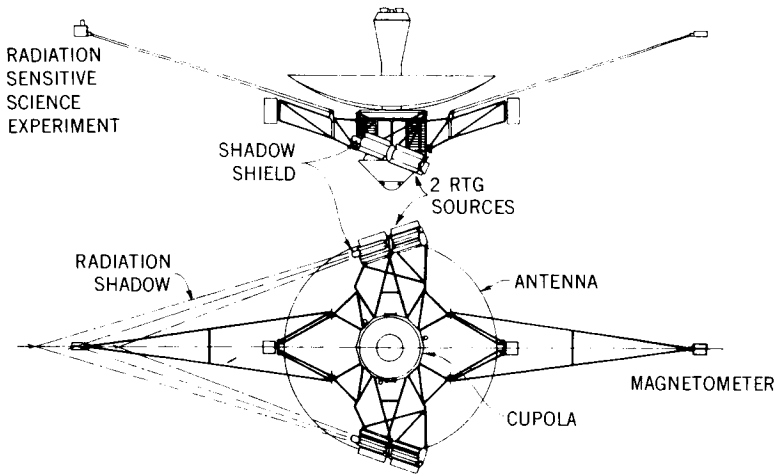


Figure 1—Schematic of typical spacecraft with RTG's.

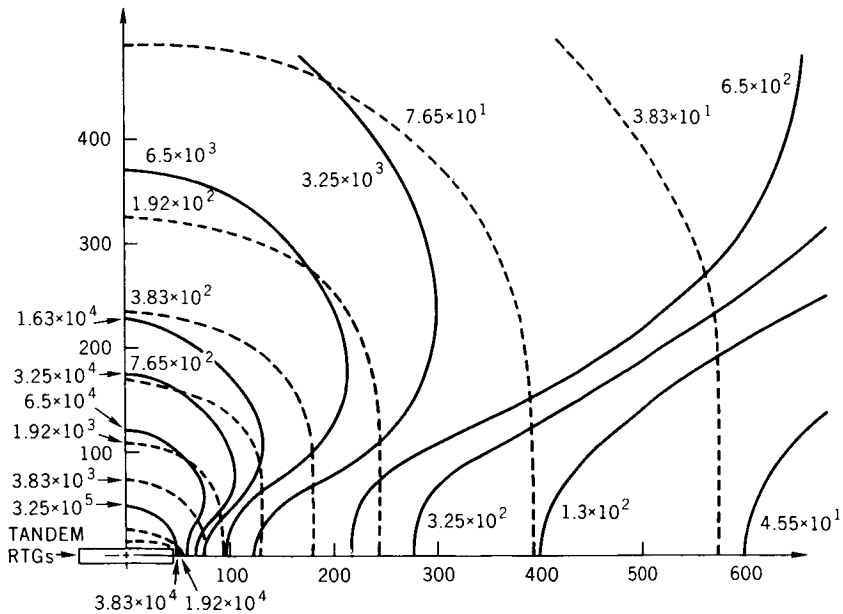
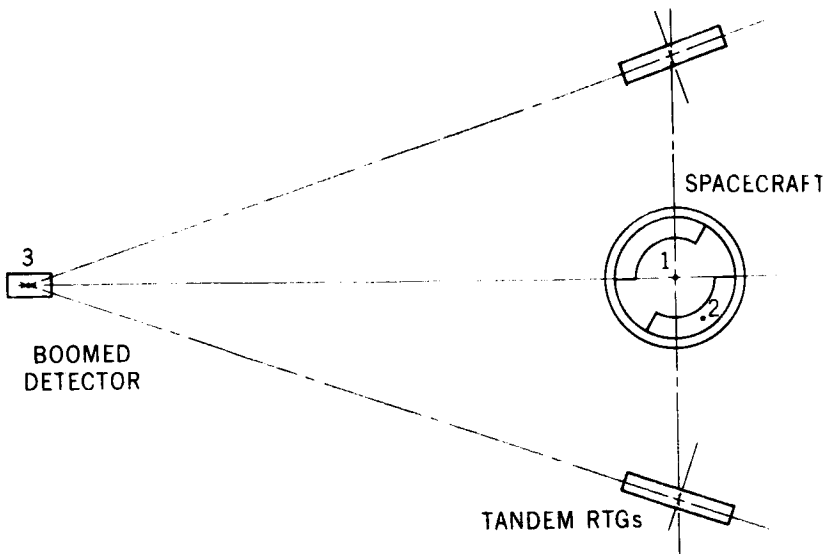


Figure 2—Photon (solid) and neutron (dashed) isoflux contours.



DETECTOR NO	NEUTRONS n/cm <sup>2</sup> -sec	PHOTONS γ/cm <sup>2</sup> -sec
1	9.85 × 10 <sup>1</sup>	5.55 × 10 <sup>3</sup>
2	2.55 × 10 <sup>2</sup>	5.35 × 10 <sup>4</sup>
3 { DIRECT CONTRIBUTION	5.29 × 10 <sup>1</sup>	2.02 × 10 <sup>2</sup>
	4.36 × 10 <sup>0</sup>	1.01 × 10 <sup>1</sup>
	5.73 × 10 <sup>1</sup>	2.12 × 10 <sup>2</sup>

Figure 3--Location of point detectors within the RTG spacecraft system

## A 10.6-MICROMETER LASER RECEIVER RF SUBSYSTEM

D. E. Santarpia

There has been a good deal of effort made to develop optical communication systems. Several of the obvious benefits of these systems are low power requirements, small equipment packaging, and high data rate capability.

These systems also have some problems. One of the problems is how to cope with the exceedingly high Doppler shifts that can be expected. A typical low earth orbit-to-ground station communication link having an optical wavelength of 10.6  $\mu\text{m}$ , which incidentally corresponds to a carrier frequency of  $28 \times 10^{12}$  Hz, has Doppler shifts which will approach 1 GHz at rates to 12 MHz/s.

Such a system, therefore, requires a receiver that has a predetection bandwidth of 1 GHz. Since data bandwidths are typically much smaller than the Doppler shift, the receiver must also be a coherent phase-lock receiver to avoid a degradation of SNR by the detector. In our attempt to develop such a receiver, we asked ourselves two questions.

(1) Can we build a phase-lock receiver capable of tracking 1 GHz in frequency with conventional loop components?

(2) What is the practical loop bandwidth and how does it compare to the theoretical minimum loop bandwidth needed to track 12 MHz/s?

Figure 1 describes a simplified laser receiver, the carrier tracking loop of which has been designed and tested. The laser carrier is optically mixed with a locally generated 10.6- $\mu\text{m}$  signal, thereby translating the received signal to an IF signal that varies between dc and 1 GHz. This signal is fed to a second-order carrier tracking loop that is functionally not unlike the receivers NASA is currently using.

Several components of the loop presented a difficult design challenge. The mixers, signal and LO amplifiers, and the loop VCO were designed to operate over a 1-GHz range. The most significant component developed was the VCO.

The VCO is a conventional transistor LC oscillator that is tuned by a varactor over a 1-GHz range. Normally the tuning range is limited to an upper frequency bound determined by the transistor output capacitance; however, by the use of transmission line techniques, the shunt capacitance is used to advantage, thereby greatly increasing the upper frequency bound and, hence, the tuning range of the oscillator.

Shown in Table 1 are theoretical and measured values of several important loop parameters; the one-sided loop noise bandwidth  $B_L$ , the loop tracking rate  $\Delta f$ , and the loop received signal threshold  $P_{TH}$ . In order to track Doppler rates of 12 MHz/s with a loop having a noiseless VCO, a 5-kHz loop bandwidth is needed. On the basis of a loop SNR of 6 dB and a receiver noise figure of 6 dB, the threshold sensitivity of this loop is -122 dBm. Laboratory tests indicated that a 20-kHz loop was needed to maintain a high lock confidence level. The calculated threshold sensitivity for a 20-kHz loop is -116 dBm. Measurements taken indicate the threshold to be -110 dBm; the 6-dB difference is attributed to the VCO, which is noisy. Data bandwidths are typically 1 MHz or greater, which corresponds to a minimum data threshold of -100 dBm. We can, therefore, still take data 10 dB above receiver threshold.

The object of building this receiver was to determine if conventional phase-lock receivers could operate in a high Doppler environment. I feel that on the basis of the test results obtained, I can confidently give an affirmative answer to this question.

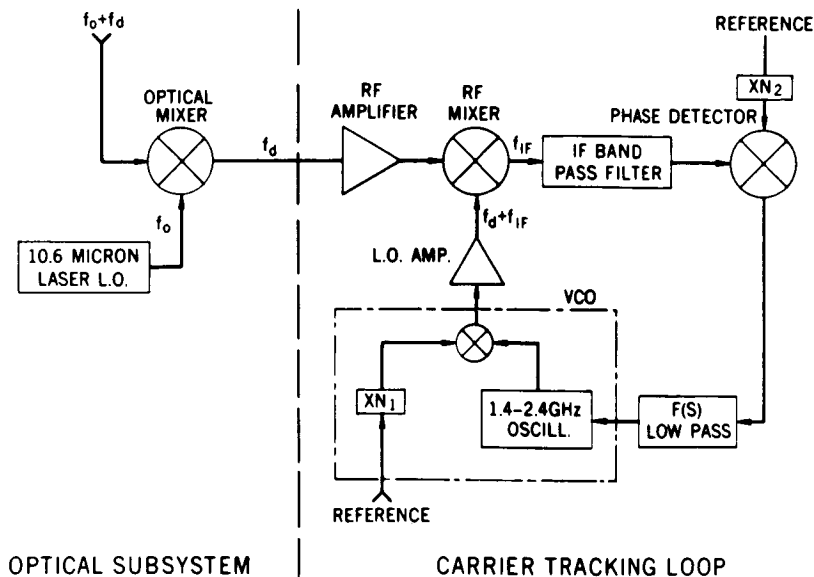


Figure 1—Simplified block diagram of a laser receiver.

Table 1—Tabulated data.

	THEORETICAL (NOISELESS VCO)		MEASURED
LOOP NOISE BANDWIDTH, $B_L$	5 KHz	20 KHz	20 KHz
LOOP SWEEP RATE, $\Delta \dot{f}$	12 MHz/sec	120 MHz/sec	110 MHz/sec
LOOP THRESHOLD SENSITIVITY, $P_{th}$	-122 dbm	-116 dbm	-110 dbm

## KU-BAND HIGH GAIN ANTENNA

**Leonard F. Deerkoski**

Almost a year ago, we made a study of the ground antenna required for support of the Tracking and Data Relay Satellite (TDRS). A 16-GHz carrier with 2-GHz bandwidth and a spacecraft EIRP of +84.5 dBm were assumed for this communication link. These parameters, along with a 10-dB margin for unfavorable weather, established a gain requirement of 70 dB. The three alternative antenna configurations considered are shown in Figure 1.

Using current state-of-the-art technology, a single 29-m-diameter single-aperture antenna with 0.76-mm rms surface tolerance can be built to provide 70-dB gain at 16 GHz. The beamwidth of this antenna would be 0.9-mrad. Assuming that the TDRS has an orbit similar to that of ATS 1 with 35-mrad orbit inclination, the angular velocity of the TDRS at synchronous altitude will exceed 0.005 mrad/s. This velocity is significant with respect to the beamwidth of the antenna, and autotracking is therefore a requirement. The surface tolerance of the reflector causes a 1-dB reduction in gain, resulting in an overall efficiency of 44 percent.

The 70-dB gain can also be achieved using a multiaperture array of antennas on separate pedestals. A four-element array would require 13.4-m-diameter elements. For this diameter, a 0.33-mm rms surface tolerance is within the current state of the art. Each antenna would contain a monopulse feed and provide 55 percent efficiency. The spacing required between array elements to prevent shadowing limits the bandwidth of the array to 250 MHz for 0.5-dB loss at band edge. This bandwidth is far below the required 2 GHz. Use of a two-element array of 19.2-m-diameter elements would extend the bandwidth to 330 MHz, but in either case the multiaperture array of antennas on separate pedestals is not a feasible alternative for meeting the requirements of the TDRS.

The third alternative is the limiting case of the second in which the four-element array is mounted on a common pedestal. This configuration has several unique features. The physical arrangement of the elements

provides the inherent capability for three-channel phase monopulse tracking with only listening feeds in each element. The requirement for only listening feeds provides at least an additional 10 percent efficiency, and only 12.8-m-diameter elements are required. A coherent receiver combines the outputs of the four elements and simultaneously provides the tracking error channels, which are derived from relative phase measurements.

In combining the array elements, the receiver adjusts the phase of each channel to provide coherent addition. The coherence function serves to scan the array pattern of the antenna to point the main beam at the spacecraft at all times. The 3-dB points for the antenna are therefore determined by the element patterns which have a 3-dB beamwidth of 1.74 mrad. The pointing accuracy requirement for this antenna is one-half that required for the single-aperture antenna.

The bandwidth of the array is 3.5 GHz, more than sufficient for TDRS support. The unused area in the center of the array is sufficiently large to permit the addition of a 5.2-m-diameter antenna. This center element would have a gain of 56 dB and could be used for initial acquisition of the spacecraft. When the full array locks onto the spacecraft, this center element would be used for command uplink to the TDRS.

The cost effectiveness of the two feasible alternatives is shown in Figure 2 as a function of gain. Below the required 70-dB gain, the single-aperture antenna is clearly superior. At 70 dB, the cost effectiveness is approximately equivalent for each configuration, with the array becoming superior as the gain requirement increases further.

The differences between the single-aperture antenna and the array become apparent when considering tracking performance. For an antenna located in the vicinity of GSFC, the gain loss due to wind-induced tracking errors is plotted in Figure 3. The probability that wind conditions are sufficient to cause a 3-dB reduction in gain is eight times greater for the single reflector than for the array. This difference results from the ability of the array to scan its radiation pattern within the 3-dB points of the array elements.

Wind-induced tracking errors can be eliminated entirely by enclosing the antenna in a radome. The use of a radome has two disadvantages: (1) it doubles the total system cost and (2) the water film forming on the surface

of the radome under precipitation will reduce the effective gain of the antenna by several decibels. To illustrate this point, the percent probability of exceeding 10 dB reduction in CNR under precipitation is plotted here as a function of elevation of the TDRS (Figure 4). At the minimum elevation angle of concern, the probability is twice as great for the radome enclosed antenna as it is for the exposed antenna. With increasing elevation angle, the difference becomes even greater since the water film losses are essentially constant while the losses due to transmission through the atmosphere decrease rapidly.

In terms of reliability, the array offers significant advantage. If one front end fails or is down for maintenance, the array gain is reduced by only 1.3 dB. With three of the four elements inoperable, the gain reduction is only 4.7 dB. The single-aperture antenna cannot offer such flexibility.

In summary, an exposed four-element array of 12.8-m-diameter elements mounted on a common pedestal is the recommended ground antenna configuration in support of the 2-GHz bandwidth Ku-band downlink from TDRS. The array provides three-channel phase monopulse tracking capability with only listening feeds in each element. The array is as cost effective as a single-aperture antenna and offers significant advantages in tracking and reliability.

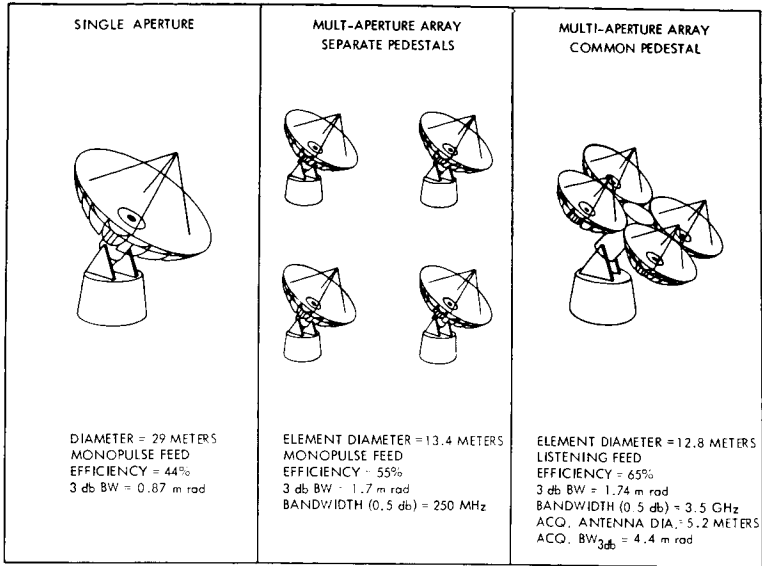


Figure 1—Alternative configurations for TDRS ground antenna.

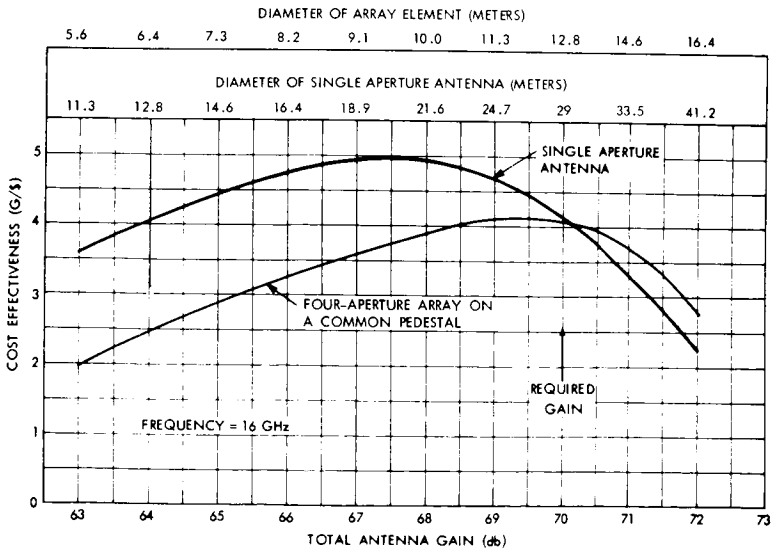


Figure 2—Cost effectiveness.

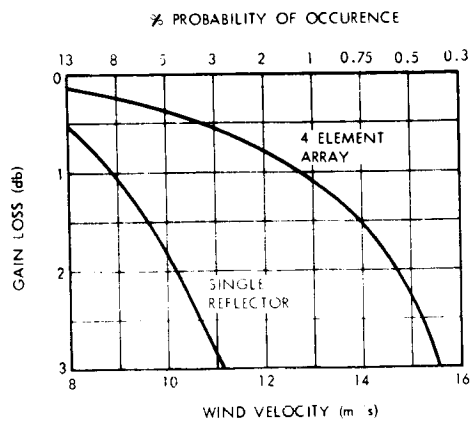


Figure 3--Tracking capability.

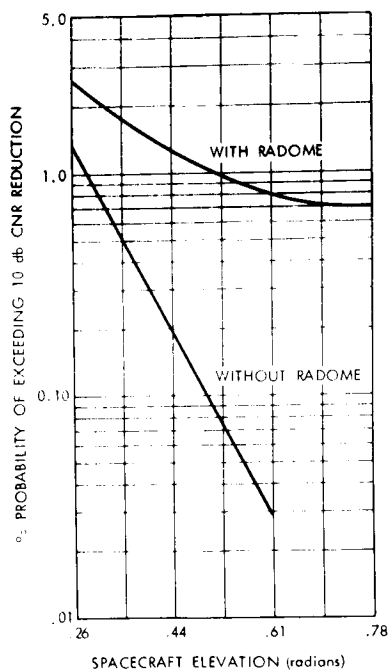


Figure 4--Effects of radome.

## DISCRETE COMPONENT S-BAND POWER AMPLIFIER

Arthur F. Block

Spacecraft S-band power amplifier development in recent years has faced the problem of developing power over 5 W without encountering undesirable "turn-on" characteristics. Small reductions of either RF driving power or applied dc voltage developed an unacceptably large power output drop. Aging of components in either the RF drive hardware or power source circuitry of a spacecraft could result in a catastrophic loss of output power.

The amplifier shown in Figure 1 has overcome this problem. It achieves stability by use of moderate  $Q$  input and output circuits. Previously designed amplifiers have used cavity resonators that suffered from high  $Q$ . Another frequently tried approach using microstrip or stripline has exhibited inefficiency and reduced gain. The discrete component amplifier uses distributed inductance and small piston capacitors for resonance and impedance matching of the transistor to 50-ohm input and output.

The amplifier is fabricated by milling an aluminum cube. Piston capacitors can be seen on either side of the transistor. The transistor is silver soldered to the plated cube that is  $2\frac{1}{2}$  cm on a side and weighs 34.3 g in nickel-plated aluminum and 93.9 g in copper.

The output power exceeds 8 W, and the collector efficiency is over 40 percent; gain is about 9 dB. Turn-on characteristics are shown in Figure 2. The linearity exhibited has allowed this design to be used on the Nimbus Tracking and Data Relay Experiment. Here, dc voltage level applied to the output amplifier will be varied on command providing power outputs of 2, 4, or 8 W. Two similar stages are cascaded on Nimbus. The pair combined produce 19 dB gain with 36 percent efficiency.

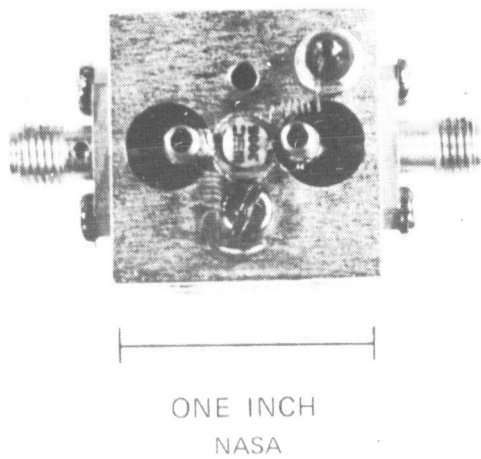


Figure 1—S-band discrete component amplifier (designed and developed by L. Line and R. Rippy).

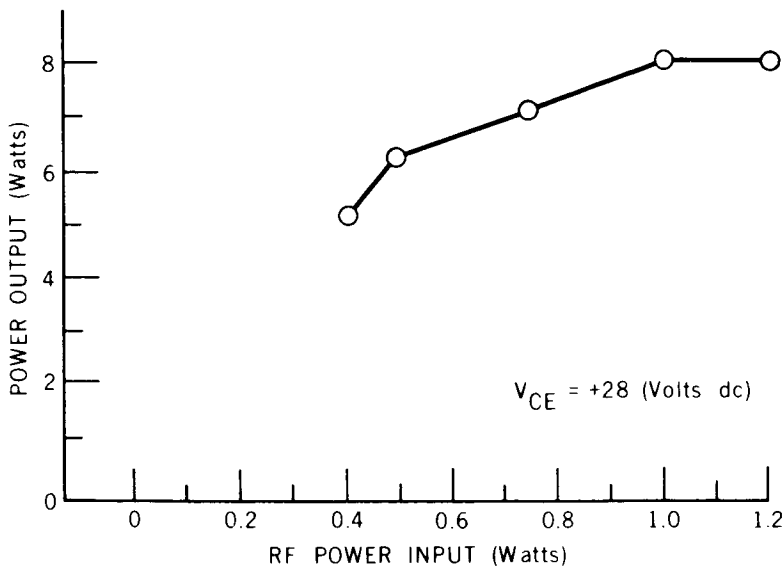
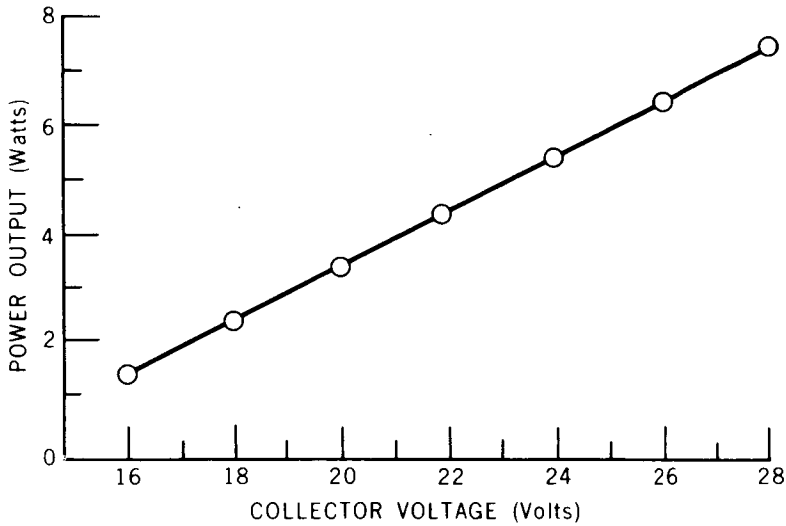


Figure 2—Discrete component S-band power amplifier at 2.3 GHz.

## **FLIGHT DATA SYSTEMS USING LSI P-CHANNEL MOSFETS**

**James H. Trainor**

For a number of years, we have carried out a research and development program concerned with the general improvement of space flight signal and data processing systems for experiments. We are concerned with components; linear circuitry; digital circuitry; and special effects due to noise suppression, radiation damage, and so on. For instance, as a result of our efforts, there is now available on the GSFC Preferred Parts List a line of very low power, complementary bipolar circuitry using hybrid thick-film techniques.

For the last two years, we have been helping to support the continuing development and expansion of a series of P-channel MOSFET circuits which had its beginnings in the IMP program. The GSFC engineers primarily responsible are Hosea White and Don Lokerson. The commercial manufacturer of these custom devices is American Micro-Systems Inc. (AMI).

The evolution of these circuits from discrete devices to the present LSI devices, or bugs, some of which have more than 1000 transistors on a chip, and the effects this advanced circuitry has had on experiment and spacecraft design are really astounding. Figure 1 tells a qualitative story using the IMP program as an example. Across the top of the figure, data flow is traced from the experiment sensors through the data system to the transmitter, function by function. Four spacecraft examples are shown with light gray denoting the experiment contribution or responsibility and dark gray denoting the spacecraft data system responsibility. The vertical extent in a given block is intended to indicate the relative functional complexity. Several features are to be noted:

- (1) As one has learned more about what is going on in space, the sensor systems and their immediate electronics have become far more sophisticated and complex.

(2) On IMP I, a large increase in sophisticated analog processing was noted, as was a dramatic increase in the demands and abilities of the digital system.

(3) On IMP H and IMP J, more useful MOSFET bugs were available, and the spacecraft engineers were able to simplify the experiments even more.

(4) It is interesting to note that if we were to include the proposed IMP KK' here, or Pioneer F and Pioneer G, or Helios A and Helios B experiments, for instance, the picture would change markedly. Much of the dark gray would be light gray because a sophisticated set of bugs or circuits is available. Experimenters can build their own sophisticated special purpose data system, and the spacecraft will revert back to central functions typical of IMP D and IMP E, for instance.

Figure 2 adds further detail to what I have been saying. Horizontally, years from 1960 to 1971 are plotted, and several satellite milestones are shown. The left ordinate gives the number of cans, flatpacs, or bugs in the data system and is to be used with the circular data points and the thin narrow curve. The right ordinate gives the number of semiconductor devices in the system and is to be used with the diamond-shaped data points and the heavy curve.

The can count increased rapidly at first, to approximately 1000 to 1500 devices, but has since decreased. The number of semiconductors has increased by more than three orders of magnitude. The IMP I data and encoding system has approximately 328,000 semiconductors, and IMP H will have approximately 500,000. In this time, there has been an evolution from discrete transistors to several transistors in a can to MSI to LSI. The spacecraft capability and complexity have increased markedly, but because of parallel data paths and the high reliability of these parts, the reliability is probably much higher. Currently, the IMP program has shown greater than  $700 \times 10^6$  device-hours in orbit with an absolute maximum of 2 device failures.

Previously, I had referred to the next step in this evolution being experiments having their own extensive data systems. At least three experiments on Pioneer F and Pioneer G are using these devices, and we are also using them on Helios A and Helios B and expect to use them on HEAO.

For Helios, our experiment data system will use approximately 130 bugs and have a semiconductor count of greater than 100,000. It will weigh less than 1 N and use less than 1.2 W. This system probably will use more transistors than all the rest of the spacecraft combined.

Table 1 is a summary showing the size of the family available, the part numbers, and GSFC drawing numbers. In addition to funding the TREE and PHA bugs, an additional LSI bug is now being funded which will be called the Helios bug. Up to 12 bits can be entered, either serially or in parallel, and then shifted out. The availability of a family of low weight, very low power, very reliable parts that are also low cost (~\$150 per bug with NASA specifications) is a major advance.

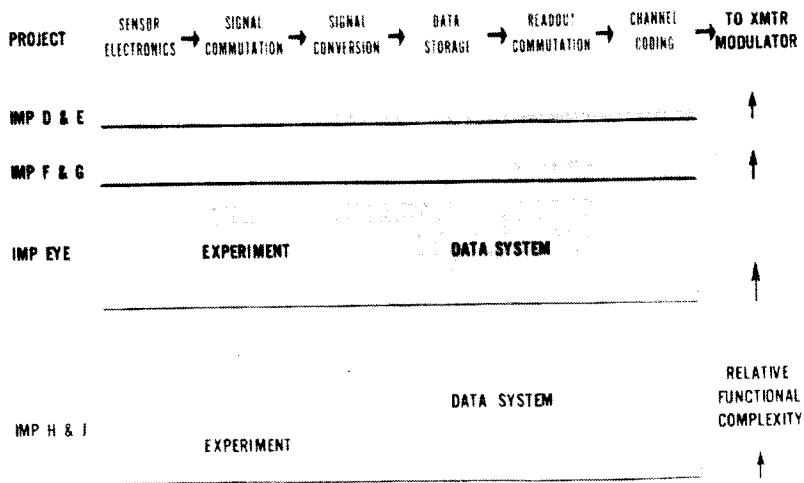


Figure 1—Spacecraft data flow.

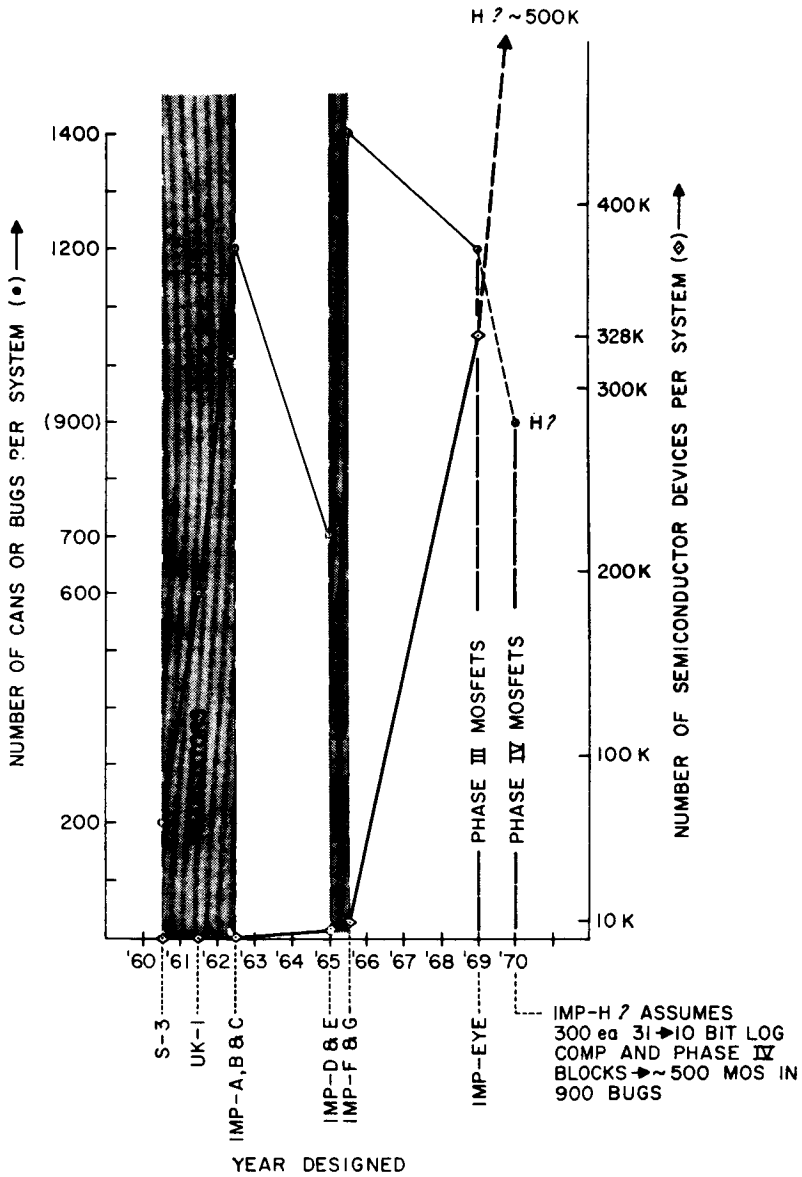


Figure 2—Evolution of encoding system.

Table 1—MOSFET block part numbers and drawing numbers.

BLOCK NAME	AMI #	GSFC DRAWING #
PHASE I BLOCKS		
Logic Block	SC-1128B	GD-1154-025 (2 sheets)
Logic Block	SC-1129B	
Logic Block	SC-1173B	
Binary Block	SC-1149B	
PHASE III BLOCKS		
ATXC Floator Block	C-1275	GP-1154-042
ATX Registers Block	C-1276	(9 sheets)
10 Channel Switch	S-1304	GD-1154-044
Universal 4 Bit	S-1304	GD-1154-043
MOS Commutator		
Outside World 4 Bit	S-1307	GD-1154-048
MOS Commutator		
PHASE IV BLOCKS		
16 Bit SR with Storage	C-1308	GE-1281-452
MARS BUG	C-1375	GE-1154-047
TREE BUG	C-1487	GE-1281-454
PHA BUG	C-1652	GE-1281-455
HELIOS BUG	--	GE-1281-456

## TELEMETRY REMOTE MODULES

J. R. Silverman

The Telemetry Remote Module development has been an outgrowth of a GSFC-initiated investigation into methods of improving data gathering capabilities. This effort has provided, after an initial group of competitive studies, a fully operational breadboard and engineering model which meets all design goals.

The technique I am discussing forms the basis for a decentralized telemetry system which employs small, low powered modules capable of distributing the multiplexer input gates around the spacecraft rather than concentrating them in one centralized location. These modules operate, in essence, as a harness reducer, allowing data to be transmitted back to a central control core for inclusion in the telemetry bit stream.

The remote module developed in this effort is shown in Figure 1. Each unit is capable of accepting 32 data points in various combinations of analog and/or digital input information. These inputs can be controlled either through a hardwired or programable central control core sequence. Each module weighs 113 g, occupies 98 cm<sup>3</sup>, and requires a maximum power of 1.3 W during the interrogate mode.

System applications of the remote modules and several of the reasons why this development has been pursued and the advantages which can be derived from remote modules are illustrated in Figure 2. The central control core and gate address generator serve to generate the sequence of addresses for the data points being sampled and for the formatting of data. These items are not per se part of this development. Also, the total weights, size, and power parameters for both a remote module decentralized system and a centralized system, with the same basic data gathering capabilities, are roughly equivalent.

A prime advantage in the utilization of decentralized remote modules is a reduction in the number of interconnecting wires between the central

control core and the data inputs. Where previously each of the 32 data inputs would require separate harness wires, the use of remote module permits the 32 lines previously required to be reduced to five. The weight savings alone for major spacecraft requiring long runs can be quite significant. There is also a more subtle advantage in that additional flexibility in specifying harness wire interface requirements is achieved.

Another advantage of the remote module is that data gathering capabilities can be tailored more closely to user requirements. Figure 2 illustrates how this building-block approach of one or more remote modules per user could be implemented.

The last item I will discuss here is the universality which has been built into the system. This is typified by the capability of intermixing inputs in several combinations of analog or digital data. Flexibility is also designed into the system's ability to accept analog data in the range from +10 to -10 V. The data rate also provides flexibility in that it can vary from 0 to 3200 channels per second with a digital resolution of 8 bits per word.

The above discussion has been an attempt to summarize a development that has produced a system which meets several fundamental spacecraft needs: standardization, increase in system simplicity, and greater flexibility in the use of telemetry systems.

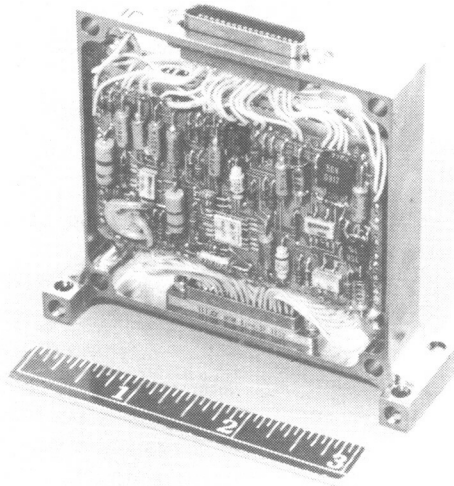


Figure 1—Engineering model of remote module.

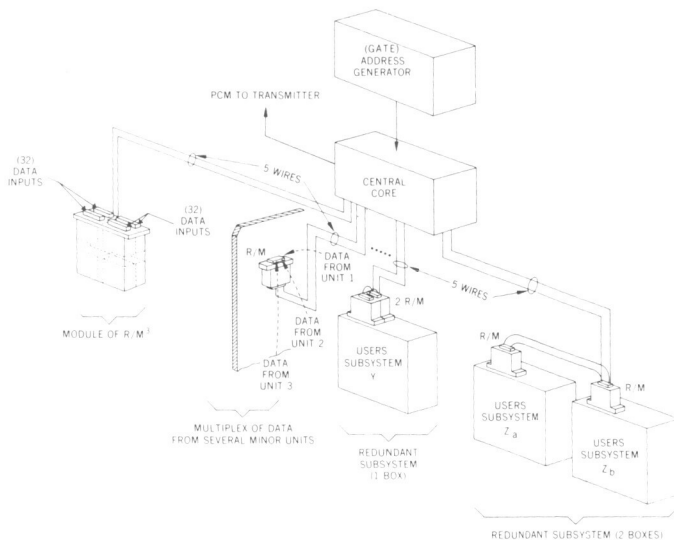


Figure 2—Remote module implementation.

## **AN ON-BOARD PROCESSOR (OBP) FOR OAO C**

**Raymond Hartenstein**

This report concerns a stored program computer for spacecraft use and its application on OAO C. The computer, referred to as OBP-I, is a medium scale, parallel machine and has a memory capacity of 16,384 words of 18 bits each. It possesses a comprehensive instruction repertoire and requires 45 W, including the dc-to-dc converter. It operates at a 500-kHz rate and executes add instructions in 10  $\mu$ s. The primary functions of OBP-I on OAO C will be auxiliary command storage, spacecraft monitoring and malfunction reporting, data compression and status summary, and possible performance of emergency corrective action for certain anomalous situations. Although the OBP-I will be initially applied to the OAO series of spacecraft, the computer was designed to have features which would fulfill the requirements of a variety of future scientific satellites. The system is modular and consists, in a minimum configuration, of one central processor unit (CPU), two 4096-word memory units, and one input/output (I/O) unit. Figure 1 shows how these units are connected to a common and redundant data and address bus, with the minimum system shown by solid lines. Several unpowered spare functional modules, shown by dotted lines, can be attached to the bus to extend the life of the system.

The CPU contains a fully parallel adder and parallel data transfers. Data words and instructions are 18 bits in length with negative numbers being represented in two's complement form. There are 50 instructions in the repertoire, 30 of which require an operand fetch; the other 20 instructions have a minor operation code in the address field of the instruction word. A storage limit register reserves a block of memory in which the operating program may write; such a block has an increment of 128 words.

Each memory module has a capacity of 4096 18-bit words and uses a conventional destructive read-out core as the storage element. The most significant feature of the device is that it is capable of being completely power-switched on a cycle-by-cycle basis and consumes less than 150 mW in the standby mode. Several memory modules may be randomly addressed

without paying the price of large power usage. For the OAO C application, the computer will have four memory modules for a total capacity of 16,384 words.

The important design feature of the I/O is that it has no direct data connection with the CPU. All data flow between the two units must pass through memory by way of the memory data bus. This method serves to minimize the number of connections required between modules and allows the easy interconnection of spare CPU, I/O, and memory modules. Also, by use of "cycle-steal" channels, the I/O can operate in a manner that is independent of the CPU, and any portion of memory can be loaded or dumped even though the CPU is either unpowered or executing a program.

Figure 2 shows the specific data interfaces between the various spacecraft subsystems and the computer. Inputs to the computer are commands from the primary processor and data storage unit (PPDS) and spacecraft data from the spacecraft data handling equipment. Outputs are commands to the PPDS, 30 bits per telemetry frame to the spacecraft data handling equipment, memory dumps at 50 K bits per second to wideband telemetry, three analog lines to the fine wheel and jet control, and a single analog voltage line to the power control unit.

The OBP-I sends commands to the PPDS by simulating the command receiver and outputting the 1042 bits per second command message. With this connection (made through a set of relay contacts) the computer can send commands to all spacecraft subsystems and experiments. The 1042 bits per second spacecraft data input provides computer programs with data relating to thermal conditions of all subsystems, charge and discharge rates of power subsystem, gimbal angle errors, spacecraft aspect from sun sensors, rate information from inertial reference unit, course and fine momentum wheel rates, jet gas usage, magnetometer outputs, and the status of many discrete functions. Some of the possible applications of these data are discussed next.

The computer outputs a 30-bit status word to telemetry each 1.6 second frame. These bits can be defined in a variety of ways. One type of message will consist of the compressed sensor data. For some sensors, OBP-I may compute and telemeter the high, low, or mean values for the preceding orbit. For other sensors, data may be telemetered only if the values exceed

some predefined limit. Another message will contain the results of a self-test computer program.

For OBP-I memory dumps, up to 4096 word blocks may be transmitted to ground at a 50 K bits per second rate. This high frequency data link will be used to verify both computer program loads and auxiliary command loads. Another use will be the transmission of summary messages which relate to status and usage of various spacecraft subsystems during the previous orbit. For the first time, control center equipment can display historical data almost immediately after acquisition from the spacecraft by a ground station. This is of particular interest to a spacecraft operator in situations where action must be taken to correct an abnormal onboard condition.

Outputs of three, 6-bit, digital-to-analog converters are connected through relay contacts to the fine momentum wheels. In this way, the computer can control spacecraft rotation about the roll, pitch, and yaw axes. For safety, the connection of these analog signals can be opened or closed by ground command. Although normal spacecraft operation will not require this interface, the computer may be called upon to control spacecraft attitude in the event of certain equipment failures in the stabilization and control subsystem or to demonstrate experimentally the application of the computer to the control system. The output of a 6-bit, digital-to-analog converter is connected through a relay to the power control unit. With this connection, the computer can control the power regulator duty cycle and thereby influence the operating point on the solar array voltage-current characteristic curve. By considering factors such as sun angle and solar cell temperature, the computer can match load to source at maximum power. This interface may be enabled or disabled by ground command.

The auxiliary command memory expands the storage capacity from 256 to 1380 commands. The increase in capacity serves to reduce the required frequency of command loads from 4 or 5 per day to 1 per day which, in turn, means the loads can be transmitted from one ground station instead of several. For this auxiliary command memory function, 4096 locations of OBP-I memory are required to store the 1024 additional OAO commands.

Monitor and malfunction detection consists of the OBP-I acting as a ground station when the spacecraft is not in contact with a station. In one

case, it monitors the commands issued by the PPDS and the response of the stabilization and control components and detects possible malfunctions. In a second case, the computer can monitor spacecraft and experiment equipment temperatures and compare them with maximum limits of dynamic models. Finally, the computer can perform energy "bookkeeping" to sense battery rundown or detect failure in other prime electrical power system hardware.

The emergency action functions would be actions taken in response to diagnosed malfunctions which, if left uncompensated for a short period of time, could cause mission failure. Emergency action could be taken if the temperature of any subsystem exceeds a maximum limit. Here, equipment and/or heaters could be commanded off. In the case of overheating of experiment optical structures, the spacecraft could be reoriented. In the case of abnormal battery discharge, the computer could command equipment shutdown and/or spacecraft reorientation to the sunbathing attitude.

OBP-I can assemble special telemetry messages that give a rapid time history of spacecraft system status during the previous orbit. Changes in status would be reported early in a contact so controllers can obtain a "snapshot" of spacecraft conditions. The malfunctions, if any, would be reported as a part of this quick picture, and the emergency action taken, if any, would be indicated.

There are a large number of failure modes which would leave the spacecraft ineffective if a computer were not on board to substitute an equivalent function. Since failure modes cannot be predicted, the routines required to provide a workaround capability will not be a part of any standard operating program. The backup capability is considered significant, however, since it could have a large and positive impact on the life of the mission.

Figure 3 is a picture of the operating flight hardware as it now exists ready for integration with the OAO C spacecraft. We are already looking ahead to an advanced OBP which could be produced in the 1972-1973 time frame and which would be significantly smaller and would consume considerably less power, making OBP readily adaptable to even the smaller spacecraft programs.

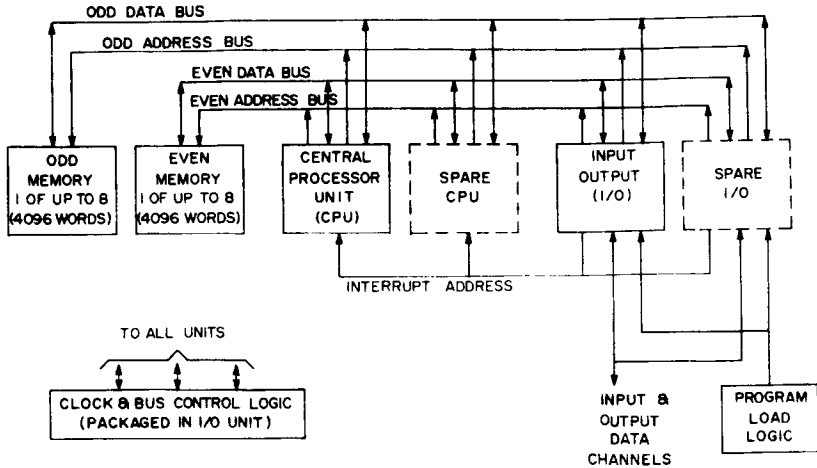


Figure 1--Functional block diagram of on-board processor.

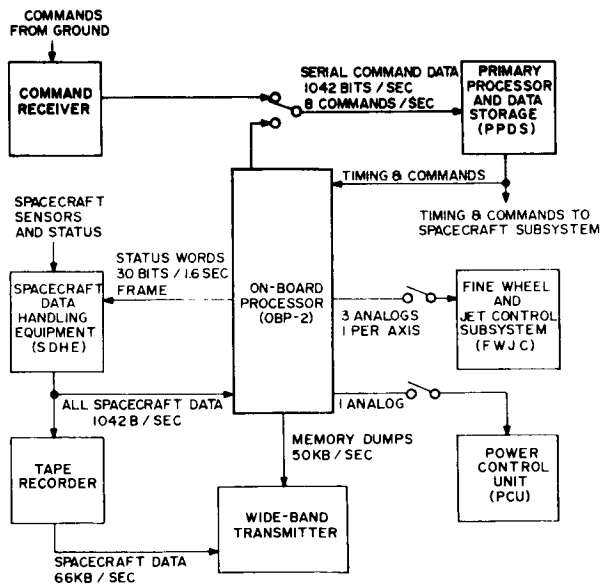


Figure 2--OBP-1 interface with OAO C subsystems.

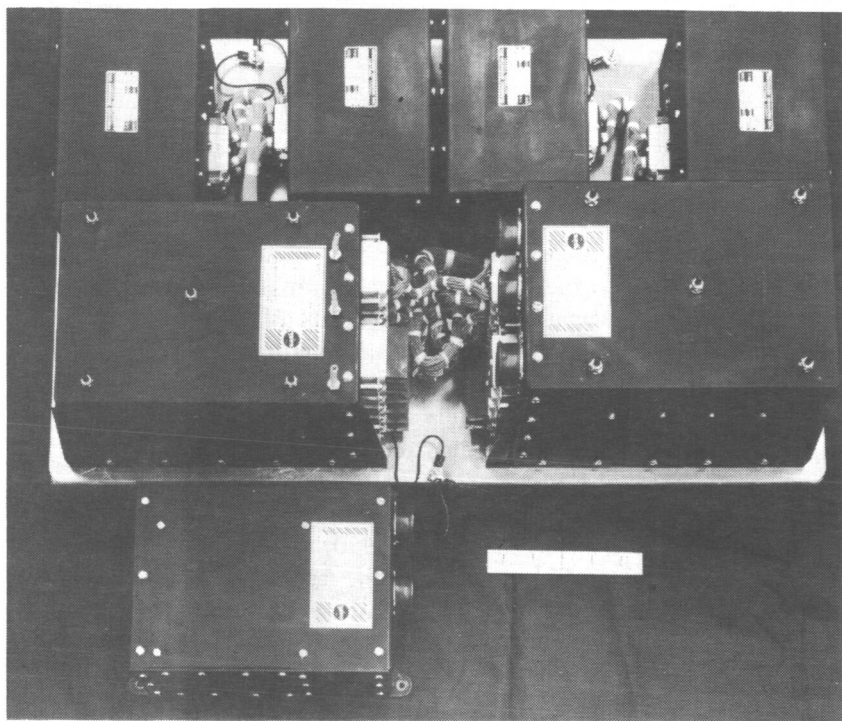


Figure 3—OBP-I flight hardware.

## **THE NIMBUS 4 IRLS METEOROLOGICAL EXPERIMENT**

**Charles E. Cote**

A meteorological experiment designed to provide scientists with their first direct look at the upper atmosphere in the tropical regions of the Earth is currently being conducted by the Nimbus 4 Interrogation, Recording, and Location System (IRLS). The IRLS is designed to locate and collect data from remote instrumented platforms deployed on a global scale. These capabilities are being utilized to obtain measurements of upper atmospheric parameters through the tracking of free-floating, constant level balloons flying at altitudes of 20.5 and 24.1 km (50 and 30 mb pressure, respectively). Operations commenced in May 1970, and, during the following months, a total of 26 balloons carrying specially designed Balloon Interrogation Packages (BIP's) were launched from a site established at Ascension Island in the southern hemisphere. This site was selected to enable insertion of balloons into the biennial circulations, which are the subject of study in the experiment. To date over 1500 locations have been obtained from points around the globe; the data have provided information which will be the subject of study for many years.

The IRLS concept is shown in Figure 1. The basic elements of the system include a ground acquisition and command station, the Nimbus satellite, and the remote platforms. In operation, addresses of platforms expected in view are programed into the satellite on an orbit-by-orbit basis from the central ground station. As orbital time elapses, interrogations are executed in ordered sequence. A minimum of two interrogations per platform are required for location computation, which is derived through range-range techniques. Simultaneous with ranging operations, sensory data sampled by the platform are transmitted to the satellite for storage and readout at the termination of the orbit. The IRLS was first flown as a technological experiment aboard the Nimbus 3 satellite and successfully demonstrated the feasibility of global data collection through tracking operations with air, sea, and land deployed platforms. The accomplishments of this program provided the design base of the improved Nimbus 4 system

which incorporated features sufficient to enable the world-wide meteorological balloon tracking experiment to be conducted.

A major developmental effort on the Nimbus 4 program involved the design of the BIP shown in Figure 2. The BIP consists of an antenna mounted on a 1.2-m diameter ground plane, a polystyrene housing containing the electronics, and a solar array. The unit is powered by rechargeable batteries and is thermally designed to maintain an internal battery temperature near 0°C during day or night periods of operation. The entire payload weighs 4.5 kg and is suspended 30 m below the balloon. The development of a 4.5-kg BIP represented a 90 percent reduction in gross weight as compared to the platform design requirements of the Nimbus 3 system. This reduction was primarily due to a 6-dB improvement realized in the satellite receiver sensitivity which in turn yielded a corresponding reduction in platform transmitter power requirements (25 to 6.25 W).

The system improvements which led to the lighter self-contained BIP unit required for balloon applications also provided a versatile instrument suitable for other applications. For example, a BIP was reconfigured into an animal collar and utilized to perform the first satellite animal tracking experiment (April 1969). Additional applications involving lightweight buoys are currently under development for the Nimbus 4 mission.

An example of balloon tracking data obtained during the experiment is shown in Figure 3. The trajectories of two balloons flying at the 50-mb level are plotted during five revolutions of the Earth. Movements north and south of the equator, but remaining within  $\pm 10$  deg, were observed on each revolution. On other flights, at both altitudes, the tendency to remain near the equator was likewise observed. This tendency is of interest to experiment meteorologists since it was expected that 10 to 15 percent of the balloons would leave the equatorial region.

A brief example of additional information contained within the data is seen by referring to the wave ridges indicated by the arrows. The ridges indicated are believed to be caused by the same wave as it progressed easterly in opposition to the direction of balloon travel. This is evidenced by the changes in longitude on successive revolutions in the upper trace, beginning with August 30, and by comparison of wave ridges seen on each balloon near the September 16 and 28 time periods. The progressive movement of the wave toward the east is at a rate of approximately 5 m/s

while the balloon speed is approximately 74.4 km/hr (40 knots). A thorough analysis of all data is being performed by Dr. James Angell of NOAA and Dr. Richard Reed of the University of Washington. A paper describing their initial results will be delivered at the spring meeting of the American Geophysical Union in April 1971.

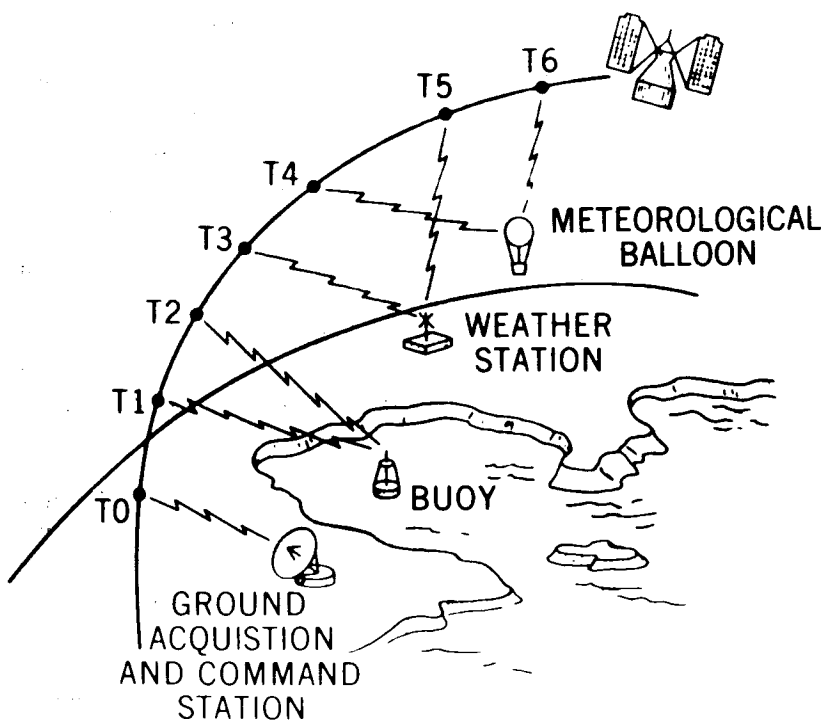


Figure 1—Interrogation, recording, and location system (IRLS).

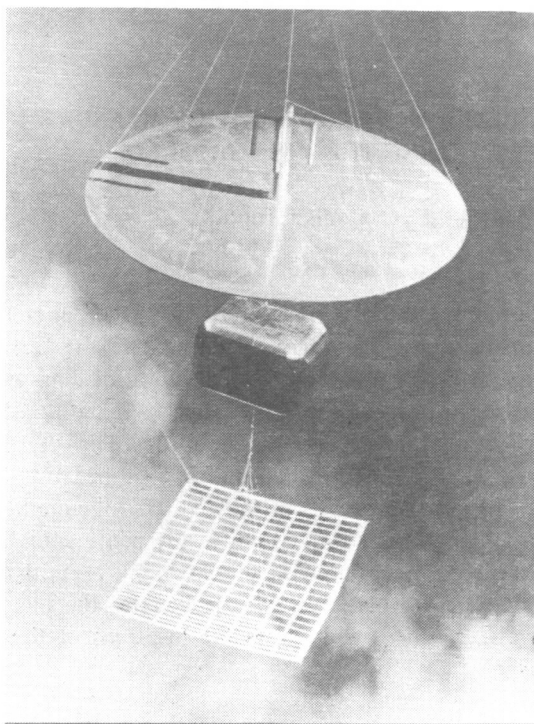


Figure 2—Balloon interrogation package.

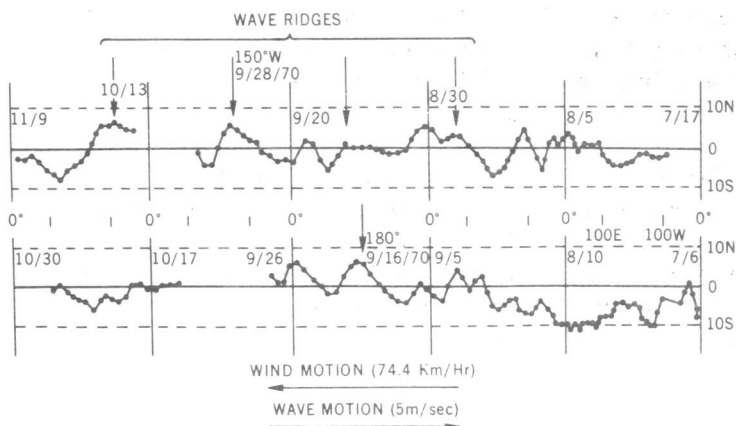


Figure 3—Nimbus 4 IRLS 50-mb balloon trajectories.

## **MILLIMETER WAVE PROPAGATION MEASUREMENTS USING THE ATS 5 SATELLITE\***

**Louis J. Ippolito**

The Applications Technology Satellite (ATS 5) Millimeter Wave Propagation Experiment is the first flight experiment in the GSFC Millimeter Wave Measurements Program for the determination of long- and short-term attenuation statistics of operational millimeter wavelength Earth-space links as a function of defined meteorological conditions. The ATS 5 experiment, launched August 12, 1969, is providing the first propagation data from an orbiting geosynchronous spacecraft in the 15-GHz (downlink) and 32-GHz (uplink) frequency bands. Several stations in the continental United States and Canada have been operating with the downlink transmission from the satellite since late September 1969. Figure 1 states the objectives of the Millimeter Wave Experiment and shows the locations of the participating ground stations.

The spacecraft transmitter is an all solid state phase-modulated unit that provides up to 250 mW of CW power at 15.3 GHz. The 31.65-GHz uplink signal is derived from a frequency stabilized klystron, varactor up-converter and 1000-W traveling wave tube amplifier. A multilevel computer processing program generates propagation statistics for attenuation as a function of rainfall rate, sky temperature, radar backscatter, and other meteorological variables.

The prime NASA station, located in Rosman, North Carolina, can both receive and transmit. The antenna system and radiometer and radar pedestals are shown in Figure 2. Downlink measurements made at Rosman show typical attenuations of 1 to 3 dB in light rains or dense fog, 3 to 7 dB in continuous rains (5 to 50 mm/hr), and a number of fades exceeding 12 dB in heavy thunderstorms. Uplink fades of up to 18 dB in heavy rains have been observed.

---

\*Paper delivered by J. Larry King.

Correlation of measured attenuation with ground measured rainfall rate was low for a single gauge but improved significantly with height averaging of 10 gauges. Correlation of measured attenuation with sky temperature recorded on a small aperture radiometer was very good for most storms. Valid predictions of attenuation from 16-GHz sky temperature measurements were observed for up to 15 dB of measured attenuation.

The uplink to downlink attenuation ratio varied with each precipitation event and often varied during a single storm. The ratio has ranged from 2:1 to 4:1 during heavy precipitation periods. Site diversity measurements at Columbus, Ohio, have demonstrated significant reductions in outage time rates with two stations placed 4 km apart.

The ATS 5 experiment results through the first 14 months of satellite operations are summarized in Table 1. Fifteen organizations with 19 ground stations are presently equipped to operate with the ATS 5 satellite, and experiment operations through June of 1971 are planned. A complete evaluation of propagation effects in the two frequency bands must await the reduction and analysis of the complete weather profile data from all participating stations. From the data reduced to date, however, it appears that both frequency bands exhibit an excellent potential for eventual utilization in reliable high-data-rate Earth-space communications systems.

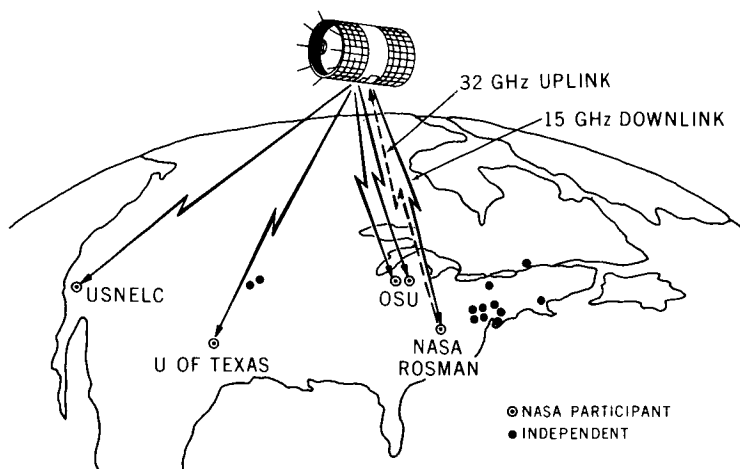


Figure 1—The ATS 5-millimeter wave experiment.



Figure 2—NASA Rosman, North Carolina, station.

Table 1—ATS 5 millimeter wave experiment summary  
(Oct. 1, 1969 – Dec. 31, 1970).

#### YEARLY OUTAGE TIME, ROSMAN STATION

- 15.3 GHz ATTENUATION EXCEEDED 15db FOR 1.7 HRS (0.02%)
- 31.65 GHz ATTENUATION EXCEEDED 18db FOR 13 HRS (0.15%)

#### BANDWIDTH COHERENCE

- NO MEASURABLE DECORRELATION ON EITHER LINK TO  $\pm 50$ MHz

#### RAINFALL RATE CORRELATIONS (DOWNLINK)

- LOW FOR SINGLE GAUGE
- SIGNIFICANT IMPROVEMENT WITH HEIGHT AVERAGING

#### SMALL APERTURE SKY TEMPERATURE CORRELATIONS (DOWNLINK)

- VALID PREDICTIONS TO 15db OF ATTENUATION
- MEASURED ATTENUATION SLIGHTLY LOWER THAN PREDICTED

#### INTEGRATED $K_U$ BACKSCATTER CORRELATION (DOWNLINK)

- LOW, RESPONSE VARIES WITH EACH STORM

#### UPLINK — DOWNLINK COMPARISON

- ATTENUATION RATIO STORM & TIME VARIABLE
- 2:1 TO 4:1 RANGE

#### SITE DIVERSITY

- TWO STATION (3 KM SEPARATION) IMPROVEMENT FACTOR OF 100

## GLANCING INCIDENCE TELESCOPES FOR SPACE ASTRONOMY

John D. Mangus

In the past two years, I have reported on our efforts to develop glancing incidence telescopes for space astronomy applications. The geometries of these telescopes are shown in Figure 1. The Type I telescope, or X-ray telescope, is used in the spectral region below 100 Å. The Type II telescope is employed in the spectral region from 100 Å to approximately 900 Å. Above 900 Å, telescope configurations such as the Cassegrain telescope (Figure 1) are used to collect spatial and spectral information.

In 1968, I reported a technique to be used in optimizing the image quality of Type I telescopes, and in 1969, I reported a technique for use in the design and optimization of image quality of the Type II telescope. At that time, I also reported that two problems were to be intensively investigated in 1970:

- (1) Increasing the collecting area of glancing incidence telescopes.
- (2) Imaging anomalies noted in the testing of Type II telescopes.

This year, I will report on the first of these problems, which deals with the essential features of two techniques which permit the design of glancing telescopes of increased collecting area (optical throughput) and which simultaneously preserve optimized image quality. The paper by Mrs. Innes will treat the problem of imaging anomalies by glancing incidence telescopes.

Before I proceed, note that in Figure 1, the focal length of glancing telescopes is determined by the intersections of the incoming rays with those rays projected back from the focus of the telescope. The locus of points generated by these intersections is called the principal surface, and as such, determines the effective focal length of the telescope.

Figure 2 illustrates nested geometries for X-ray and extreme ultraviolet (EUV) telescopes. Note that it is imperative that each telescope in the nested array generate a singular principal surface. If this were not the case, then the telescopes would behave as if they possessed several different focal lengths. In the case of the X-ray telescope, a candidate configuration was investigated, and it was discovered that this telescope did not exhibit a singular effective focal length. The design parameters were perturbed so that the nested array generated a singular principal surface. Unfortunately, once this condition is met, the curvature of field of each telescope is significantly different. Classical field curvature is determined by the eccentricities of the image surfaces and therefore does not lend itself to modifications once the geometry has been selected. However, it was discovered that if the field curvature of the outer telescope is selected as a standard, the focus of each of the inner telescopes could be made coplanar by a slight decrease in the collecting area (diameter) of each of the inner telescopes.

The nested EUV telescope exhibited essentially the same problem, namely, that once the nested telescopes are forced to generate a singular surface, the field curvatures exhibited by each of these telescopes do not match. However, in the case of the EUV telescope, one may slightly perturb the maximum glancing angle without a severe loss in reflectance. In the case studied, it also was found that by a change in the maximum slope angle of the inner telescope of one degree, the field curvatures can be made to coincide. The image quality of each of the two candidate telescopes studied is shown in Figure 3. In Figure 3(a), the image quality is formed by five concentric X-ray telescopes with a collecting area of approximately  $900 \text{ cm}^2$ . In Figure 3(b), the image quality is shown for a nested EUV telescope which consists of two concentric telescopes. The effective focal length of the telescope is one meter, and the collecting area is  $45 \text{ cm}^2$ .

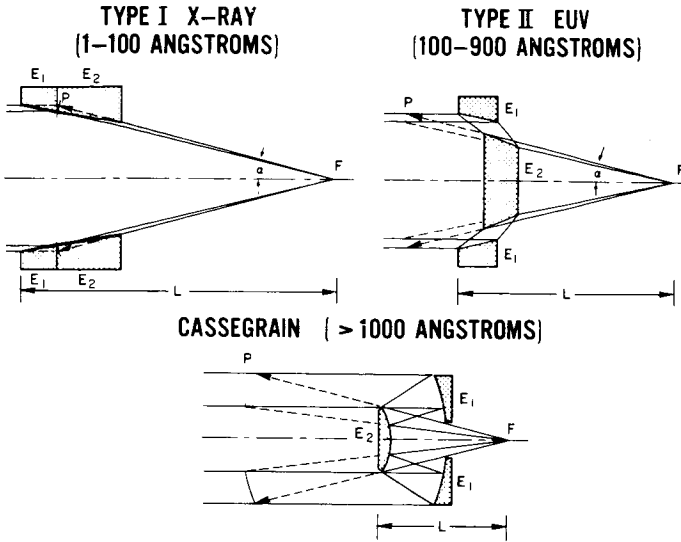


Figure 1—Types of glancing incidence telescopes for space astronomy applications.

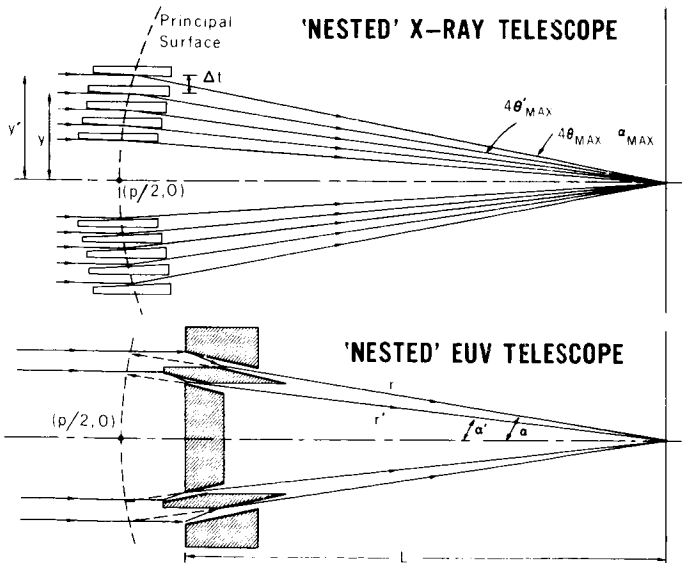
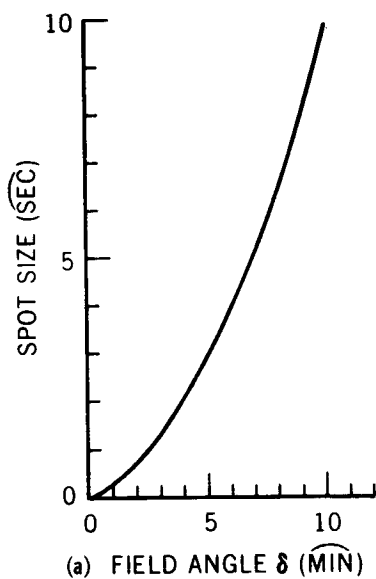


Figure 2—Telescope geometries.

## NESTED X-RAY TELESCOPE



## NESTED EUV TELESCOPE

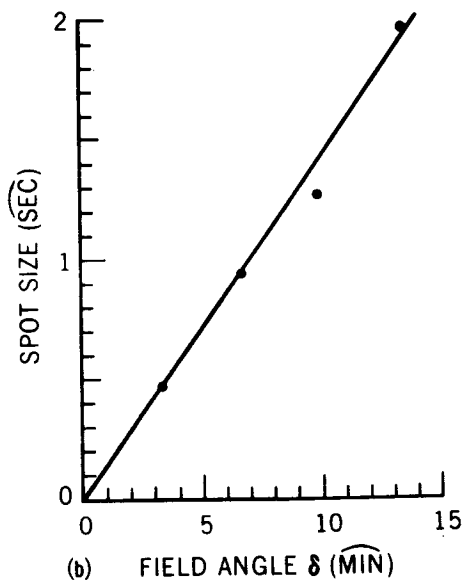


Figure 3--Image quality.

## A COMPUTER PROGRAM TO EVALUATE OPTICAL SYSTEMS

Daphne Innes

It is customary to use geometrical optics in the design of optical instrumentation. Usually these methods predict performance which is in reasonably good agreement with that achieved when the instrument is finally manufactured. However, in the case of the glancing incidence systems for use in the X-ray and extreme ultraviolet (EUV) region of the spectrum, this did not prove to be the case. Figure 1 shows the results of the geometrical analysis for a 25.4 cm X-ray telescope at a field angle of 20 minutes of arc. The large area represents the size of the spot based upon geometrical optics.

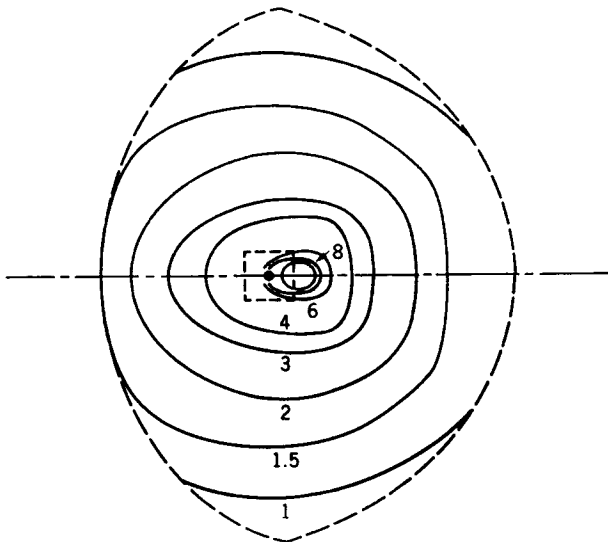
The black spot in the center represents the size of the Airy disc at 5000 Å for a diffraction limited system. Hence, even in the visible region, a performance many times poorer than the theoretical limit is predicted. However, when the telescope was constructed and tested in the visible region, it was found that the entire observable image fitted inside the dotted box. In an attempt to account for this discrepancy, we turned to a wave optical analysis.

Since very large computers were at our disposal, we decided to write a computer program based upon very exact general principles. In short, we decided to solve Maxwell's equations numerically. The object is regarded as a point source of electromagnetic radiation, and the optical surfaces are treated as the boundary conditions in the solution of the electromagnetic wave propagation equations. The electric field distribution is then evaluated in the region of the image, and from this, the intensity distribution is inferred.

Figure 2 shows the results of the wave analysis and a photograph taken through the actual telescope. Note the excellent agreement of results. Since the program was formulated in such general fashion, it was found to be readily adaptable to the analysis of a large class of optical systems. Figure 3 shows the results applied to a 1-meter diameter, f4 parabola at 0.1 deg

off-axis. In addition, the program is being used in the evaluation of the large space telescopes and the design of an EUV interferometer.

In conclusion, we may state that although we will still use geometrical optics in the design of optical systems in the future, we now have, in addition, a tool for the accurate evaluation of the performance of optical systems prior to their construction.



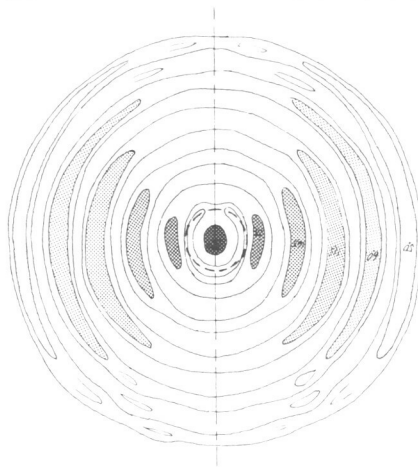
COMPARED WITH ACTUAL IMAGE (SMALL SQ.)  
FOR 20 MIN. OFF-AXIS SOURCE.

GEOMETRIC IMAGE DIA.-200 MICRON,  
DIFFRACTION LIMITED AIRY DISK-5 MICRONS.

Figure 1—X-ray telescope geometric optical image.

WAVE OPTICAL IMAGE

FOR 20 MINUTES OFF-AXIS SOURCE



ACTUAL IMAGE

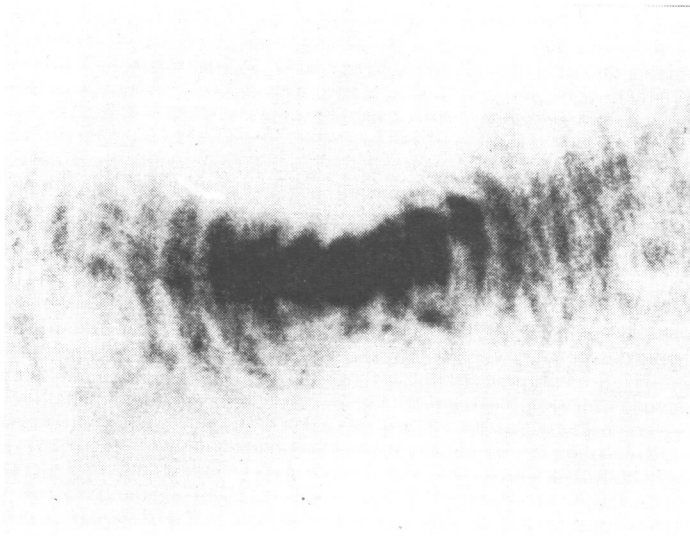


Figure 2—Results of wave analysis and actual photograph.

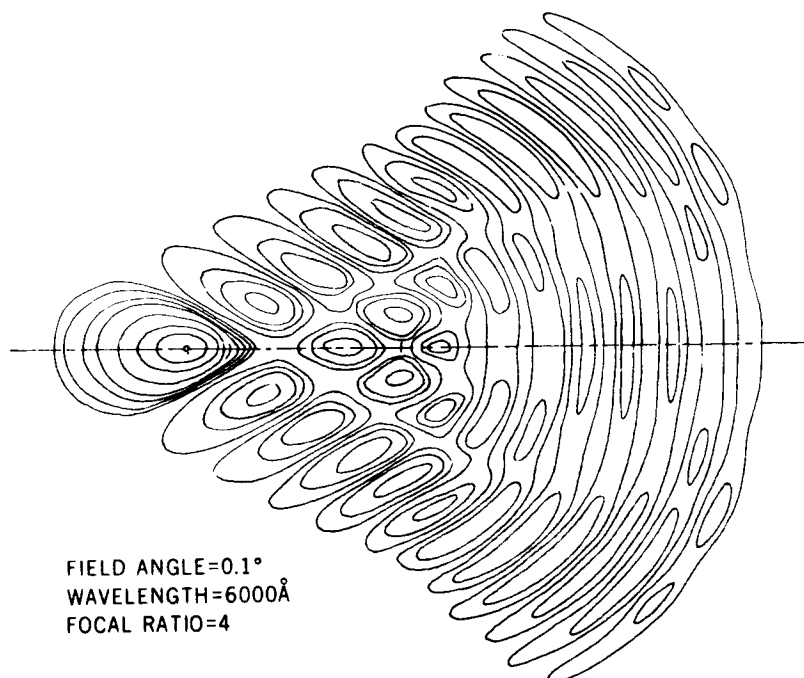


Figure 3—Wave aberrations for 1-m diameter parabola.

## MULTISPECTRAL IMAGE DISSECTOR CAMERA SYSTEM

**Bernard L. Johnson**

The ERTS spacecraft will provide multispectral images via two sensors, the Return Beam Vidicon Camera (RBV) system and the Multispectral Scanner (MSS) system. The RBV system requires three individual cameras to obtain data in three spectral channels. Unless the cameras are perfectly bore-sighted and completely identical in all respects, misregistration between images will result which can only be corrected by elaborate ground processing techniques. The MSS on the other hand requires a complex oscillating scan mirror and six detectors in each of four spectral channels to obtain adequate signal to noise ratios. Because of these disadvantages, an effort was made to develop a sensor system which would provide registered high-resolution multispectral images from a single sensor with no mechanical moving parts.

Figure 1 shows how the Image Dissector Camera (IDC) system operates. An Earth scene 100 nautical miles wide is imaged through a single lens onto a photocathode surface containing three spectral filters, thereby producing three separate spectral signatures on the photocathode surface. An electron image is formed and is accelerated, focused, and electromagnetically deflected across an image plane which contains three sampling apertures, behind which are located three electron multipliers.

The IDC system used electromagnetic deflection for cross-track scanning and spacecraft orbit motion for along-track scanning, thus eliminating the need for a mechanical scanning mirror. Because a single lens and electrooptical system are used, registration is assured with simple "X" and "Y" positioning of the write beams in the ground processing equipment.

Table 1 shows a comparison of data obtained with an engineering model and lens system in the lab and with the RBV system. As noted, the IDC has achieved 3400 TVL resolution as compared to 4000 for the RBV. This small difference will likely vanish in final picture processing because of

the ease of registration with the image dissector. A 3 to 8 dB improvement in S/N with the RBV system is noted. This is not as great a difference as it first seems. In the RBV system, the signal output is generated from the returned portion of the electron beam scanning the photocathode; hence, as signal input goes down, return beam current goes up, resulting in increased noise. This causes S/N to decrease at a faster rate than is normally associated with reduction in signal level. In the IDC, the exact opposite occurs. As the signal input goes down, so does the photomultiplier current, reducing the noise level, and hence, the S/N does not decrease as fast as that dictated by normal signal level reduction. This results in picture quality that does not suffer as much from the lower S/N seen in the IDC. Excellent quality is seen in pictures taken with values of S/N typical of those which would be achieved with an orbital camera system. It will be an important experiment to make pictures of identical scenes with both the RBV system and the IDC and allow potential users to evaluate the relative merits of the resulting imagery.

In conclusion, the IDC system is lighter in weight, smaller in volume, simpler in electronics and mechanics, simpler in ground processing equipment required, and, most importantly, considerably cheaper than existing multispectral image systems intended for use in the ERTS mission.

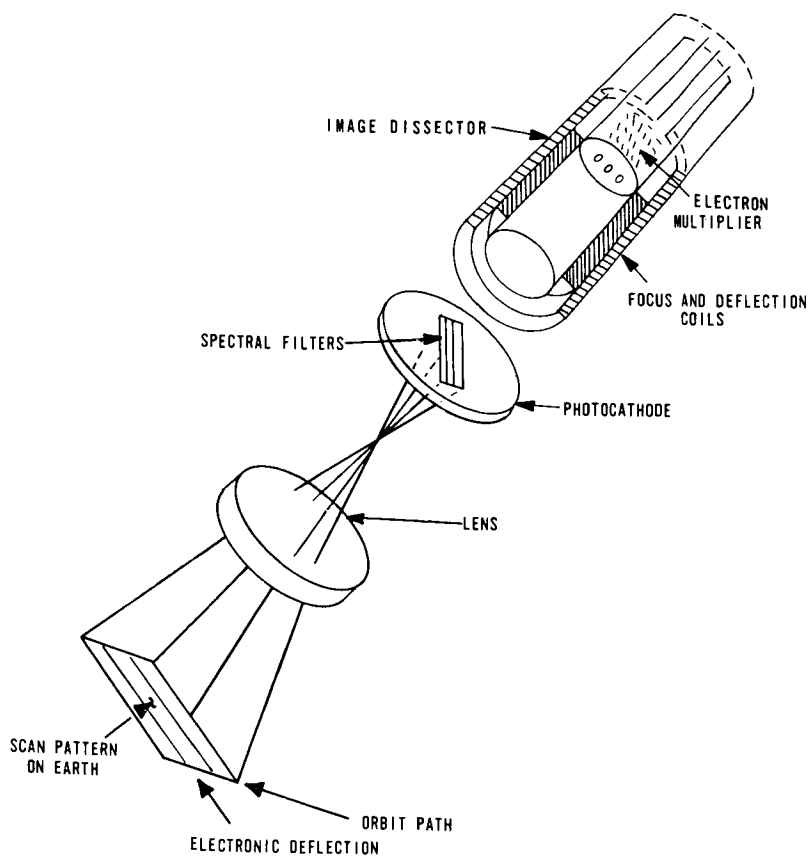


Figure 1—Schematic diagram of the IDC system.

Table 1 —Performance of the IDC and RBV systems.

System	Tube Resolution (TVL)	In-Laboratory System* (TVL)	S/N Ratio (dB)		
			Channel 1 (475-575 mm)	Channel 2 (580-680 mm)	Channel 3 (690-830 mm)
IDC	3400 @ 25% mod.	3400 @ 5% mod.	25	23.8	22
RBV	4500	4000	33	33	25

\* Lens and camera with scene having 40% reflectance and contrast ratio 6:3 to 1.

## PRECISION DIGITAL SOLAR ASPECT SENSOR

H. P. Scherer

Digital solar aspect sensors have been used successfully in many flight programs. These sensors give a digital output that is proportional to sun angle. Light passing through a slit forms an image of the slit on a binary-code pattern reticle that is separated from the slit plane by a fixed distance. Silicon photocells behind each column of the code pattern are illuminated by the light coming through the slit to give a digital output which is a function of sun angle. The accuracy achieved by this system is limited to about  $\frac{1}{2}$  degree, because of the angle subtended by the Sun.

Figure 1 shows a precision digital solar aspect sensor which has been developed with a resolution of  $1/256$  degree, or approximately 14 arc-seconds. The overall accuracy is 1 arc-minute. A binary coded reticle similar in principle to those used on  $\frac{1}{2}$ -degree systems is used to generate the most significant bits. If a gray code were used, as in the  $\frac{1}{2}$ -degree systems, all bit transitions would have to be made to an accuracy of better than 1 arc-minute. The precision sensor uses a natural binary code reticle, with V-brush logic to eliminate the ambiguity inherent in natural binary transitions. The reticle configuration is shown in Figure 2.

An interpolation technique is used to generate the fine angle measurements. Four columns are used, each having a 2-degree spacing but successively displaced by  $\frac{1}{2}$ -degree increments. The fine angle signal processing is shown in Figure 3. As the slit image scans across the reticle, four sine waves are generated with a period of 2 degrees but displaced 90 degrees in phase from each other. The sinusoidal waveform results from the interaction of the slit and the circular image of the Sun.

The outputs from the four columns are chopped by four quadrature square waves derived from a chain of flip-flops counting down from a fixed-frequency oscillator. These outputs are summed and passed through a bandpass filter to produce a sine wave whose phase is proportional to the sun angle. This phase angle is measured by counting the number of pulses at

the oscillator frequency that occur between the zero crossings of the phase reference and the sine wave. Upon receipt of a command signal, the number counted is transferred into a buffer storage register and held until the next command is received.

The sensor being developed has a single sensor head with a total angular field of view of 64 degrees in each of two orthogonal axes. Outputs of a number of sensor heads may be combined to extend the field-of-view capability. Complete spherical coverage with an accuracy of 1 arc-minute can be achieved in this manner. The data output consists of a Sun-presence signal from the illuminated head and a two-axis error signal from that head. Unlike analog sensors, the digital sensor is not susceptible to errors caused by other light sources such as the illuminated Earth. The detector output from these light sources is below the solar threshold level.

The electronic and mechanical design of this sensor has been completed, and two flight units are being fabricated. One of these units will be flown as an experiment aboard OAO 4. A simpler one-axis form of this sensor can be used to determine the attitude of a spinning spacecraft. A single slit command reticle is used to determine when the sensor sweeps past the Sun and to trigger a readout of the sun angle binary output in the sensitive axis.

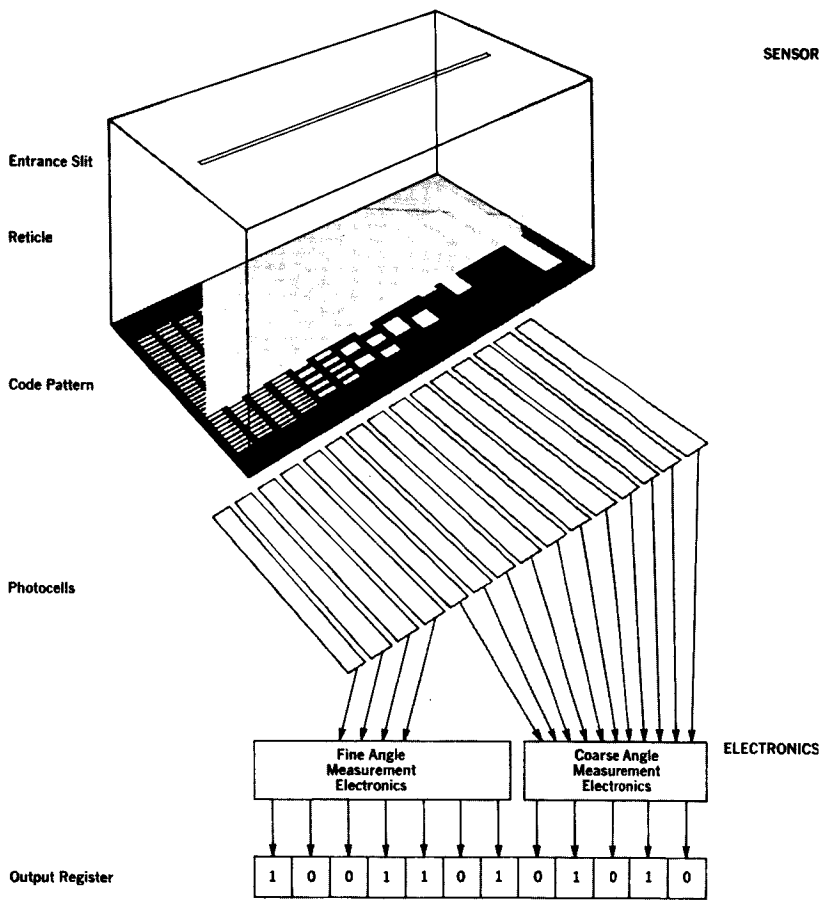


Figure 1—A precision digital solar aspect sensor.

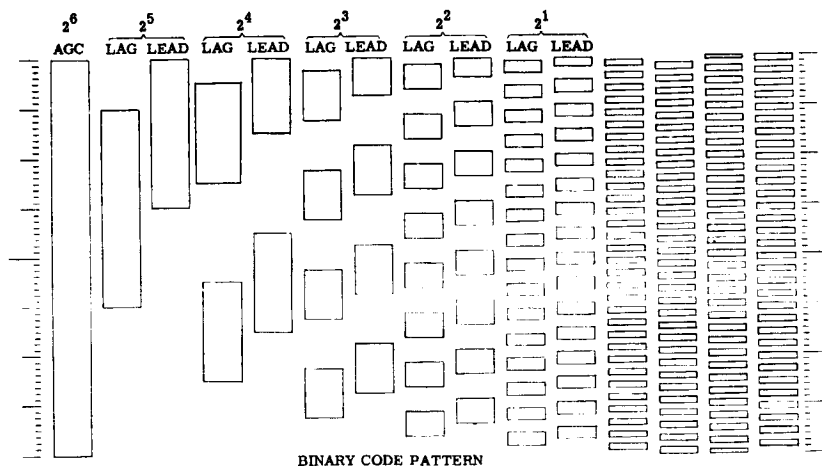


Figure 2—Reticle configuration.

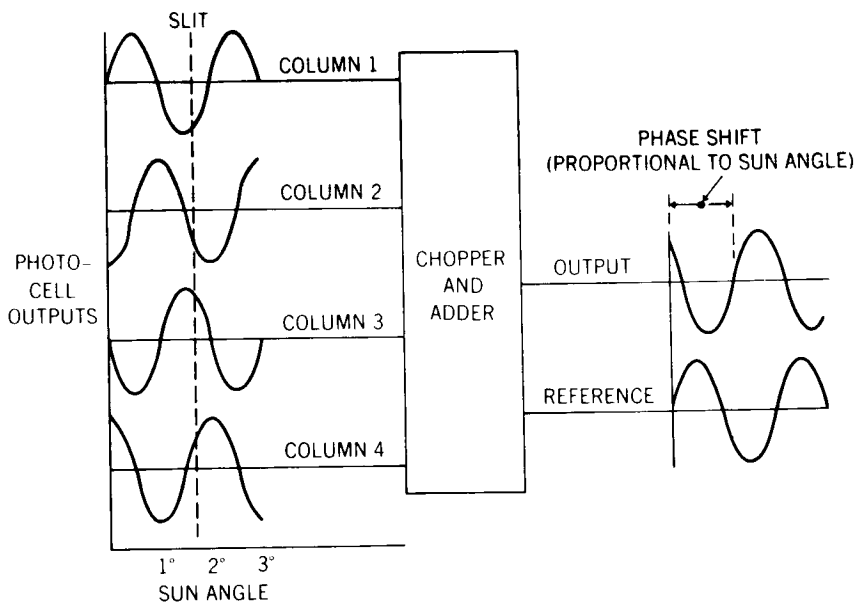


Figure 3—Precision digital solar aspect sensor interpolation technique.

## **AN ADAPTIVE NARROW BAND FREQUENCY MODULATION VOICE COMMUNICATION SYSTEM**

**Sheldon Wishna**

A narrow band frequency modulation (NBFM) communication system which provides for the reception of good quality voice at low carrier-to-noise ratios has been built for the position location and aircraft communication equipment experiment of the ATSF program. The high level of performance of this system is obtained by designing a limiter and phase-lock loop combination as a demodulator so that the bandwidth of the phase-lock loop decreases as the carrier level decreases.

This adaptive feature provides for the improvement in voice reception in two ways. First, by reducing, at low carrier-to-noise levels, the demodulation closed-loop bandwidth, the detected noise for the remaining low frequency voice spectrum is decreased, which in effect increases the remaining voice spectrum signal-to-noise output. The masking effect of the noise makes the intelligibility contribution of the high voice frequencies under high noise conditions negligible so that it is more advantageous to low-pass filter the voice spectrum and thus improve the signal-to-noise ratio of the lower voice spectrum.

Second, reduction of the phase-lock loop bandwidth at low carrier-to-noise levels extends the onset and reduces the rate of degradation caused by demodulation thresholding, which is an operating point where a large degradation of the output signal-to-noise ratio occurs for a small reduction in the input carrier-to-noise ratio.

Figure 1 is a block diagram of the NBFM demodulator as designed for use with ATSF. Another unit has been built and flight-tested as part of the European Space Research Organization Balloon/Aircraft tests conducted last summer. As is shown in the block diagram, the demodulator consists essentially of the limiter and the phase-lock loop combination.

Figure 2 illustrates the adaptive properties of the demodulator. It is seen that, as the input carrier level decreases, the demodulator bandwidth decreases. For example, for an input carrier-to-noise ratio of 49 dB-Hz, the demodulator bandwidth is approximately 4000 Hz; however, at an input carrier-to-noise ratio of 41 dB-Hz, the demodulator bandwidth has decreased to 2100 Hz. This provides a nearly two-to-one bandwidth reduction.

Figure 3 is a plot of the output voice articulation index as a function of the input carrier-to-noise ratio for a laboratory-built demodulator. Articulation index is a measure of voice intelligibility with 95 percent sentence intelligibility occurring at an articulation index of 0.4. The extreme linearity of the NBFM curve is very evident. A calculated plot of a conventional NBFM voice communication system having similar RF and voice processing characteristics is shown for comparison.

One should note that 95-percent sentence intelligibility is obtainable at about 41 dB-Hz. Because of the small deviation employed, only approximately 8 kHz of the RF spectrum is required. The adaptive NBFM system provides, at low carrier-to-noise levels, an improvement in response of approximately 4 dB over that obtained from a conventional NBFM system.

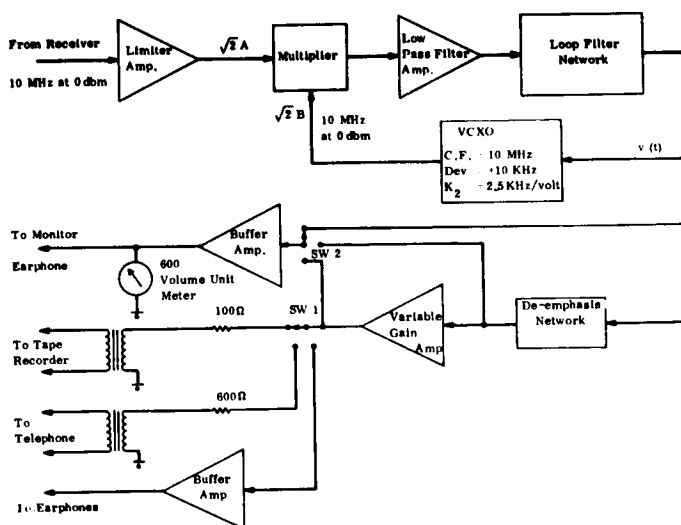


Figure 1—Demodulator block diagram.

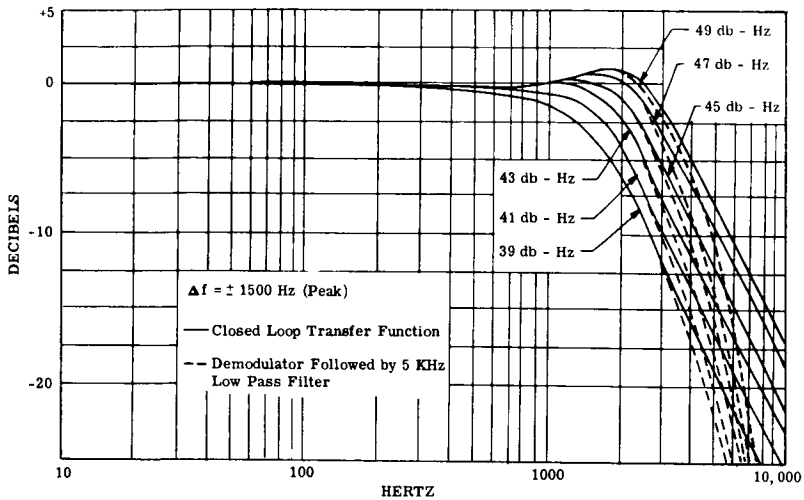


Figure 2--Closed-loop response of phase-lock loop versus carrier-to-noise spectral density.

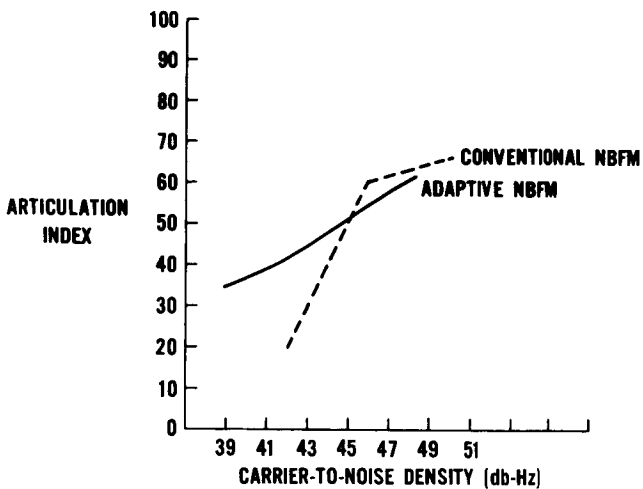


Figure 3--Articulation index versus carrier-to-noise density (FM, 3-kHz voice truncation, clipping such that peak-to-rms ratio is 6 dB, pre-emphasis using 6 dB/octave, 10-kHz RF bandwidth).

## COMPUTER-AIDED CO<sub>2</sub>-LASER CAVITY-LENGTH SELECTION FOR REDUCED LINE COMPETITION\*

G. Schiffner

Carbon-dioxide lasers are attractive for space communications systems because they have many advantages (high efficiency, wavelength near 10  $\mu\text{m}$  where the atmosphere has a window, and good frequency stability). These properties allow the building of heterodyne receivers as part of communications systems which come close to the theoretical sensitivity limit.

Figure 1 shows the absorption spectrum of CO<sub>2</sub> gas in the 10- $\mu\text{m}$  and 9- $\mu\text{m}$  regions. In the case of a CO<sub>2</sub> laser, the gain shows a similar behavior. The strongest laser line is P(20) of the 10- $\mu\text{m}$  band. Because so many lines can oscillate, competition effects occur, and it is often difficult to obtain oscillation at the desired lines. For example, in heterodyne communications systems, the transmitter and the L.O. must operate at the same line, and the L.O. must have a sufficiently large tuning range. This paper shows how competition effects can be reduced by selection of an appropriate cavity length.

The upper portion of Figure 2 shows a laser consisting of a laser tube which contains the active medium and an optical resonator made of two spherical mirrors. One mirror can be moved by a piezoelectric transducer (PZT) element to tune the resonator. The resonator has many resonances (middle portion of Figure 2) with a frequency interval of  $c/2d$  ( $d$  is the mirror separation distance). If one resonance coincides with one line of the active medium (three lines are plotted), then oscillations start. When the resonator is tuned, the cavity resonances are shifted, and another line starts to oscillate. In the lower section of Figure 2, a typical output power profile of a CO<sub>2</sub> laser is shown as a function of the cavity length (or PZT voltage).

---

\*The research was accomplished while the author held a National Research Council Postdoctoral Resident Research Associateship supported by NASA-Goddard Space Flight Center. The author is also with Institut für Hochfrequenztechnik, Technische Hochschule Wien, Vienna, Austria.

Several complete and incomplete line tops can be seen. The lines can be identified by means of a monochromator. The sequence and distribution of line centers over a half-wavelength tuning interval repeats nearly unchanged within the next half-wavelength tuning interval. However, a change of the cavity length on the order of 0.1 mm or more may completely alter the sequence and distribution of line centers. This property is more or less unique for each laser and is called its "signature".

During this study we first attempted to predict the signature of CO<sub>2</sub> lasers. It was found that this requires very accurate data on the laser wavelengths (accuracy on the order of 10 MHz). The results of recent absolute frequency measurements of CO<sub>2</sub> lines were utilized, and a list of accurate frequencies was calculated that fulfilled the requirements.

A computer program which can be used to predict the signature was written. Several comparisons were made, and in each case close agreement was found. Figure 3 shows signatures taken with decreasing (top) and increasing (bottom) PZT voltage. Unfortunately, the PZT elements are not perfectly linear and show hysteresis effects. The portion between the two P(26) lines seems to be fairly linear. Figure 3 also contains for this portion the predicted positions of the line centers, which fit quite well.

Another computer program was written which searches through large ranges of cavity length and prints lists of regions where a particular line is well separated from adjacent lines in the signature. Lasers designed according to this list will have an undisturbed tuning profile for one or more lines. These results make it possible to design L.O.'s for heterodyne systems without a grating within the resonator. (Until now, gratings had to be used in order to achieve a satisfactory tuning range.) This results in an increased efficiency for the L.O. and a power saving of several watts.

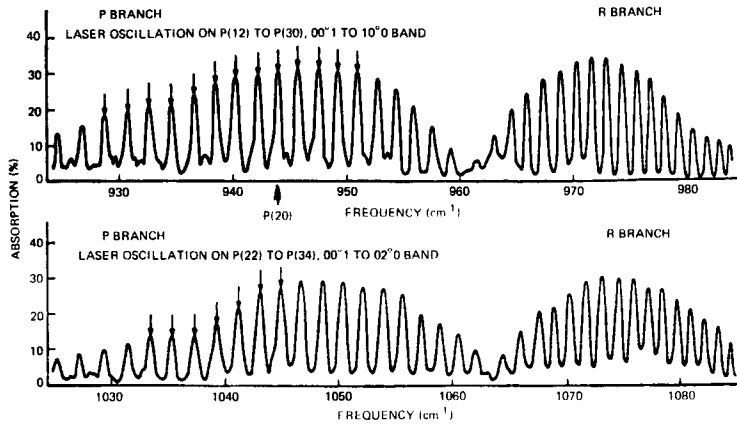


Figure 1—Carbon-dioxide absorption spectrum for the 10-μm or 28.8-THz band (top) and for the 9-μm or 31.9-THz band (bottom). (After Barker and Adel, *Phys. Rev.* 44:185, 1933, and Patel, *Phys. Rev.* 136A:1187, 1964.)

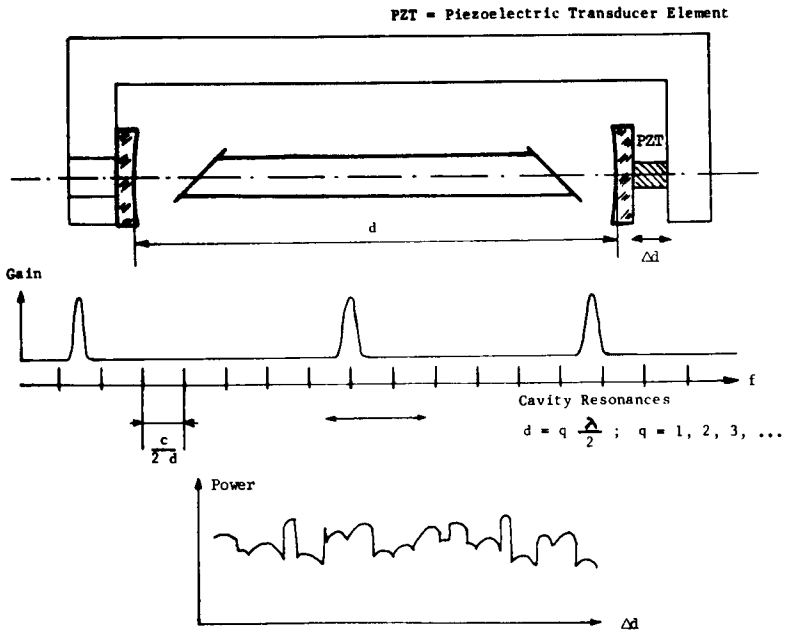


Figure 2—Carbon-dioxide laser and characteristics.

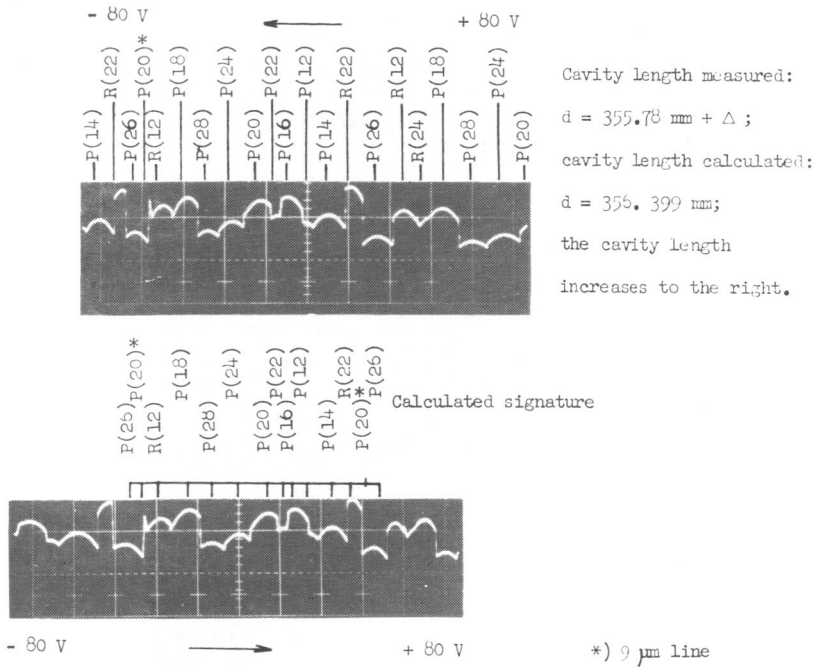


Figure 3—Comparison of measured and predicted signature.

## **RESULTS OF FM-TV THRESHOLD REDUCTION INVESTIGATION FOR THE ATS F TRUST EXPERIMENT**

**James P. Brown**

In commercial FM-TV transmission, threshold effects are seldom a problem since the received carrier-to-noise ratio is usually large. For low cost community TV reception via satellite, however, this is not necessarily the case. For this reason, an investigation of threshold effects in FM-TV was initiated, primarily to determine if any simple, low cost techniques were available which can reduce the subjective video threshold. The first step was to examine the work of Rice and determine the fundamental causes and effects of threshold phenomena. From this study, it was determined that the threshold would be caused by voltage spikes appearing at the demodulator output as the input carrier-to-noise ratio is decreased. It was thought that the observed effects due to this phenomena would be white dots in the dark picture areas and black dots in the white areas. Actual observations, however, revealed that as the carrier-to-noise ratio was decreased, the first observable threshold effect was frequently white streaks which were noticed in the dark picture areas. No corresponding black streaks in white picture areas were observed, and the expected black and white dots did not occur until substantially lower carrier-to-noise ratios were reached.

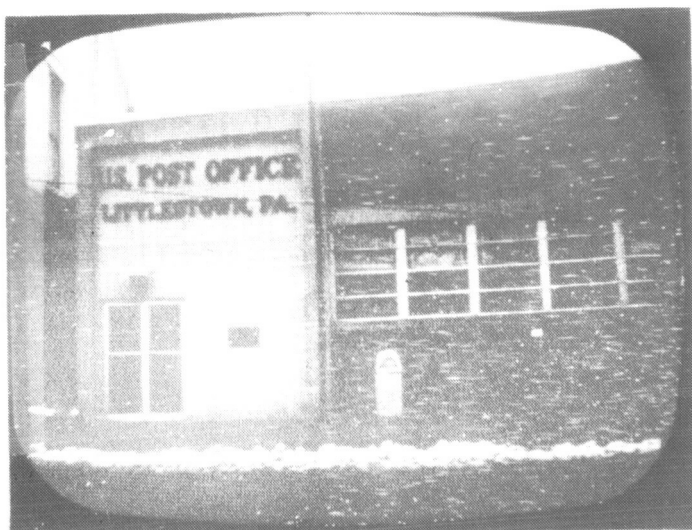
A reexamination of the problem led to the following hypothesis: Since the probability of occurrence of a spike depends not only on the input carrier-to-noise ratio but also on the deviation of the carrier from the center frequency, and since the video horizontal sync pulses represent the peak frequency deviation in one direction, it is reasonable to assume that many spikes will occur during the horizontal retrace period. These would normally appear as white dots, but the fast horizontal retrace smears them, and they appear as white streaks which are visible only in the dark picture areas. Examination of the video waveforms revealed that this was indeed the case.

Two methods have been examined to eliminate these effects. One method is the use of standard video pre-emphasis. The pre-emphasis

networks attenuate the low frequency portion of the baseband video signal by about 10 dB, thus reducing the deviation of the carrier due to the low frequency components of the video signal. Since the horizontal sync pulses are primarily composed of low frequency components, the deviation of the carrier due to the sync pulses is reduced, thereby reducing the probability of threshold spike occurrence. While pre-emphasis is a well known, inexpensive technique, there are cases for which one does not wish to use it. Obviously, if a standard FM signal is being received, one cannot utilize a de-emphasis network at the receiver without requiring that a pre-emphasis network be employed at the transmitter. For this reason, an alternate technique, horizontal retrace blanking, was developed.

Normal TV sets are designed for use with the standard AM-TV transmissions and rely on the detected video waveform to blank the picture during horizontal retrace. In an AM system, no threshold spikes occur during the sync pulse, and horizontal retrace blanking is unnecessary. For an FM system, this is not the case. However, adding a circuit to blank the picture tube during the retrace period will solve the problem. A simple one-shot multivibrator, triggered by the start of horizontal retrace and providing a blanking pulse to the picture tube, is a simple and inexpensive means of eliminating these threshold noise streaks.

If one defines the subjective threshold as that carrier-to-noise ratio at which threshold effects just become noticeable, then horizontal retrace blanking provides about a 3 dB decrease in the subjective threshold. Based on this, one can conclude that active horizontal retrace blanking does provide a simple technique for reducing the subjective threshold in standard FM-TV (see Figure 1).



WITHOUT BLANKING



WITH BLANKING

Figure 1—Demonstration of the effect of active horizontal retrace blanking.  
Both pictures are at the same carrier-to-noise ratio.

## RADIATION DAMAGE EFFECTS ON SOLID STATE DETECTORS

James H. Trainor

The solid state detectors I will discuss are totally depleted silicon diodes used as nuclear particle detectors in investigations of galactic and solar cosmic radiation and also trapped radiation. The convenient size of these detectors, their relatively low bias voltage requirements, their extremely good energy resolution, and their small dead time effects have often led to their selection over competitive detector systems (witness the Pioneer F and G and Helios A and B experiment selections).

To the list of their advantages, one can now add an extremely long lifetime as a typical characteristic. In the mid 1960's, this statement could not have been made because there was a history of these detectors failing, becoming noisy, or developing other problems. In fact, we now understand that most of these detectors behaved normally, expiring just about on schedule because of radiation damage effects. Those effects were not well understood then because much of the information existing at that time came from studies of irradiations in nuclear reactors or in accelerators where one had to contend with multiple nuclear radiations: charged particles and neutrons, gamma rays, and X-rays with complicated spectra. Usually, results were presented as a critical parameter versus absorbed dose in rads. We now know that this is not a good way to analyze the problem, which is a fairly complicated one. The important effects are dependent on the type and energy of the particle, and the results are best understood in terms of the parameter of interest versus the integrated flux, or fluence, as it is called.

For several years, we have been involved in a systematic study of these radiation effects, and, more recently, chemical effects also. Normally, one is interested in the detector's noise, leakage current, capacitance, and energy resolution in the measurement of the particles emitted from a convenient radiation source, such as  $\text{Am}^{241}$ . Work on electron and proton irradiation of surface barrier detectors with thicknesses up to 1 mm has been completed, and indepth work on lithium-drifted silicon devices with thicknesses of several millimeters is beginning.

Figure 1 is an example of our early results and shows a quite unexpected result. In the figure, the detector noise is plotted versus the integrated flux of protons incident on a surface barrier detector. Four curves are shown: two for irradiation by 200-keV and 800-keV protons through the front, gold surface and two for the same particles through the rear, aluminum surface. All other conditions were identical in each case. The noise produced by the damage effects of low energy protons incident on the rear, aluminum contact of the detectors is lower by a factor of  $10^3$  to  $10^4$  than the effect of protons incident on the front, gold contact. For the typical steep spectrum we are dealing with in space, this effect can markedly extend the lifetime of a detector if the rear contact is preferentially exposed.

Figure 2 is taken from recent work which will be published in the February issue of *IEEE Transactions on Nuclear Science*. The device's capacitance is plotted versus the fluence of electrons. The upper set of curves is for a 50-V bias on the device; the lower curves are for a full bias of 150 V. The effect of electron energy is clearly visible. Similar effects are present for noise and leakage current.

Figure 3 shows a somewhat more subtle effect. What one is really interested in measuring with these detectors is the energy deposited in a given detector or series of detectors (and really measuring this deposited energy with good resolution). One can get a good feeling for this by looking at pulse height spectra. The number of events recorded is plotted on the ordinate and the energy deposited in the detector is plotted on the abscissa. These spectra are taken from a detector irradiated by 400-keV electrons.

Spectrum (a) is a normal spectrum showing the expected alpha particle distribution from  $\text{Am}^{241}$  and the distribution from a good pulser. The width of the pulser peak is a measure of the resolution or noise of the detector. Spectrum (b) shows the accumulated effect of an irradiation of  $3 \times 10^{14}$  electron/cm<sup>2</sup>. There is very little broadening of the pulser peak, but there are prominent changes in the response to the alpha particles. Some of the charge liberated in the detector is not being collected.

Spectra (c) and (d) continue the rapidly deteriorating picture. Although the noise, resolution, capacitance, and leakage current have changed little, this detector is useless for spectral analysis after irradiation exceeding  $10^{14}$  electron/cm<sup>2</sup>. The loss of charge collection efficiency is due primarily to the

trapping of charge carriers on defects, which leads to smaller pulse heights and longer rise times.

Although a complicated set of processes is going on here, two things are clear: (1) there is a great advantage in using the aluminum contact as the detection front surface and (2) detector biases should be as large as possible (i.e., in the range of 100 to 200 V/mm) to minimize the loss of charge collection efficiency and to maintain the depletion depth.

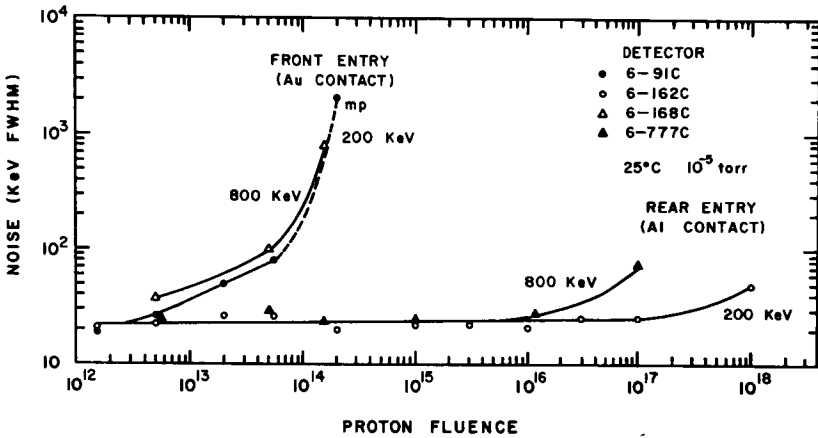


Figure 1

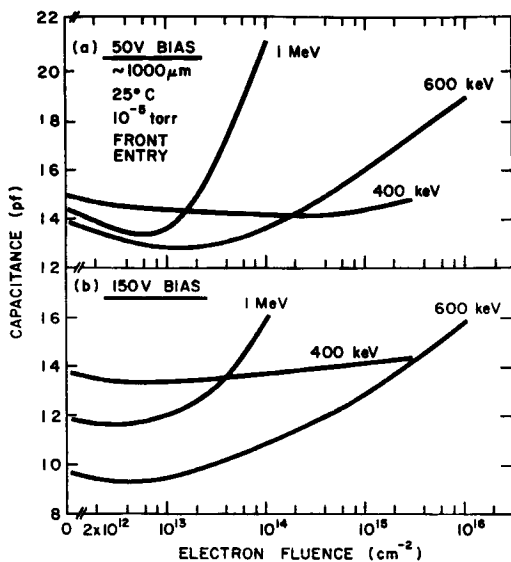


Figure 2

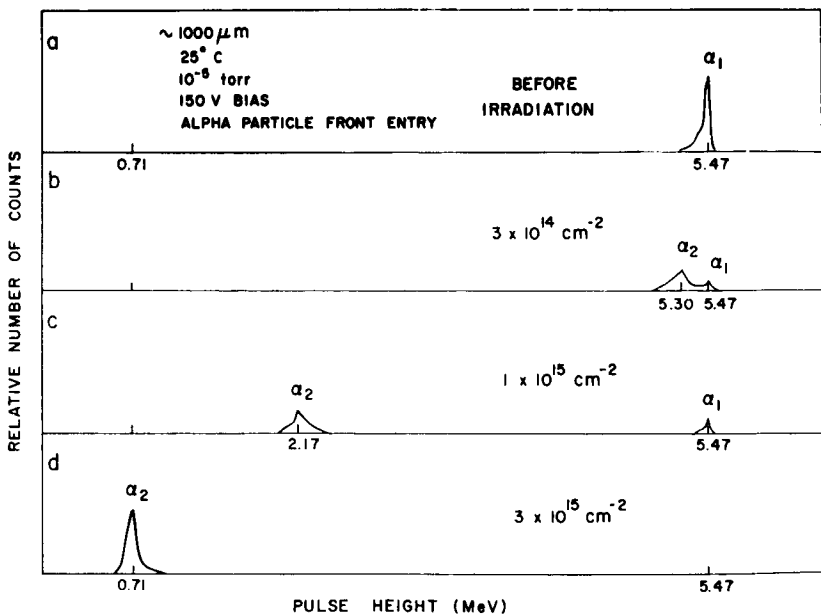


Figure 3

## REVISED STANDARDS FOR THE SOLAR CONSTANT AND THE SOLAR SPECTRUM

M. P. Thekaekara

This paper presents the values of the solar constant and solar spectrum which are proposed as revised standards for science and technology. The proposal is now going through the review and approval process of the Standards Committee of ASTM and the International Commission on Illumination. These values have already been accepted by NASA's Space Vehicles Design Criteria Office.

The solar constant is the energy received from the Sun at the average Sun-Earth distance in the absence of the Earth's atmosphere. The zero-air-mass solar spectrum is the distribution of this energy as a function of wavelength. These parameters are important in many areas of solar physics, meteorology, geophysics, space technology, and other fields. In particular, they are important in the determination of the temperature equilibrium of satellites, the output of solar panels, radiation torques, and the surface degradation of space vehicles.

The value of the solar constant which had been in use for a long time, at least in the United States, was  $2.00 \text{ cal-cm}^{-2}\text{-min}^{-1}$  or  $139.5 \text{ mW-cm}^{-2}$ . It had been proposed by F. S. Johnson of NRL in 1954 and had been based on early ground-based Smithsonian data. Johnson had also proposed a solar spectral curve which became the standard (Figure 1). Values close to these had been proposed by Nicolet in Belgium, Allen in England, Makarova in the USSR, and others.

High altitude measurements made in recent years had produced converging evidence that  $2.00 \text{ cal-cm}^{-2}\text{-min}^{-1}$  was too high a value and that the spectrum required considerable change. In the range of wavelengths greater than  $0.7 \mu\text{m}$ , the presence of highly variable and absorbent water vapor makes ground-based measurements highly unreliable. Hence, an *ad hoc* committee, of which I was the chairman, was formed to propose new standards. Members of the committee were Dr. Drummond of Eppley

Laboratory, Dr. Murcray of the University of Denver, Dr. Gast of AFCRL (retired)—all three of whom had done considerable work in this area—and Laue and Willson of JPL.

After a year's work, we proposed a revised value  $1.94 \text{ cal-cm}^{-2}\text{-min}^{-1}$  or  $135.3 \text{ mW-cm}^{-2}$ , which we felt would be accepted by the international scientific community with a high level of confidence (Table 1). This value is a weighted average of 8 values taken from experiments on the University of Denver balloon, the University of Leningrad balloon, and the Mars-Mariner Probe; from joint measurements by Eppley Laboratory and JPL, from experiments aboard the X-15, B-57B, and CV 990; and from four instruments, two angstroms, a cone, and a Hy-Cal which our GSFC group used on board NASA 711 Galileo in 1967. The new value is 3 percent lower than the Johnson value.

The standard solar spectral curve which we have proposed is based mainly on the GSFC experiment, with modifications based on the filter radiometer data of Eppley-JPL. We have built up a detailed spectral irradiance table for the range of 0.12 to  $1000 \mu\text{m}$ . Of great interest is how the revised curve compares with those proposed earlier. The upper graph of Figure 2 shows the ratio of the values of spectral irradiance from the Johnson table to those from the revised table. In the visible spectrum, the Johnson values are higher by 5 to 10 percent. The lower graph shows a similar comparison with the Labs and Neckel curve. In the visible spectrum, the Labs and Neckel values are lower. In the IR spectrum, differences are greater. Figure 3 shows how the new curve compares with those of Nicolet (rather large differences), of Stair (small differences), and of the GSFC Galileo experiment. Corrections of the order of 1 or 2 percent were made to the earlier GSFC values in order to obtain the proposed new standard.

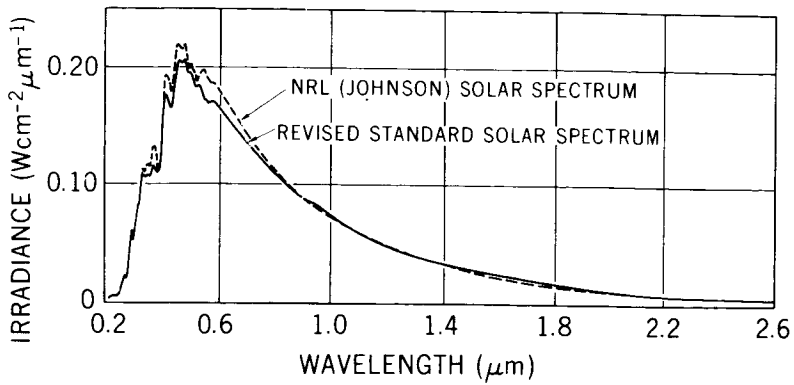


Figure 1—Solar spectral curves.

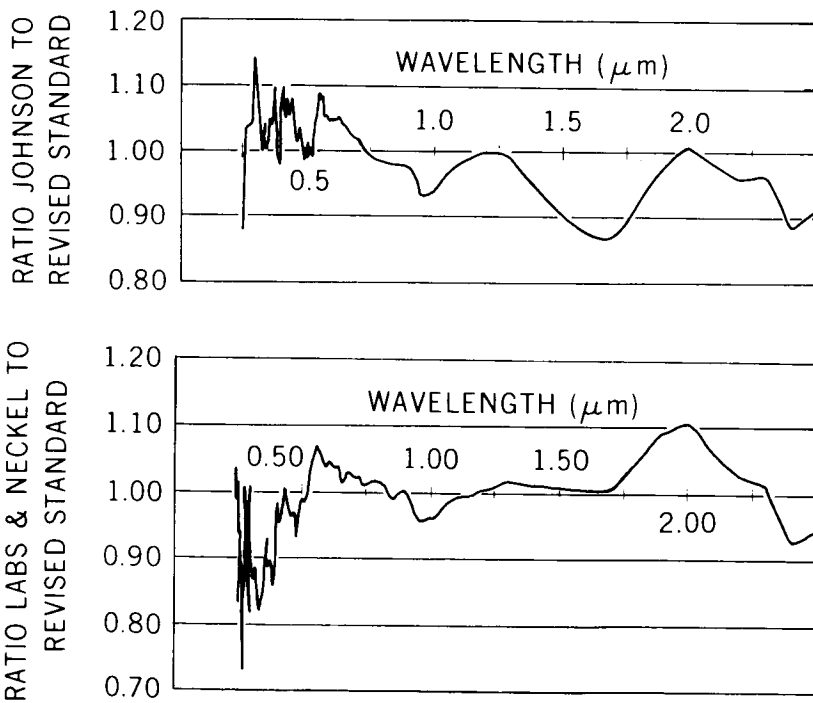


Figure 2—Comparison of revised standard with solar curves of Johnson and Labs and Neckel.

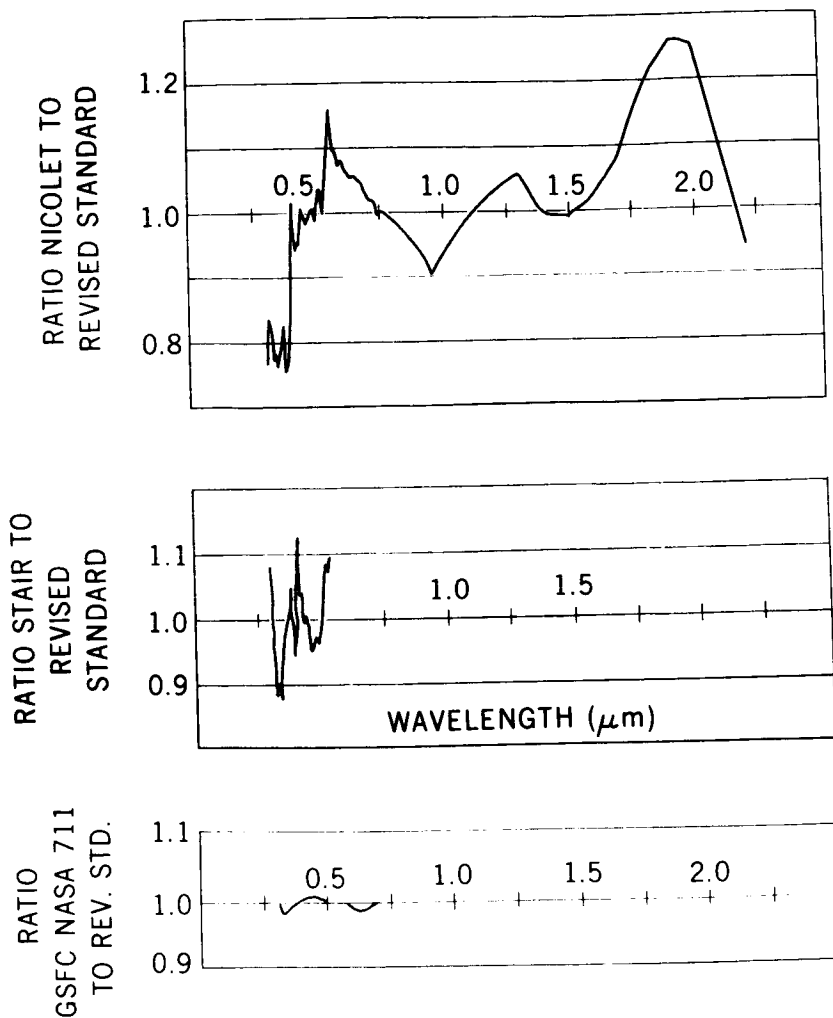


Figure 3—Comparison of revised standard with solar curves of Nicolet, Stair, and GSFC NASA 711.

Table 1—The solar constant.

NRL (JOHNSON) VALUE		139.5 mW cm <sup>-2</sup> (2.00 cal cm <sup>-2</sup> min <sup>-1</sup> )
VALUES FROM HIGH ALTITUDE		
● GSFC Å 6618		134.3 mW cm <sup>-2</sup>
● GSFC Å 7635		134.9
● U OF LENINGRAD BALLOON		135.3
● U OF DENVER BALLOON		133.8
● GSFC HYCAL		135.2
● JPL MARINER CAVITY		135.3
● GSFC CONE		135.8
● EPPLEY-JPL X-15, CV990		136.0
REVISED STANDARD		135.3 mW cm <sup>-2</sup> (1.94 cal cm <sup>-2</sup> min <sup>-1</sup> )

## **A COMPUTER PROGRAM TO AUTOMATE RESIDUAL GAS ANALYSIS**

**H. Shapiro**

About five years ago, a need was foreseen for some system that would automatically determine the gases found in an environmental chamber during spacecraft testing. At that time, this function was performed by a skilled chemist reading the output of a mass spectrometer. At best, this is a time-consuming activity which severely limits the quantity of such scans that the human operator can analyze. Others also foresaw the need for the computer processing of such data, and from time to time the literature would carry a scheme or program to accomplish it. All of these schemes had drawbacks which, when applied to our needs, were insurmountable. For example, one scheme required that a library be built using the exact instrument that would perform the required analysis. Since three different types of mass spectrometer comprising ten individual instruments are in use at GSFC, building such libraries is an impossible task.

In 1968, Trombka and Schmadebeck of GSFC published a least-squares method for resolving complex pulse height spectra which offered a path to a solution to our problem. Using their basic concepts and adding a year's effort, a modification, which is practically a new program, was arrived at. We have a program today, written in Fortran IV and using a matrix inversion method, which successfully analyzes mass spectrometer data. Those aspects of previous programs which were detrimental to our use have been overcome. A library can be built from any published data, such as handbooks, textbooks, compendia, or data generated by other instruments. Results are reasonably good and are understandable in direct proportion to the quality of the library. Thus, data from the user's instrument itself will give nearly perfect answers; from good literature values and a typical mass spectrometer, completely understandable answers; from poor values and poor data, some answers requiring a preknowledge on the part of the user.

Testing the program was done in the most objective manner. Materials were prepared, and mass spectrometric data were taken by one group, and

these raw data were given to a second group who ran the program. Unreasonably difficult mixtures of materials were prepared and run, and the program successfully separated them and printed out a correct analysis each time (see Table 1).

The program is being utilized currently for the solution of experimental spectra, where the spectrometer is being used as a contamination monitor by an untrained spectroscopist.

The ultimate goal is to acquire pushbutton analysis capability. The program is the most difficult link in the chain of steps necessary to achieve this goal. Still required is the electronic hardware for taking the signal from the mass spectrometer, digitizing it, labeling it as to mass number, and putting it on tape in this fashion so that the program can take over. We have begun the work on this last phase and are optimistic that next year all mass spectra can be computer analyzed, and automation will be complete except for the technician who pushes the button.

Table 1—Computer analysis results.

COMPOUND	% RELATIVE ABUNDANCE	
	COMPUTED	ACTUAL
ACETIC ACID	15.3 ( $\pm 2.0$ )	15
ACETONE	64.3 ( $\pm 3.9$ )	75
CARBON MONOXIDE	3.6 ( $\pm 2.2$ )	
ETHANOL	11.3 ( $\pm 1.8$ )	10
ETHYL ACETATE	0.8 ( $\pm 2.0$ )	
3-ETHYL HEXANE	0.4 ( $\pm 1.1$ )	
HYDROGEN CHLORIDE	0.1 ( $\pm 0.7$ )	
METHANE	3.3 ( $\pm 1.1$ )	

## **EXPERIMENTAL THERMAL MECHANICS OF DEPLOYABLE BOOM STRUCTURES**

**Roamer Predmore**

Metal ribbons are processed with a heat forming treatment that enables them to form tubelike structures when deployed from a roll. The size, thickness, perforations, metals interlocking seams, and surface coatings are designed to provide the thermal-mechanical and mechanical structural properties required for the particular spacecraft system. Over a dozen varieties of deployable booms, which range in diameter from 0.6 cm to 5 cm and in length up to 230 m, have been developed, tested, and flown. The deployable booms have been utilized for gravity gradient stabilization on the RAE, ATS, and Nimbus D satellites, and for antennas and instrument probes on the OGO, RAE, and IMP spacecraft. They will be used for instrument support structure on Apollo, Skylab, and for a space flight interferometer presently under development.

The analytic and experimental description of the mechanical behavior and thermal-mechanical behavior of a deployable boom structure has to be developed for each boom design to assure the structural performance required by the spacecraft system. The experimental mechanics and thermal-mechanics studies are conducted with short booms because of the large gravity induced effects on long booms. The anticipated behavior of the long booms on the spacecraft is then scaled from short-boom measurements using an analytic boom model. The technology developed consists of the unique apparatus for thermal distortion measurements shown in Figure 1, the calibration procedure, and all of the thermal static bending plus twist measurements.

The thermal-mechanics test facility is shown in the cutaway drawing in Figure 1. The 5-m-long, massive rigid vacuum chamber supports the 3-m boom test element from an Invar mandrel with the introduction of a minimum of thermal and mechanical background distortion. The space thermal environment is simulated with a collimated tungsten halogen solar simulator and black vacuum chamber walls cooled below  $-190^{\circ}\text{C}$ . The

thermal static distortion of the tip is optically measured and reported in terms of the in-sun-plane bending component, the out-of-sun-plane bending component, and the thermal static twist. The thermal static distortion values are measured as a function of boom perimeter by rotating the boom stepwise in the solar simulator field, as shown in Figures 2 and 3. The distortion values measured at each step are corrected for gravity effects and solar spectrum heating effects.

The thermal mechanics of a seamless tube has been accurately analyzed. Frequently, it is utilized to scale thermal distortion of deployable booms on spacecraft because of its simplicity. Consequently, the tip distortion of a 3-m seamless BeCu tube was measured (Figure 2), found to agree with the analysis, and used to calibrate the test facility. Heat is absorbed on the front of the tube and conducted around the perimeter to the back, which is then at a lower temperature. The thermal expansion of the front is greater than that of the back and causes the in-sun-plane bending. The thermal expansion is equal on each side of the tube; thus, neither out-of-sun-plane bending nor thermal static twist is observed.

The advantages of reduced in-sun-plane bending and thermal static twist provided by the perforated, interlocked Westinghouse boom over the original BeCu overlap STEM are shown in Figure 3. The thermal distortions of the 3-m overlap STEM show large in-sun-plane bending, out-of-sun-plane bending, and large thermal static twist. The out-of-sun-plane bending results primarily from differences between the thermal expansions on either side of the sun plane. The large thermal static twist is characteristic of the overlap element and was predicted by H. Frisch's analysis, presented in the 1969 Science and Technology Review. The perforations and the thermal coatings on the Westinghouse boom are designed to produce a minimum of in-sun-plane bending by obtaining approximately equal heat absorption and equal thermal expansion on both the front and back of the boom. The interlocking seam provides larger torsional stiffness to reduce the thermal static twist.

Table 1 shows several examples of spacecraft applications of thermal static distortion measurements on 3-m deployable booms. Thermal static twist measurements on a 5-cm silver-plated Bi-STEM for Apollo 15 showed that it would twist through a much greater angle than the required  $\pm 15$ -deg. Measurements on the full scale 7.5-m Bi-STEM at NASA-Manned Spacecraft Center showed a 40-deg twist. Design changes will be made to correct

the problem. Thermal static distortion tests on 1.8-cm-diameter interlocked and overlap booms for Nimbus D showed essentially no thermal static twist for the interlocked boom and provided an accurate measure of the thermal static bending. These measurements, along with the spacecraft stability calculations, led to the selection of the interlocked boom for the flight spacecraft. Several designs of the 1.2-cm perforated, interlocked Bi-STEM boom have been tested to develop a flight boom with minimum in-sun-plane bending for a Navy satellite. At present, several deployable boom elements are being tested to optimize the ATS F and ATS G antenna rib design for minimum thermal distortion.

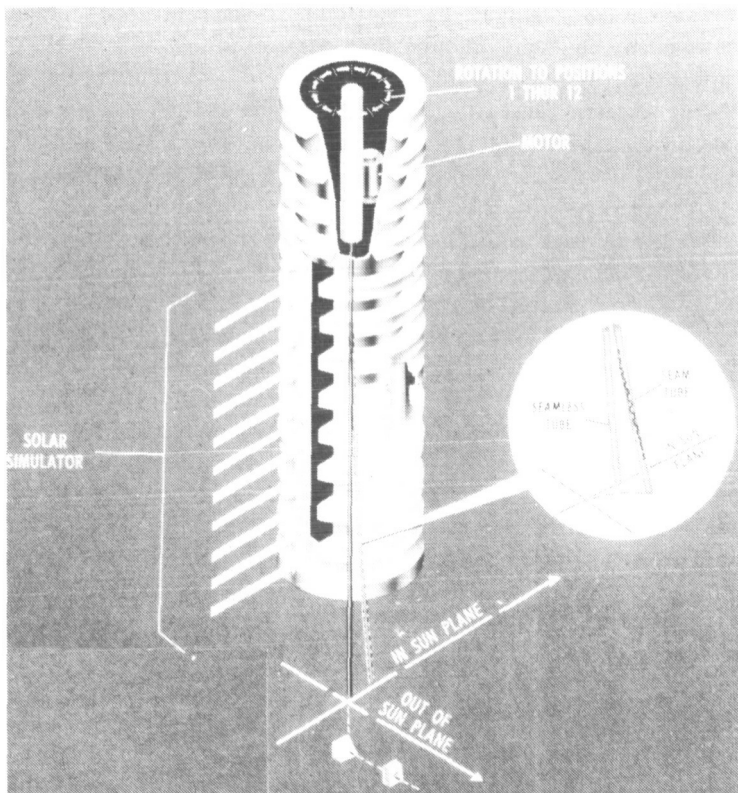


Figure 1—Diagram of the thermomechanical test facility for thermal distortion measurements on the 3-m deployable boom elements.

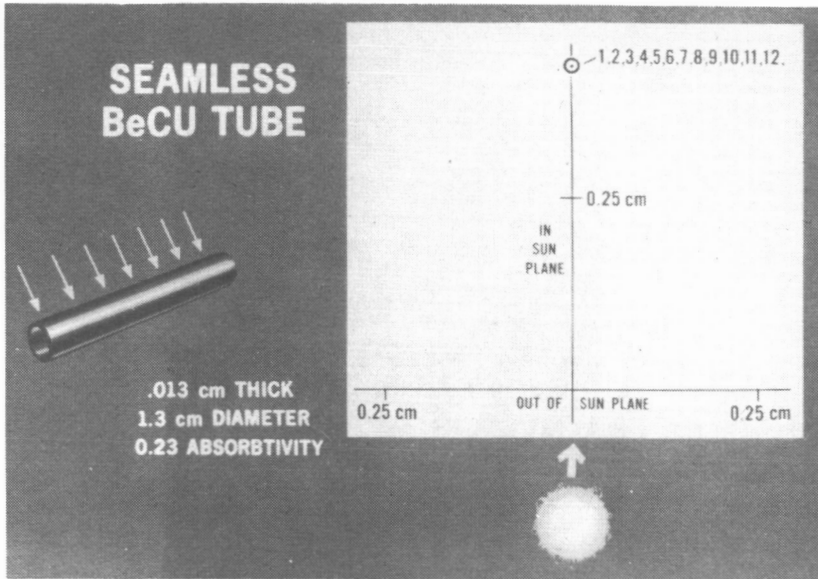


Figure 2—Thermal static bending.

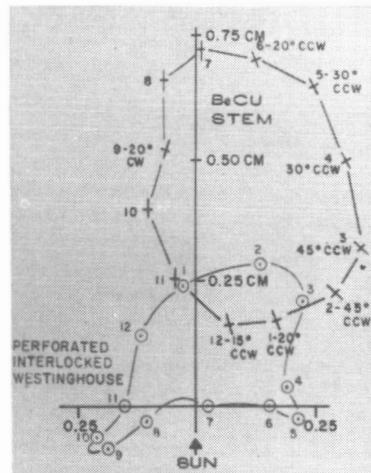
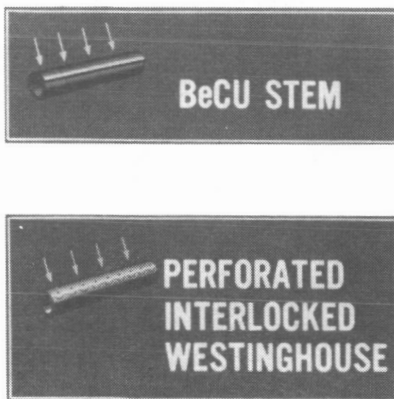






Figure 3—Thermal static bending and twist of the BeCu stem and the perforated interlocked Westinghouse booms.

Table 1—Applications of thermal static distortion measurements.

DEPLOYABLE BOOM	PROGRAM	STRUCTURAL REQUIREMENTS	EXPERIMENTAL RESULTS	REMARKS
4g 5 cm BI-STEM	APOLLO 	SUPPORT AND POINT MASS SPECTROMETER $\pm 15^\circ$	THE BOOM WAS CLAMPED-SEMPRE WITH ANTICIPATED THERMAL STATIC TWIST $\pm 30^\circ$	FULL SCALE TEST IN MSC SES CHAMBER - DIRECT MEASURE OF WORST CASE TWIST
1.1 cm THIN DISC ALLOW OVERLAP	NIMBUS-D 	GRAVITY GRADIENT WITH TP DEFLECTION LESS THAN 30 cm	SHOWED INTERLOCKED BOOM TO HAVE NO TWIST AND 25 cm THERMAL STATIC BENDING	
1.2 cm Part. with BI-STEM	NAVY 	GRAVITY GRADIENT STABILIZATION	SHOWED THERMAL BENDING TO BE MINIMUM FOR DEVELOPMENT BOOM	BOOM DESIGN SELECTED FROM TEST BOOMS
0.14 meter Antenna Rib	ATS FEG 	ANTENNA RIB DESIGN	SELECT PERFORATION PATTERN AND THERMAL COATING FOR MINIMUM BENDING AND TWIST	FUTURE WORK

## DESIGN AND DEVELOPMENT OF A MICROPOUND EXTENDED RANGE THRUST STAND (MERTS)

**Kenneth W. Stark**

The micropound extended range thrust stand (MERTS) was developed to test the various thrusters developed at GSFC. The thrust stand was designed on the basis of the six objectives shown in Figure 1. These design objectives, heretofore, were not found in a single thrust stand. This thrust stand is a torsional measurement device consisting of two major sections, the rotatable horizontal beam and the vertical support tube which is connected through flexural pivots to the fixed frame.

Thrust is measured by sensing of the horizontal displacement of the beam (occurring when the thruster is run). This is accomplished by the use of a differential capacitor sensor capable of sensing  $2.54\text{ }\mu\text{m}$ . The thruster system is mounted at the extremity of the horizontal beam. An electromagnetic coil is used as a forcer and calibrator. Power is brought to the stand through the flexural pivots. All electronic connections are made on the beam. No hard wiring is connected from the fixed frame to the movable assembly, resulting in essentially a frictionless system. Other important features are a counterweight system for static balancing and a telemetry system for housekeeping and thruster data. All six objectives were met in this development. An important, unique feature of this system is its ability to make measurements in the range from  $4.5\text{ }\mu\text{N}$  to  $22.5\text{ mN}$  with a 5 percent accuracy.

Figure 2 shows the thrust stand resulting from our development effort. The rotatable horizontal beam and vertical support column are connected to the outer fixed frame through the flexural pivots. At the front end of the horizontal beam, the electronic signal conditioning and thruster package are mounted. On the rear portion of the beam is the balancing mechanism and transmitter. The fixed frame contains the differential capacitor sensor, forcer-calibrator system, and the optical link command system.

To determine the measurement accuracy of MERTS and to verify the calibration technique utilized, a cesium ion engine was tested. An ion engine produces a thrust which can be calculated exactly, and, therefore, its use is an excellent method for verifying the thrust stand's accuracy. Figure 3 shows the MERTS output (solid line) and the ion engine thrust (dotted one). As can be seen, the MERTS tracked the ion engine to within 5 percent. A check of the thrust stand calibration factor against that of the ion engine calibration factor showed only a 4.3 percent difference.

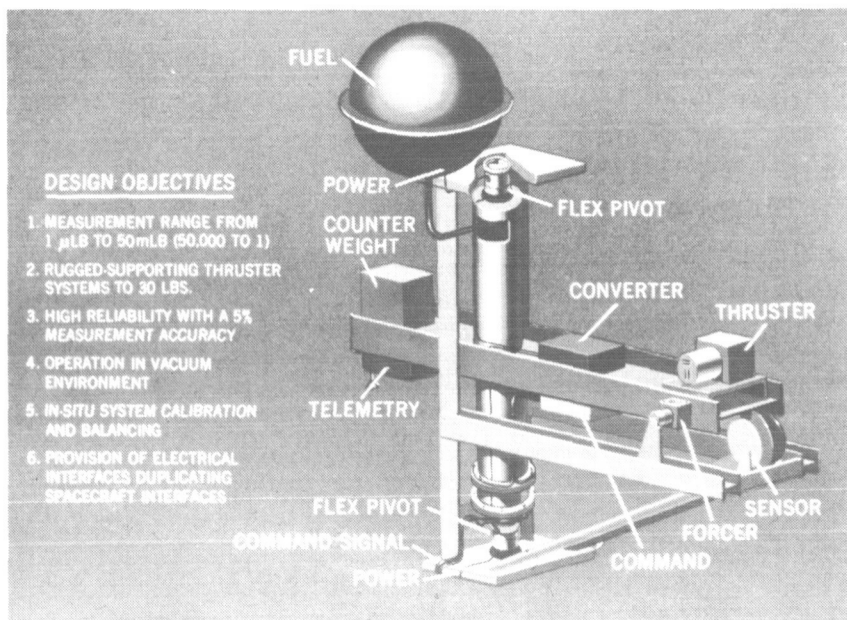


Figure 1—MERTS objectives and design.

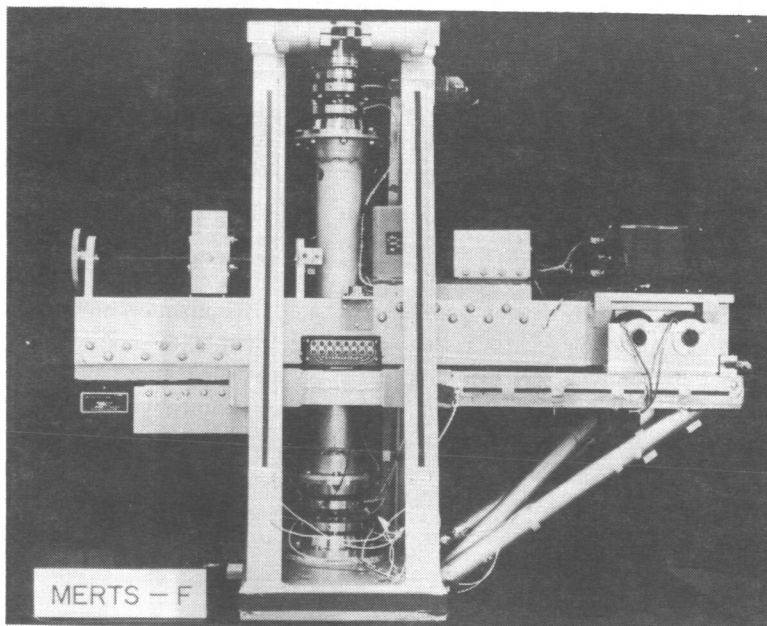


Figure 2—Working model of MERTS.

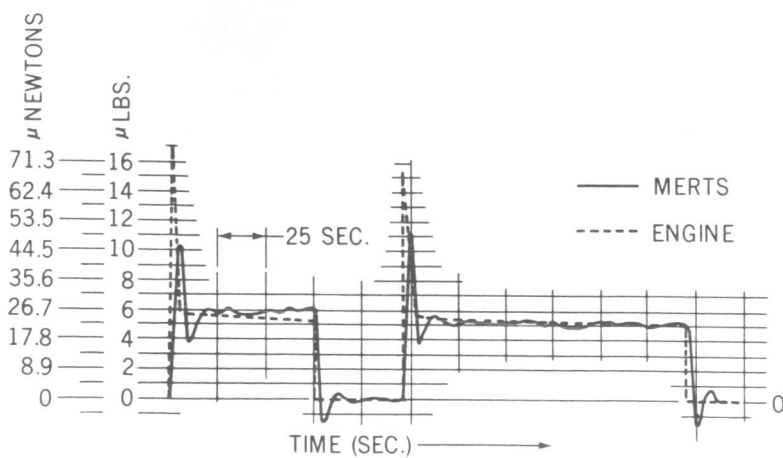


Figure 3—Comparison of thermally compensated MERTS output and ion engine output.

## ULTRA-PRECISE ATTITUDE TEST FACILITY FOR FLIGHT SPACECRAFT

E. J. Devine

To date, it has not been possible to test the stabilization and control systems of large spacecraft in the complete flight-ready configuration. Attempts to conduct systems tests using air-bearing facilities have failed because of the difficulty of maintaining torque-free conditions in the face of convection currents, mass imbalance, and hard wire cable connections. It remains a highly desirable goal to conduct systems tests of the flight spacecraft to assure proper interaction of the various subsystems, the integrity of the flight cable harness and the proposed control system-spacecraft operations procedures.

A facility has been designed and built for conducting complete dynamic systems tests of the OAO spacecraft. The operating principle of the facility is illustrated for a single control axis in Figure 1. In orbit, the spacecraft position  $\theta_s$  is a function of momentum wheel position  $\theta_w$  multiplied by the ratio of wheel inertia to the spacecraft inertia. In the facility, the spacecraft is suspended on a gimballed platform. The wheel position is monitored by means of a synchrotransmitter, and a high gain servo tracks the wheel position. A mechanical gear reduction factors in the ratio of inertias. The result is that the spacecraft motion in the facility simulates precisely that which will occur in the external, torque-free space. The gain of the servo overpowers the extraneous disturbance torques which defeat air-bearing type facilities.

Although simple in theory, implementation of this approach for OAO, where ultra-accurate pointing was desired, placed very stringent requirements on the mechanical design of the facility. Specifically, very low friction suspension, zero backlash, extreme structural stiffness and dimensional stability, and maximum attenuation of building vibration inputs were essential.

Figure 2 shows the complete facility in schematic form. The spacecraft is suspended in the cradle as shown. The cradle is gimballed about two

orthogonal horizontal axes. The base, which supports the gimbal ring, also supports a superstructure for mounting stellar simulators. To complete the capability for testing the spacecraft control system, a precision coelostat provides an inertially fixed optical beam for stimulation of the fine guidance error sensor in the observatory telescope. Thus it is possible to test the inertial reference unit and to conduct realistic transfers of control between the inertial package and the stellar guidance sensor.

Figure 3 shows the test facility which was built and employed successfully to test the stabilization and control system of the OAO B flight spacecraft. Fine pointing of the spacecraft, under the control of the GSFC experiment package was demonstrated to better than 0.5 seconds of arc. Other spacecraft functions tested included

- Gimbaled star tracker operation,

- Boresight star tracker operation,

- Coarse slew maneuvers,

- Fine slew maneuvers,

- Operation of the inertial guidance package including demonstration of the proposed in-orbit drift correction,

- Settling time of the spacecraft control system, and

- Transfers between all modes of control (automatic and/or commanded as appropriate).

The facility is presently being upgraded, with the goal of testing the OAO C spacecraft with a pointing stability approaching 0.1 seconds of arc. The facility concept demonstrated here could also be employed for preflight testing of any spacecraft employing momentum exchange devices for control muscles.

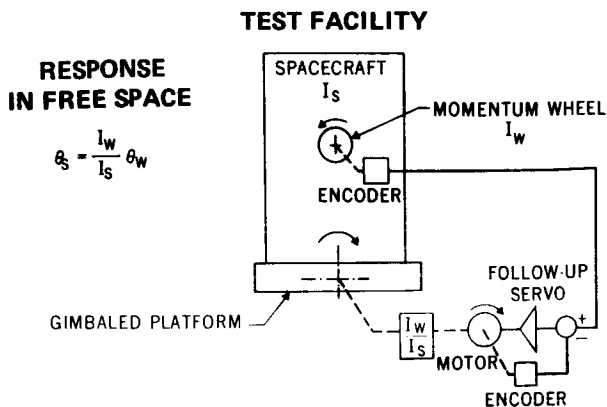


Figure 1—Operating principle of the OAO fine pointing test facility.

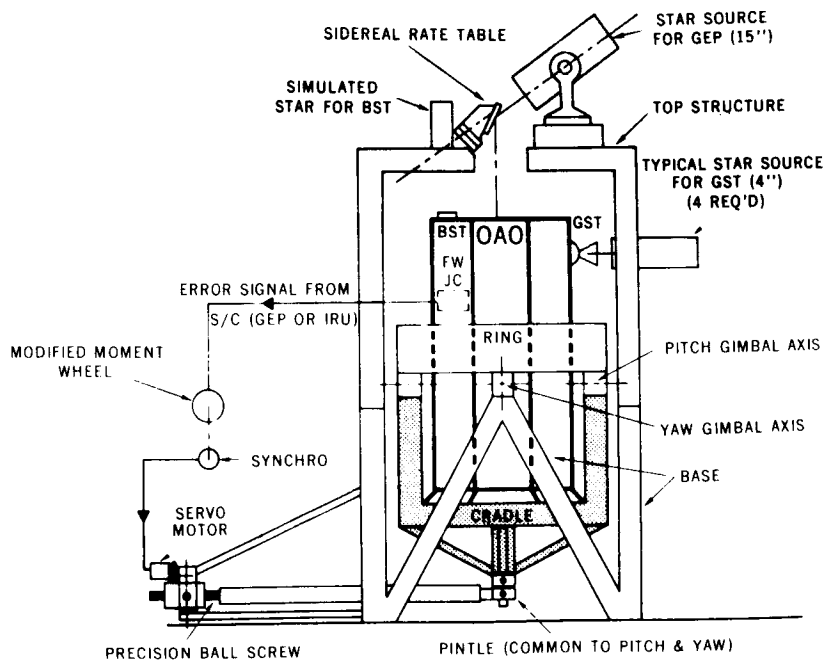


Figure 2—OAO fine pointing test facility (schematic).

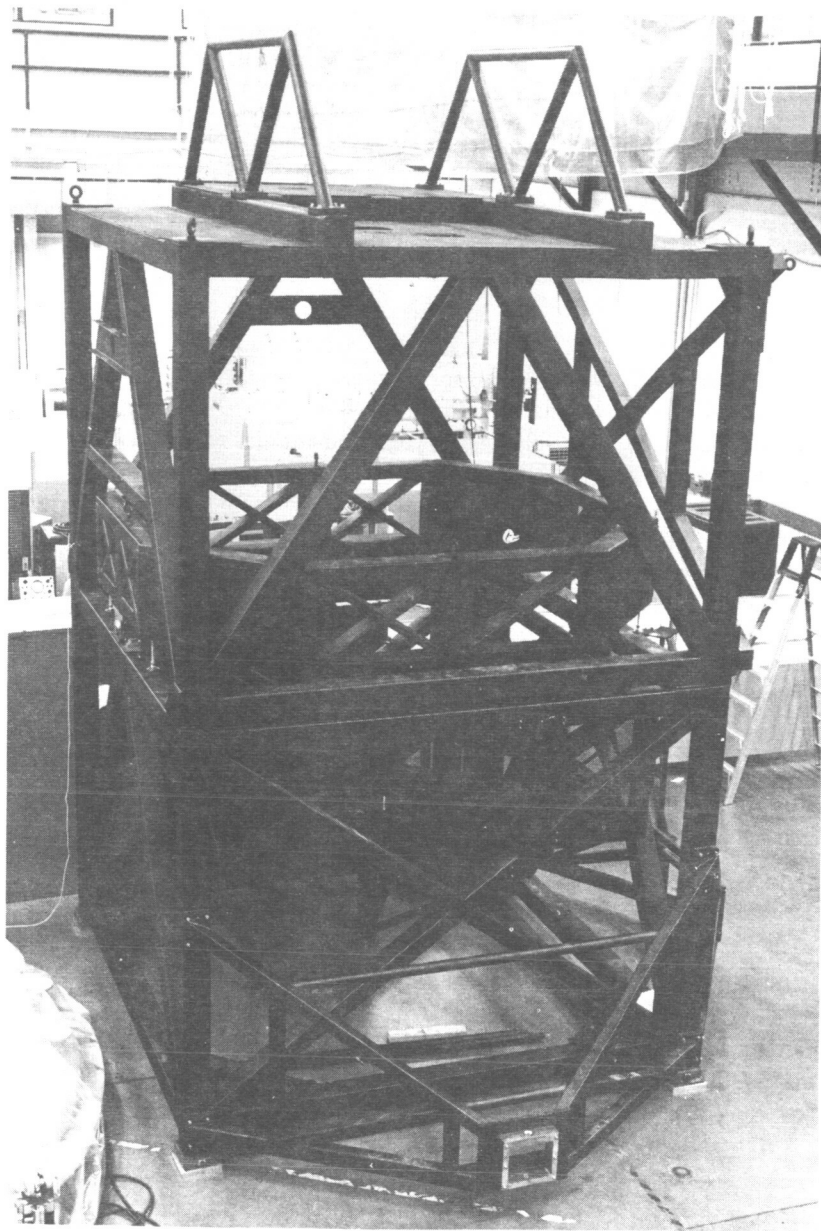


Figure 3—OAO fine pointing test facility.

## **IMPROVED LASER RANGING ACCURACY THROUGH DYNAMIC THRESHOLD COMPENSATION**

**T. S. Johnson**

Laser satellite tracking systems are now being used in support of geodetic and Earth physics programs. The value of the laser tracking system in these programs is dependent on the range noise and the range bias over widely varying conditions for typical satellite passes. During the recently completed preliminary polar motion experiment (an experiment in which two laser ranging systems on a north-south line simultaneously tracked a satellite to determine motion of the pole), new techniques for improving both the range noise and range bias were demonstrated. These techniques typically improved the GSFC laser ranging systems from the former 1.5-m accuracy level to the 20- or 30-cm accuracy level.

The range accuracy of a laser satellite ranging system, separate from that introduced by time jitter and instability in electronic components (presumably small), is dependent on the transmitted pulse duration and the resulting shift in the time of triggering the start and stop of the time interval counter, caused by variations in both transmitted and received signal levels, when a fixed trigger threshold setting is used. This effect for three different received signal levels is illustrated in Figure 1, where the time difference relative to the center of a typical 20 ns transmitted pulse duration is shown. The fixed threshold setting determined by the horizontal line intersects the three pulses at 4, 8, and 14 ns relative to the center of the pulses. However, if the amplitude of the received pulse is the only varying parameter, it can be shown that by adjusting the threshold to a constant value of the peak amplitude, i.e., 50 percent, there is only a constant time offset relative to the center of the pulse.

Dynamic adjustment of the detection threshold is accomplished (Figure 1) by measuring the peak amplitude of the received pulse, recording this value, and then using it to set the threshold level of the threshold detector and trigger generator. The original received pulse, after a known delay, is then detected at the required level, and a trigger pulse is generated

to stop the range time interval unit. The dynamic electronic threshold circuitry is capable of measuring pulses having varying amplitude, but fixed shape, with a precision better than 1 ns over a wide dynamic range.

The need for threshold compensation is shown in Figure 2, which illustrates the variation in signal level throughout a typical satellite pass. The measured signal level in photoelectrons varies by more than 100 through the pass with a predominance of high levels at the closest range as expected. The wide variation in signal level from point to point is due to atmospheric perturbations, inhomogeneous beam distribution, corner reflector interference effects, and tracking error, whereas the systematic variation from low to high to low signal level is due to range changes, increased atmospheric path length, and changes in the optical cross section of the satellite with elevation angle.

The corrections to the measured ranges (based on these received signal levels relative to a fixed correction that would have been applied if pulse height information was not available) are also shown in Figure 2. The overall correction span exceeds 4 m, which is far in excess of the observed rms for this pass. Furthermore, visual inspection of the corrections implies that any orbit determined by these corrections would be biased from the true orbit.

Figure 3 shows the improvement that pulse height information and electronic threshold adjustment make for short arc orbital fits. The laser ranges for a satellite pass are used to determine a short arc orbit, and then the measured ranges are compared to the computed orbit. The range residuals are plotted as a function of time throughout the pass. The upper plot shows a noise level of 1.4 m, typical for a constant correction, while a noise level of 24 cm is obtained when the pulse height correction techniques are employed. More important than the reduction of noise level, however, is the reduction in the bias implied in Figure 2.

Noise level and range bias in laser ranging systems can best be reduced by a reduction in transmitted pulse duration below the required precision; however, it has been demonstrated that even existing long pulse systems (20- to 40-ns duration) can be improved to the 20- to 30-cm level of precision without major or expensive changes to the system.

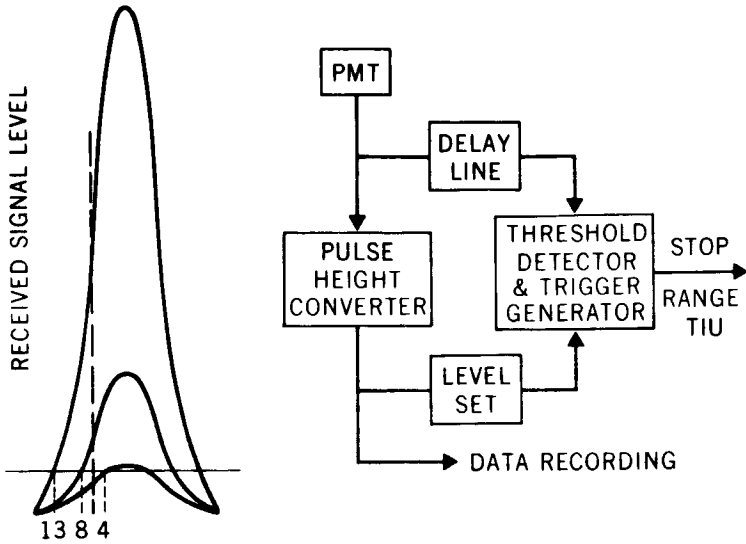


Figure 1—Dynamic threshold compensation.

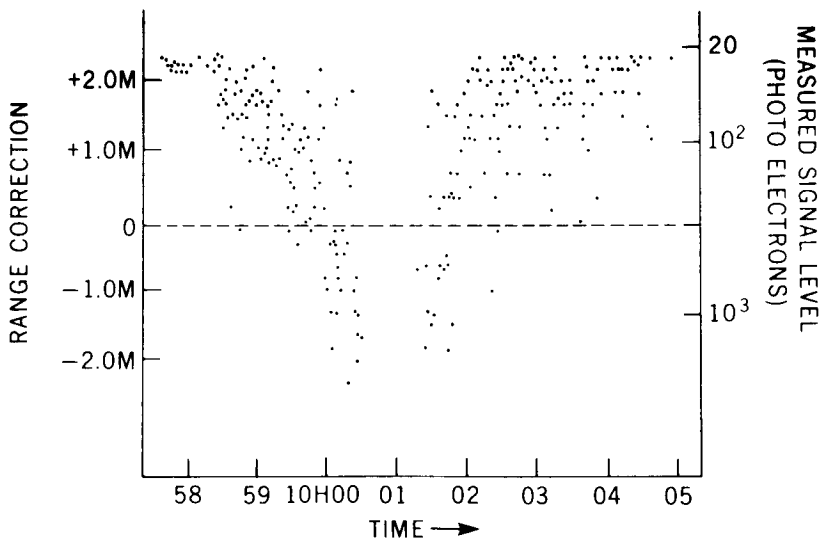


Figure 2—Range correction based on received signal level.

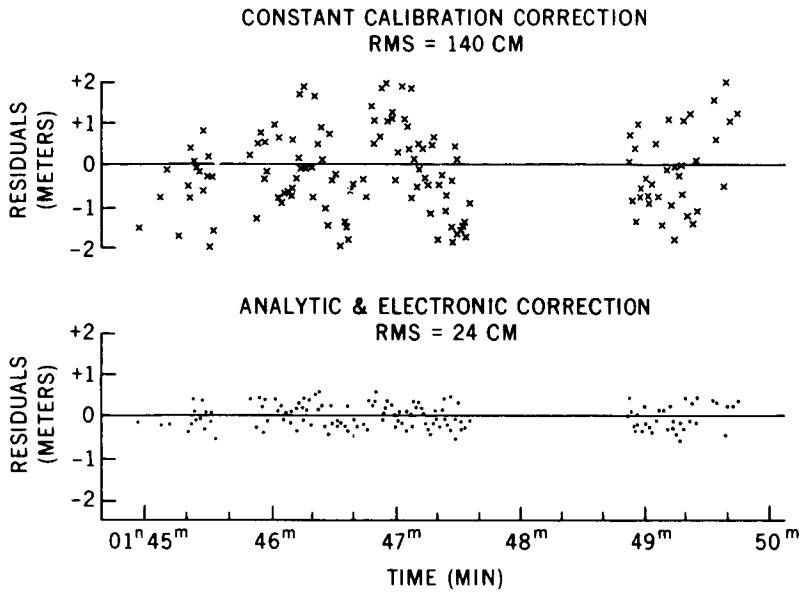


Figure 3—Laser range residuals.

## **STADAN ANTENNA GAIN CALIBRATION USING RADIO STARS**

**Ralph E. Taylor**

An antenna gain measurement method has been developed that utilizes a signal emitted from a radio star, such as Cassiopeia A or Cygnus A, to determine absolute antenna gain at 136 MHz and 400 MHz for antennas in the STADAN network. The standard technique is to use an aircraft to determine the gain of STADAN antennas. Antenna gain determinations made with an aircraft reference the measured antenna gain to a standard-gain antenna. Uncertainties in the gain of the standard antenna, system calibration errors, polarization errors, and parallax errors make the aircraft method generally less accurate than the radio-star approach.

As far as station antenna gain measurements are concerned, the adoption of the radio-star method by the stations would eliminate the necessity for a NASA aircraft to visit the stations to make gain measurements. Furthermore, a radio-star gain determination then could be made by site personnel at any time, in a matter of minutes, whereas up to several hours of flying time over the site is required for the aircraft method. A series of over 60 STADAN antenna gain calibrations have been completed over the past year, and each station's antenna gain was measured using both the radio-star and aircraft methods.

In order to make an antenna gain measurement with a radio star, the only special equipment required is an inexpensive square-law diode detector "black box" connected at the intermediate-frequency output from a station receiver (Figure 1). The addition of this "black box" converts the station's RF receiving system into a total power receiver like that used in radio astronomy applications. To determine a station's antenna gain by means of a radio star such as Cassiopeia A, it is only necessary to make two dc voltage measurements at the output of the square-law detector/filter network. These two simple measurements consist of an off-star voltage reading, which includes the contribution of the star's background sky temperature, and an on-star voltage reading which is made with the peak of the antenna's main

lobe pointing directly at the radio star (Figure 1). A necessary condition for the off-star reading is that the antenna's axis be rotated to position the radio star in the first null of the antenna's radiation pattern; however, since the radio star is essentially a point source, this poses no problem.

An error analysis of the radio-star gain determination method for the radio stars and antennas considered here shows that the overall standard deviation uncertainty in antenna gain is only  $\pm 0.6$  dB ( $1\sigma$ ). At 136 MHz, using Cassiopeia A, the mean values and  $1\sigma$  uncertainties in the parameters influencing the overall gain uncertainty include a background sky temperature of  $900 \pm 100$  K, obtained from a radio map; a flux density of  $(13.8 \pm 1.1) \times 10^{-23}$  W-m<sup>-2</sup>-Hz<sup>-1</sup> for Cassiopeia A; a  $1\sigma$  error of  $\pm 10$  percent in the voltage measurements obtained from the square-law detector; and other uncertainties in the various parameters used in the expression for effective antenna gain (Figure 1).

The series of over 60 antenna gain calibrations recently completed at the stations, verifies that the square-law detector output voltage  $1\sigma$  error is indeed within the allowable limits of  $\pm 10$  percent. (A number of detector voltage measurements were averaged to determine the standard deviation for a given gain calibration.)

The representative antenna gain determinations shown in Table 1, obtained from the series of over 60 determinations made using a radio star, reveal that the overall standard deviation uncertainty in effective antenna gain is close to  $\pm 0.6$  dB. In each case, the uncertainty in each radio-star gain determination was computed using the specific detector voltage measurement error for that determination. The values of  $1\sigma$  quoted in Table 1 also reflect uncertainties in the other parameters influencing effective antenna gain at both 136 MHz and 400 MHz.

The  $\pm 1.5$  dB uncertainty in the corresponding aircraft gain determinations is admittedly heuristic but is, nevertheless, based upon discussions with personnel who made the aircraft measurements. This uncertainty includes the influence of the various error sources, mentioned earlier for the aircraft method.

It should be recognized that both the radio-star and aircraft gain determinations were made at the stations by an independent group under the supervision of GSFC personnel.

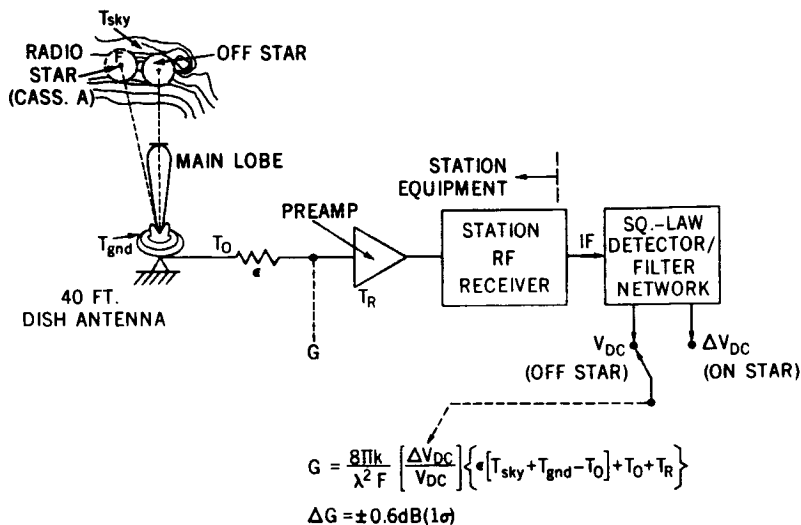


Figure 1—Antenna gain calibration using radio star.

Table 1—Antenna gain measurements.

STADAN STATION	TYPE ANTENNA	FREQ (MHz)	G EFFECTIVE ANTENNA GAIN	
			STAR (db ± 1σ)	AIRCRAFT (db ± 1σ)
QUITO	SATAN	136	19.3 ± .59	19.9 ± 1.5
QUITO	40' DISH	136	16.9 ± .61	16.0 ± 1.5
SANTIAGO	SATAN	136	20.7 ± .59	21.0 ± 1.5
ALASKA	SATAN	136	20.8 ± .68	20.6 ± 1.5
MADAGASCAR	SATAN	136	20.3 ± .47	20.1 ± 1.5
MADAGASCAR	40' DISH	400	29.9 ± .47	30.4 ± 1.5
JOBURG	40' DISH	400	29.7 ± .59	28.7 ± 1.5

## COMPUTER CONTROLLED ANTENNA SYSTEM

Nicholas A. Raumann

With the advent of relatively cheap and small computers on the market, digital techniques have become very attractive for application to the servo and control systems of large antennas. A small dedicated digital computer can be used to perform an automatic checkout and readiness verification of the servo system. In addition, the computer can be used to replace certain pieces of existing hardware. Such a system has several advantages: reliability and consistency of operation, minimization of turnaround time between satellite passes, fast identification of component or subsystem failures or misadjustments, and in the case of new antenna procurements, substantial savings on special equipment requirements. Digital techniques have been evaluated at GSFC's Network Test and Training Facility using the 40-ft data acquisition antenna and the Sigma V computer. Figure 1 shows the programs that have been written for the monitoring and automatic checkout of the antenna servo system.

During normal operation of the system, the computer monitors critical quantities such as power supplies, oil temperatures, and axis velocity. Abnormal conditions are flagged to the operator, and if conditions warrant it, direct action is taken by the computer.

The antenna operator can call for a startup program. This program automatically brings the antenna up to operational status by properly sequencing the various switching functions.

A readiness test program can be called which is intended as a short prepass check of the servo system. This program checks power supplies, interlocks, the hydraulic system, and the servo amplifier. As a final test, a step function is applied to the antenna, and its transient response is evaluated according to a predetermined performance index. If all of these tests pass satisfactorily, the antenna is declared operational. If not, the operator is informed of the particular problem and is given the choice of operating the antenna in a degraded mode or of calling for the complete test program, which will help in further pinpointing the problem.

The complete test program checks for items such as tachometer gain and ripple, error sensitivity, synchro operation, friction, low speed performance, and hydraulic leakage and finally generates a diagnostic message to the operator. This program can also be called during the performance of routine maintenance because many tests of this program coincide with tests required by standard maintenance procedures.

Figure 2 shows the tracking loop for an antenna as it exists at a STADAN tracking site. The antenna structure is driven by a hydraulic drive system, and the tachometer, receiver, and encoder provide feedback signals from the structure. The tracking loop is closed via the servo amplifier and the receiver or the antenna position programmer, depending on the operating mode selected. Offline, the PB 250 computer is used to generate prediction data, and a scan generator is provided which aids during the satellite acquisition phase.

All of these devices, with the exception of the antenna structure and its sensors, are special-purpose equipment ranging in size from one chassis to several racks. The functions of these devices have been replaced with a program on the same computer. Test results indicate that the digital system has a performance that is equal to or better than the performance of the existing system.

With the use of the computer approach, a third mode has been added to the antenna: the augmentation mode.

This mode permits operation in the program mode with the addition of a correction factor derived from the receiver which is passed through a low-pass filter and integrator (Figure 3). Thus, the antenna is driven by a signal with high signal-to-noise ratio, as it would normally be during program mode operation, but improved pointing capability is provided by the introduction of the average receiver output.

In the lower half of Figure 3, the response of the augmentation mode is shown at a time when the antenna was tracking Nimbus 3. First, autotrack performance is shown; then, the operator switches to program mode. (Note the offset in this mode caused by a combination of antenna misalignments and prediction error.) Then, the augmentation mode is selected, and the error goes to zero after an overshoot.

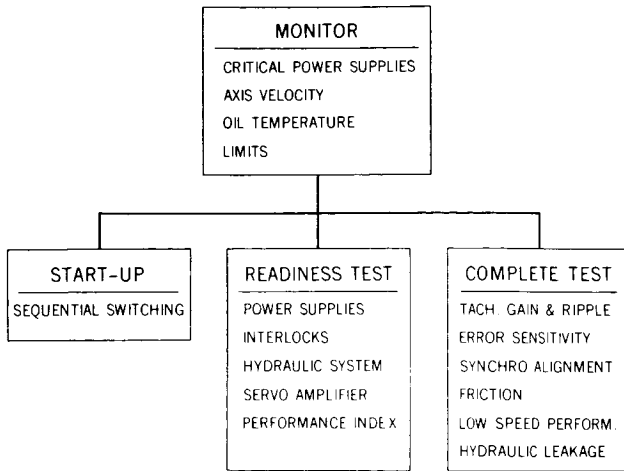


Figure 1—Program for the monitoring and automatic checkout of the antenna servo system.

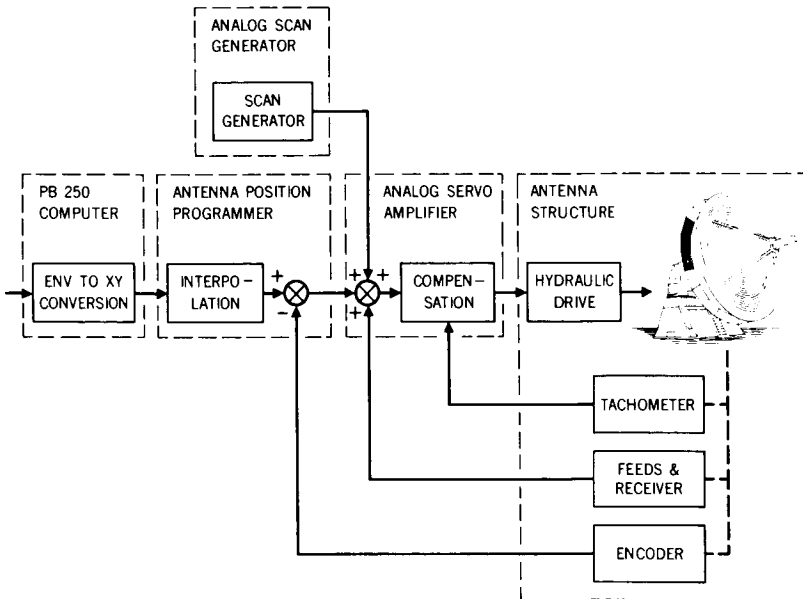


Figure 2—Tracking loop for a typical STADAN antenna.

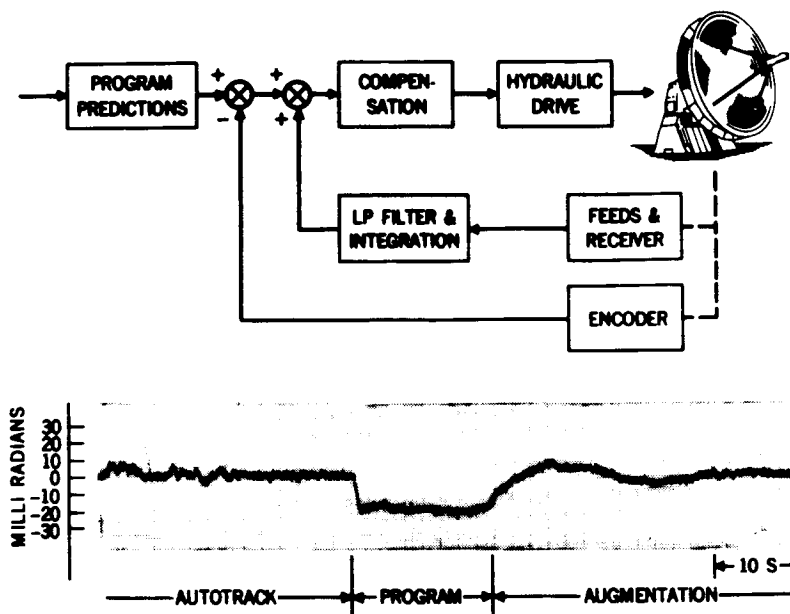


Figure 3—Configuration of the tracking loop with augmentation added and the response of this loop (tracking error versus time).

## DICHROIC SUBREFLECTOR FOR ROSMAN II

**Julius A. Kaiser**

This paper reports on the dichroic subreflector of the Rosman II antenna. Figure 1 is a picture of the Rosman II dish, which has both focal-point and Cassegrain feeds. The rear of the ground screen on which the focal-point feeds are mounted can be seen between the square feed box and the solid metal subreflector, which was used with the Cassegrain feed operating at 4 and 6 GHz. In order to use the focal-point feeds in this system prior to installing the dichroic subreflector, it was necessary to remove the subreflector and to replace it for Cassegrain feed use. The turnaround time required for this was several hours and required that riggers be available whenever the changeover had to be made. The risks to personnel and equipment involved in removing and replacing the subreflector, and the personnel complications associated with changes in shifts made this operation somewhat undesirable.

A dichroic subreflector functions as shown in Figure 2. It is virtually transparent to a baseband of frequencies and the focal-point feeds look through it as though it were not there. At the Cassegrain feed frequencies, on the other hand, it is highly reflective, which permits normal Cassegrain operation. Simultaneous operation with both focal-point and Cassegrain feeds is thus provided without the need of removing the subreflector.

Also shown in Figure 2 is a picture of the 3.35-m dichroic subreflector, developed at GSFC, for the Rosman II antenna system. It is a sandwich construction, 1.9-cm thick, and consists of two laminated epoxy glass skins 1-mm thick separated by a phenolic honeycomb core. Visible on the front surface is an array of circular copper discs. On the opposite surface is a similar array. These two surfaces were designed to give maximum reflectivity in the 4-GHz portion of the C band. Since the arrays are resonant, some deterioration in performance is to be expected in the 6-GHz portion of the band.

The dichroic subreflector was installed in the Rosman II dish during the latter part of last November and is still in operation. Some solar heating of

the dichroic was encountered in the dish. This was eliminated by painting the surfaces with white epoxy paint so that if one were to see the dichroic now it would be very similar in appearance to the solid metal subreflector which it replaced. Tests made to date have been directed at (1) making focusing adjustments and measuring those system parameters which would be most indicative of a focused condition for the Cassegrain feed and, to a lesser extent, (2) determining losses for the focal point feeds due to the presence of the dichroic.

The C-band test results were derived from measurements of radiation patterns, noise temperatures and carrier-to-noise ratios at 4.1 GHz, and the relative transmitter power at 6.3 GHz that was required to produce a 1-MHz tone in the ATS 3 satellite. This latter measurement, when compared to transmitter power level required in operations with the original solid metal subreflector, provides a measure of loss at the transmitter frequency attributable directly to the dichroic subreflector. The measured loss at 6.3 GHz was 1.3 dB at the best focus position.

The increase in noise temperature caused by the use of the dichroic over that caused by the use of the solid metal subreflector arises from resistive losses in the dichroic. The measured increase in noise temperature for the dichroic over that for the original metal subreflector at 4.1 GHz was approximately 8 K, corresponding to a resistive loss of about 0.1 dB.

There is also a reactive or scatter loss at 4.1 GHz which must be added to the resistive loss to account for the total loss in gain when the dichroic is used. This scatter loss does not, in general, contribute to noise temperature but does represent energy not collimated usefully by the antenna. With the ATS 3 used as a source, the carrier-to-noise ratio was measured. When this parameter is related to the noise temperature of the system, a gain figure can be established. If the gain figure obtained using the dichroic is compared with that obtained using the solid metal subreflector, the total gain loss due to the dichroic can be deduced. At the best focus position, this gain loss was 0.3 dB at 4.1 GHz. It was felt at the time those measurements were made that even better performance could have been obtained with more time available for adjustments.

For the focal-point feeds, abbreviated measurements of loss due to the dichroic were made at 137, 400, and 1700 MHz and compared to that with

no subreflector at all. Gain degradation at 137 and 400 MHz was virtually unmeasurable. At 1700 MHz, the measured value was under 1 dB.

We have heard that the focal point feeds have been used more extensively since the installation of the dichroic. The deterioration in performance associated with use of the dichroic is believed to be more than offset by the increase in operational availability of the system.

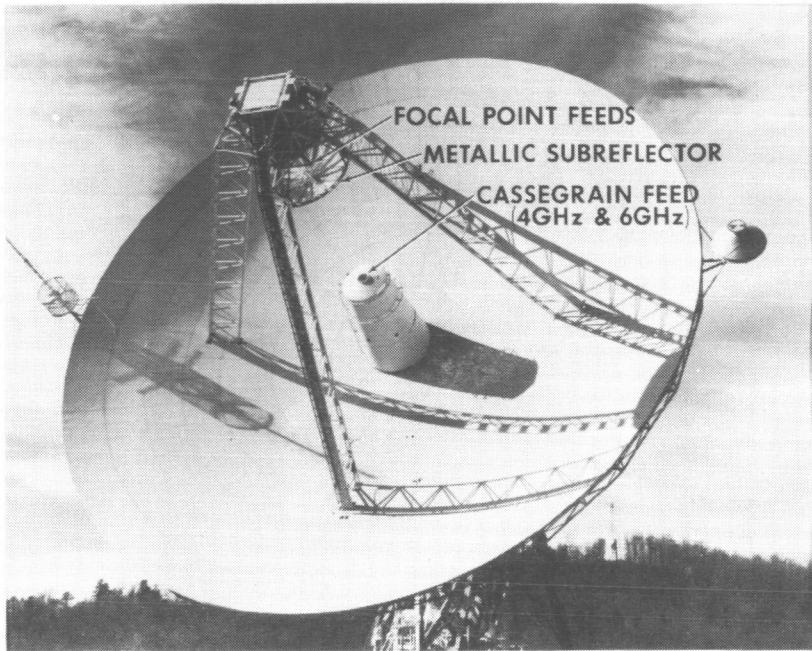


Figure 1—Rosman II antenna.

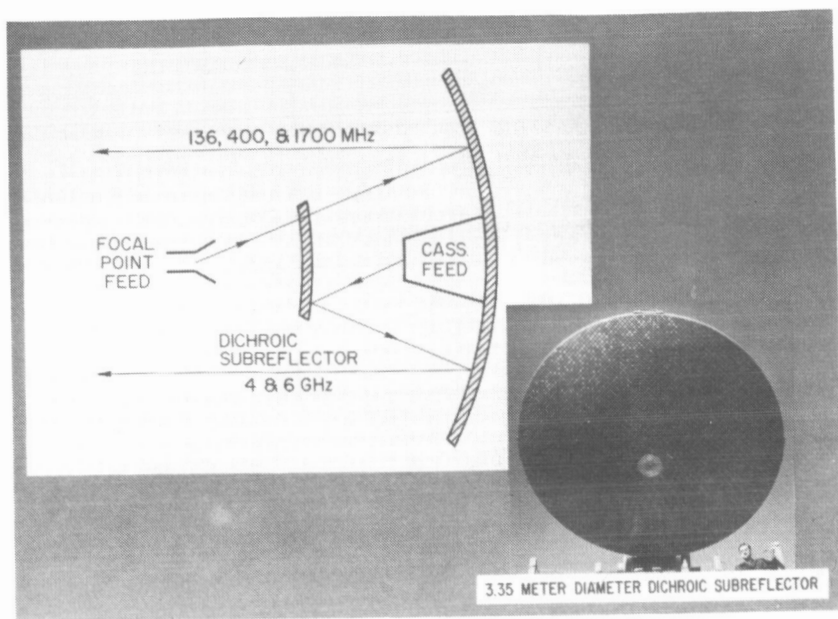


Figure 2—Dichroic function.

## SIGNAL COHERENCE STUDIES IN MULTIAPERTURE ARRAYS

Leonard F. Deerkoski

The gain capability of a single-aperture antenna is limited by surface tolerance. Figure 1 is a plot of gain versus antenna diameter, normalized to wavelength. The lower curve indicates the state of the art in single-aperture antenna gain in 1965. The upper curve represents the current state of the art as defined by the antennas listed on the figure. Although 73-dB gain is technically feasible, the antenna cost increases exponentially as the antenna size enters the nonlinear portion of the curve. In this region, it becomes economically desirable to array several smaller aperture antennas, each of which falls in the linear portion of the curve, instead of constructing a single large antenna.

Each time the number of array elements is doubled, the gain requirement of each antenna is theoretically reduced by 3 dB. The feasibility of arrays is dependent upon the ability to achieve close to the theoretical gain improvement through coherent combination of the array elements. The importance of this factor has prompted the construction of a two-element array to measure the gain improvement that can be realized while tracking spacecraft. These measurements were taken at VHF and at S-band.

The array at VHF consisted of two five-element Yagi subarrays shown in Figure 2. One of these Yagi antennas is shown at the left, the second Yagi antenna is barely noticeable in the distance. At S-band, two 4.6-m diameter reflectors were used with focal point mounted monopulse feeds. At each frequency, the gain improvement of the array over that of a single element was determined by measuring CNR at the output of the coherent combiner and comparing this to the CNR at the input channels. These gain improvement measurements were repeated at 20-s intervals for the duration of the satellite pass. ATS 3 was used as the transmitter at VHF, and Apollo 12 at S-band.

Since these measurements indicate "instantaneous" CNR in each channel, the randomness of the noise in the input channels generally

resulted in unequal CNR's at these points. For any given set of measurements, the maximum theoretical CNR (gain) improvement at the output over that of the best input channel is defined by the relative CNR between input channels. The measured gain improvement fell within 0.5 dB of the theoretical maximum with 90-percent probability at VHF and 93-percent probability at S-band.

Unless time delay correction is included in the system, the spacing between array elements will cause a reduction in the bandwidth capability of the array. This bandwidth limitation is due to the added path length the signal must travel to be received at the first element as compared to that for the second element. Figure 3 indicates the maximum loss in SNR at band edge versus bandwidth for several antenna spacings. The wider spacings shown in Figure 3 are beyond that required to overcome mutual shadowing and are considered for applications where atmospheric inhomogeneities cause severe phase front distortion. One such application is used at the NASA tracking stations in South America where spatially correlated ionospheric fading at VHF dictates a spacing of at least 300 m for optimum performance.

An automatically controlled time delay correction system has been developed and tested for this program. The time delay circuits were inserted in the IF stage of the coherent receiver. A fixed 2.909- $\mu$ s delay was placed in channel 1 and a variable delay circuit was placed in channel 2. The variable delay is digitally selectable in increments of 90.9 ns (one wavelength at IF) with a maximum delay of 5.808  $\mu$ s. The setting of the variable delay unit is calculated from the azimuth and elevation of the spacecraft, which uniquely define the required delay for any given antenna separation. The calculation requires 25 ms, but the actual switching time is less than 50  $\mu$ s. The variable delay control speed is sufficient for tracking rates of up to 0.05 rps. Incorporation of the time delay system into the receiver had no measurable effect on receiver phase or AGC.

The effect of using this time delay system is to extend the bandwidth capability of a two-element array for any spacing up to 850 m to that which would be available with no time delay system at a 15-m spacing, a bandwidth extension of 50 times.

In summary, arrays of large aperture antennas are a feasible solution to the problems posed by the technical and economic limitations of single

aperture antennas, and these large arrays can operate within at least 0.5 dB of their theoretical gain capability. The greatest disadvantage of multi-aperture arrays, bandwidth limitation, can be essentially eliminated if digitally controlled time delay correction circuits are used.

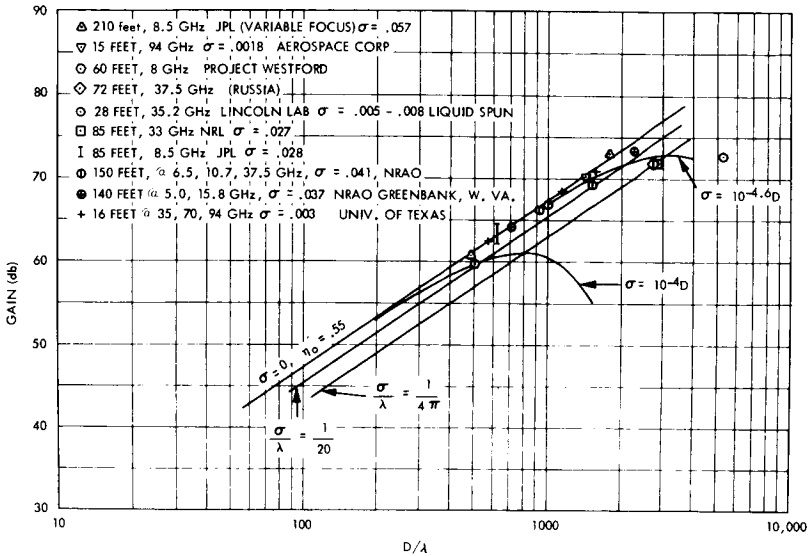
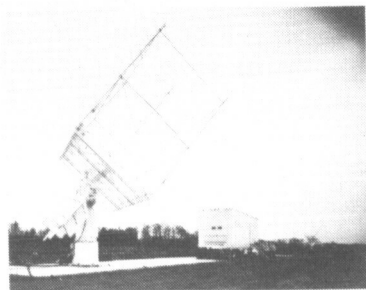


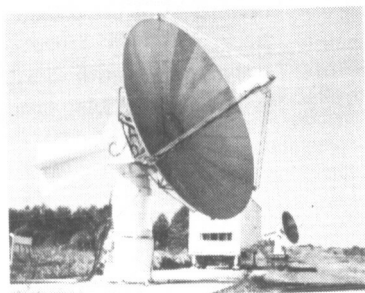
Figure 1—Antenna gain versus surface tolerance.



VHF

SPACECRAFT	ATS-3
FREQUENCY	136.47 MHz
NUMBER OF MEASUREMENTS	3000

% OF DATA WITH GAIN IMPROVEMENT WITHIN 0.5 db OF THEORETICAL	90%
---	-----



S-BAND

SPACECRAFT	APOLLO 12
FREQUENCY	2287.5 MHz
NUMBER OF MEASUREMENTS	2280

% OF DATA WITH GAIN IMPROVEMENT WITHIN 0.5 db OF THEORETICAL	93%
---	-----

Figure 2—Measured gain improvement.

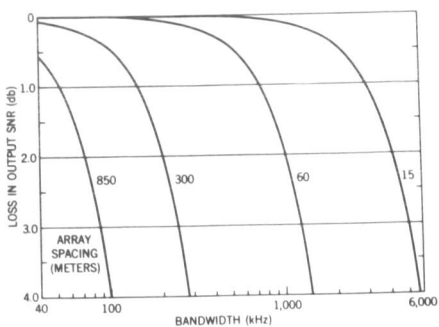
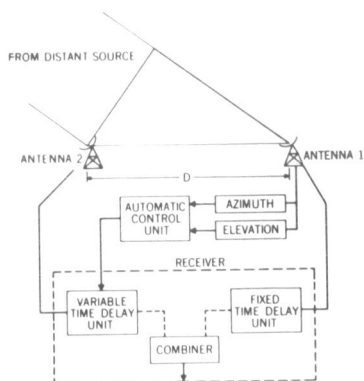


Figure 3—Array bandwidth.

## THE NAS-PAK LOGIC SYSTEM

**James Billingsley**

For the past eight years, the design and fabrication of telemetry ground data processor equipment at Goddard Space Flight Center have been accomplished through the use of commercial logic cards or modules. Each design engineering group selected a manufacturer logic system which suited their particular requirements. Unfortunately, these logic systems were not physically or electrically compatible with each other; thus, competition was eliminated when additional purchases were made. As integrated circuits improved in performance and price, an opportunity for performance and size improvement motivated us to investigate new methods of implementation of the integrated circuits. A microelectronics program was initiated to evaluate circuitry, packaging methods, and fabrication approaches necessary to produce a competitively procured logic system. Goals of this micro-electronic program were

- (1) In integrated circuit evaluation, to evaluate circuit elements for their electrical performance, their availability from numerous sources, and the completeness of the logic line.
- (2) In special circuit development, to design and test additional circuitry unavailable in the form of integrated circuits and to develop techniques that will allow competitive manufacture.
- (3) In hardware development, to design and develop modular rack-mountable hardware to house the integrated circuits.
- (4) In software development, to provide the designer with computer-generated design, fabrication, and drafting assistance to reduce cost and the incidence of human error.
- (5) In testing and documentation, to evaluate available test equipment and fixtures for use with the new logic system and to provide a user's manual for the logic system and the program aids.

The result of this microelectronic program of investigation is the NAS-PAK logic system described in this report.

The NAS-PAK logic system emerged more from the integrated circuit dual inline package than from any other aspect of the logic system development. Circuit evaluation was performed without regard to package type. Hardware development, however, required consideration of each package type. The familiar printed circuit card was discarded because of connector pin number limitations. A socket panel with plug-in capacity for 60 14-pin dual inline packages was chosen. These panels (shown in Figure 1) are 15.2 cm X 17.8 cm X 0.32 cm with 14 wire-wrap pins per socket. Six socket panels are mounted on an aluminum frame (Figure 2) which in turn is mounted in an 8.9-cm drawer assembly (2 frames) or a vertical page assembly (3 frames). Figure 3 illustrates the modular assemblage from dual inline package to drawer assembly. Plastic protective covers are attached to the frame assemblies to prevent pin damage. The drawers assemblies have provision for mounting 4 fans, 2 fans, or a blank fan plate to facilitate cooling as required. The vertical page assembly is cooled by rack-mounted fans. Figure 4 illustrates the vertical page assembly (8 pages) mounted in a cabinet rack. The resultant reduction in size averages 15:1 over discrete component logic systems and 2:1 over commercial lines of integrated circuit modules.

Miniaturization of electronic equipment introduces the difficulty of circuit interconnection in very small areas. Automation of circuit interconnection then becomes necessary for full utilization of the system capabilities in normal time schedules. Realization of these problems early in the NAS-PAK system development led us to investigate wiring machines and their capabilities. The machine chosen, though manufactured by only one manufacturer, is available on a rental basis from several companies; thus, competition is preserved.

The wiring machine eliminated manual wiring errors and human deficiencies in the fabrication area but offered no improvement for design modification or correction after wiring. Computer programs were written to minimize errors introduced at the design phase. (See Figure 5.) These programs reduce the modifications and corrections required by eliminating the most common design errors before wiring. Figure 6 shows a typical intermediate printout demonstrating computer subroutines which provide design diagnostics, module placement guides, and circuit-use charts to

further aid the user. Figure 7 illustrates the autowire program flow from logic diagram to the wired chassis. Additional programs were written to provide function block entry and automatic drafting of the designer's input data.

The block entry program reduces the input wirelist card number by generating wirelist cards from a single descriptive statement. Large shift registers and counters may be entered with a statement such as "-32 SRS." The block entry program will then generate all interconnection wiring cards necessary to wire the shift register as determined by the block entry function library. Since the designer does not have a drawing of the function, it became necessary to develop a program to show the designer how the computer implemented his input statement. The auto-draft program provides drive information to an x-y plotter to draw the logic symbols with module type, socket, and pin information. The symbols are positioned on the paper by coding information provided by the designer or the computer on the wirelist cards. The interconnecting lines are not drawn by this program and must be drawn by hand. Since the symbols and designation information consume 90 percent of hand drafting time, the auto-draft program offers considerable design assistance. Figures 8 and 9 are flow diagrams which show the complete NAS-PAK software system. User-oriented instruction manuals have been written for the NAS-PAK hardware and software.

The NAS-PAK logic system is a complete system covering all phases of implementation, not just the hardware phase alone. Each of the design aids were developed after the realization that previous developments introduced difficulties which would require additional effort by the designer. With these intentions, the NAS-PAK logic system will continue to develop.



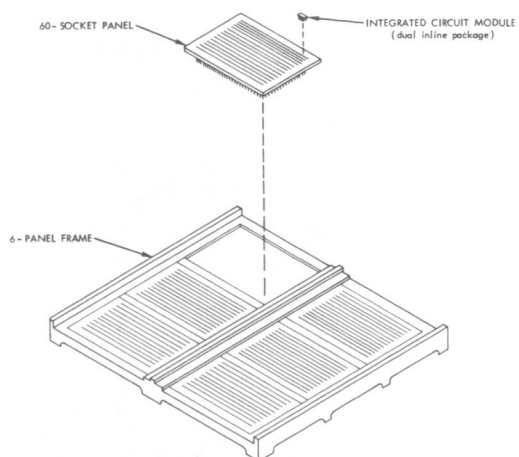


Figure 2—Socket panel mounting scheme.

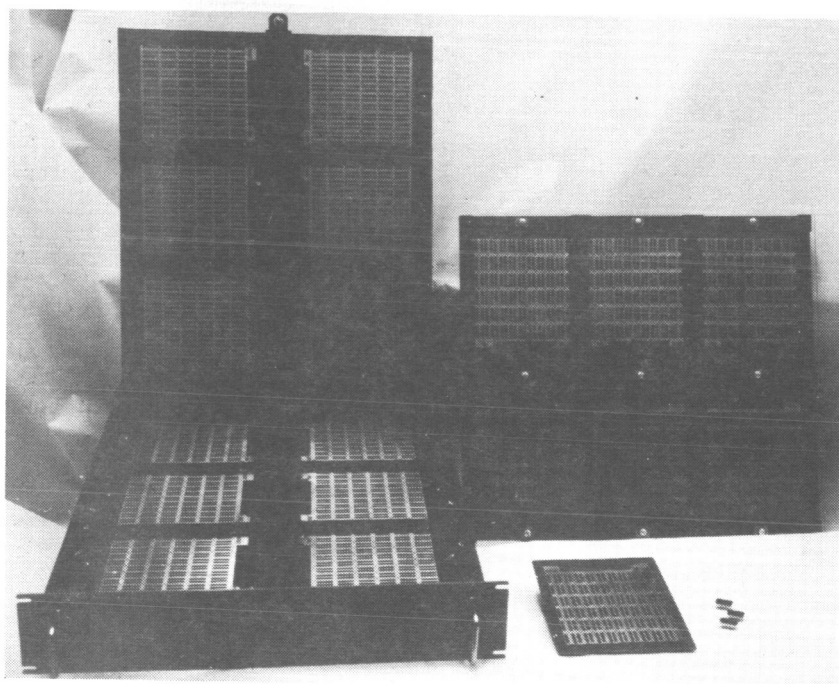


Figure 3—Modular assemblage.

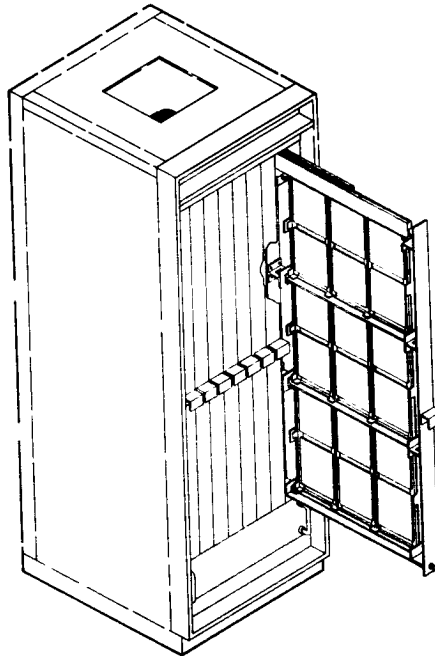


Figure 4—Vertical page assembly.

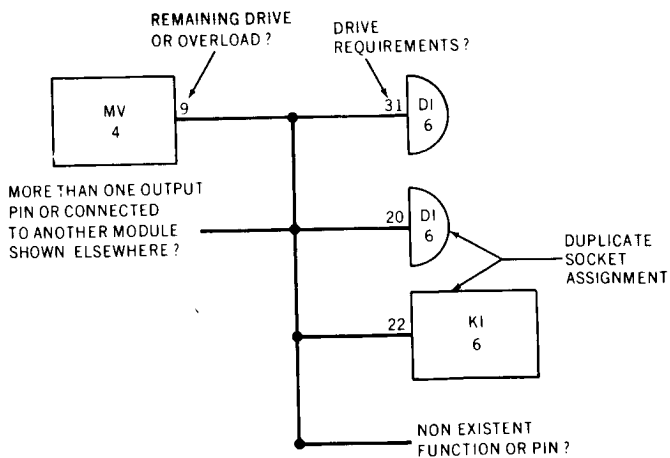


Figure 5—Logic design aid program test.

```

*** PIN LIST PRINTOUT ***

=====
PART 10. DIAGNOSTIC STATEMENTS
=====
PIN NOT LISTED -- PIN NUMBER NOT FOUND UNDER MODULE TYPE 14 MODULE DATA LIBRARY, OR
MODULE TYPE NOT FOUND IN LIBRARY.

MISCELL -- NETWORK CONTAINS MIXTURE OF SIGNAL, MOVE-EXPANDER, OR POWER PINS.

OVERLOAD -- LOADING EXCEEDS OUTPUT DRIVE CAPABILITY.

SINGLE PIN -- NETWORK CONTAINS ONLY ONE PIN.

MULTI PIN -- NETWORK CONTAINS TWO OR MORE OUTPUT PINS.

NO OUTPUT -- NO OUTPUT PIN IN NETWORK.

MULTI MOD -- TWO OR MORE DIFFERENT MODULE TYPES ASSIGNED TO SAME SOCKET.

UNIQUE CARD -- IDENTICAL CARD (U ENCL) REFERENCED.

COMMON PIN -- PIN COMMON BETWEEN TWO NETWORKS.
=====

NETWORK NR. 201
609 3 FN 3 12 201 OUT 8 609
610 3 FN 3 6 201 INP -1 610
611 3 NO 10 3 201 INP -1 611
REMAINING DRIVE = 6 UNITS.

NETWORK NR. 202
612 3 FN 3 11 202 OUT 8 612
613 3 NO 10 2 202 INP -1 613
REMAINING DRIVE = 7 UNITS.

NETWORK NR. 203
615 3 NO 8 5 203 OUT 8 614
616 3 NO 10 1 203 INP -1 615
616 3 NN 7 12 203 INP -1 616
617 3 NN 7 13 203 INP -1 617
618 3 NO 8 6 203 INP -1 618
619 3 NN 7 2 203 INP -1 619
620 2 NN 55 9 203 INP -1 620
REMAINING DRIVE = 2 UNITS.

```

Figure 6—Computer subroutines.



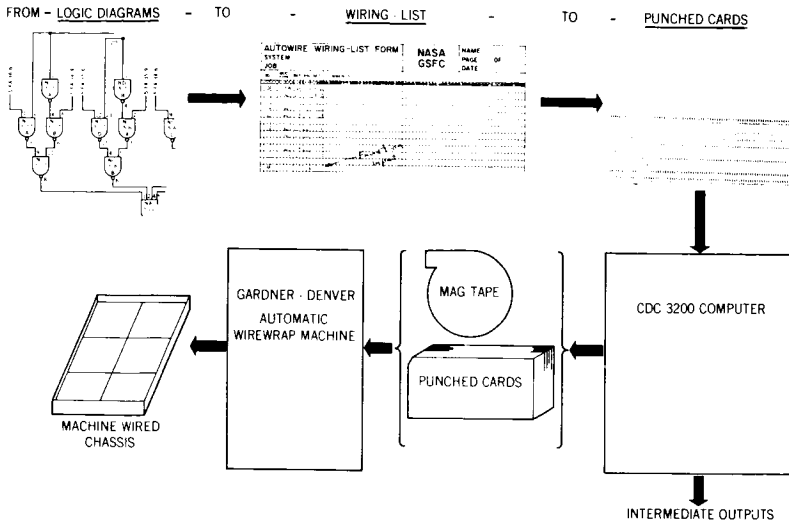


Figure 7—Autowire program flow.

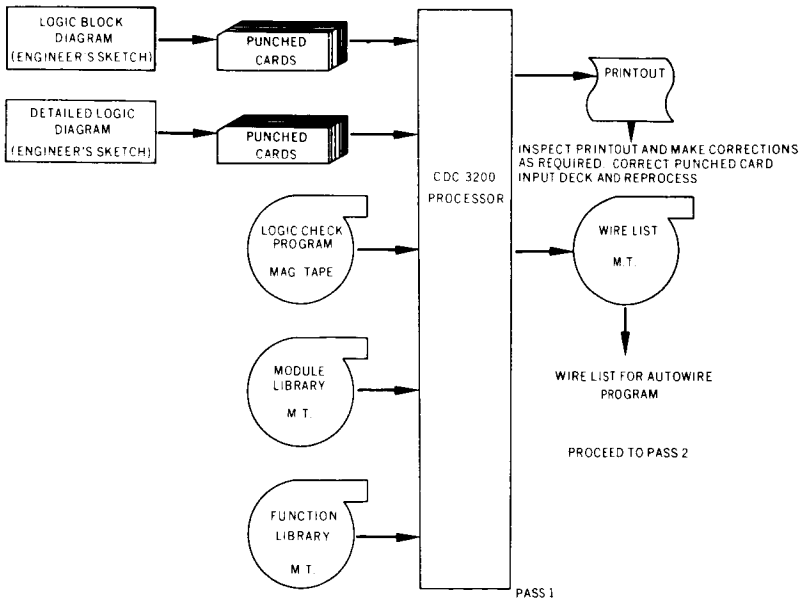


Figure 8—Logic design aid program.

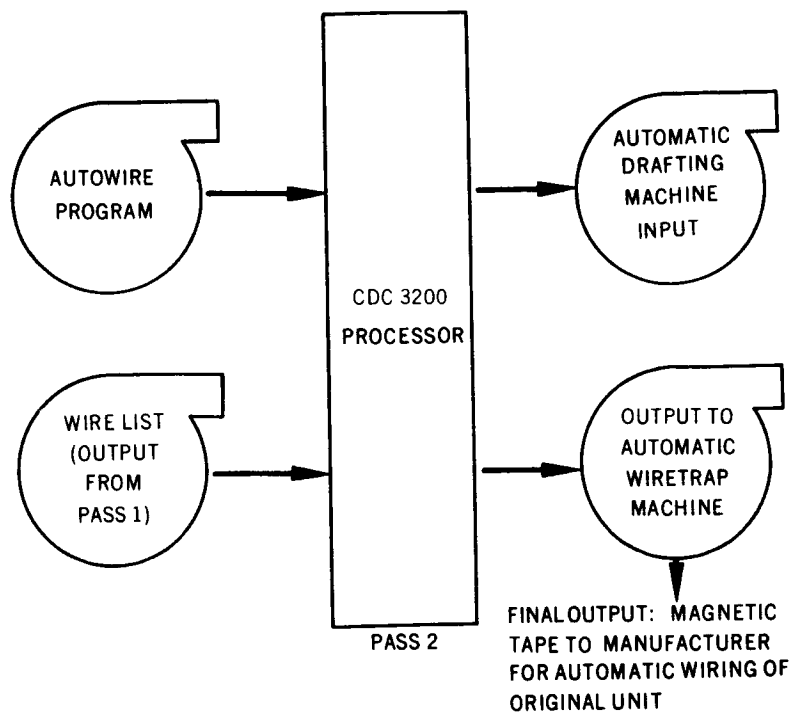


Figure 9—Automatic wiring program.

## **SIMULATION OF MASS STORAGE SYSTEMS OPERATING IN A LARGE DATA PROCESSING FACILITY**

**Richard Holmes**

We are studying the kind of data processing facility that we will need in the near future to meet the expected workload and to obtain the desired operational benefits, including cost benefits. The most recent studies in this area have centered on facilities built around mass storage systems. A mass storage system, as we use the term, is capable of providing storage for up to  $1 \times 10^{12}$  bits of data and access to any part of this data within a few seconds. This quantity of data is equivalent to about one year of the data flow into our facility.

The configuration in which such a mass storage system might operate is shown in Figure 1. The mass storage system is shown here providing storage for data between the input processor and the intermediate processor, which is a UNIVAC 1108 complex. The mass storage simulation program simulates the behavior of such a mass storage system operating on-line with the UNIVAC 1108.

The simulation program was written to aid system designers in the design of a new data processing facility. The simulation accomplishes this by providing a tool to measure the overall effect on the facility of on-line mass storage systems and by providing a means for measuring and comparing the performance of competing mass storage systems.

Table 1 shows how well the simulation performed. Four different cases were simulated for a 1-hr period of production processing. Each case required only 2½ min to simulate. In the first case, magnetic tape was used to input data to the UNIVAC 1108; this is the present mode of operation of the UNIVAC 1108. The second and third cases were mass storage systems, and the fourth case was an idealized situation which put an upper bound on the amount of production that can be processed in the 1-hr period. A large difference in throughput between mass storage system 1 and mass storage system 2 is probably explained by the figures in the last column, which

show the amount of data available within milliseconds to the UNIVAC 1108. Mass storage systems have the characteristic of providing millisecond access to that subset of the total data which is mounted in the reading device. Mass storage system 2 had very little data available within milliseconds and had to spend too much time performing time-consuming "fetch" operations to retrieve additional data.

These results show that competing systems can be compared by the use of the simulation program and that the simulation program can be used as a design tool by system designers. Future plans for the simulation include (1) making it easier for designers to use, (2) simulation of other mass storage systems and comparisons of them to those discussed here, and (3) enlargement of the scope of the simulation to include a larger part of the operations of the facility, such as the on-line input of data from the input processor.

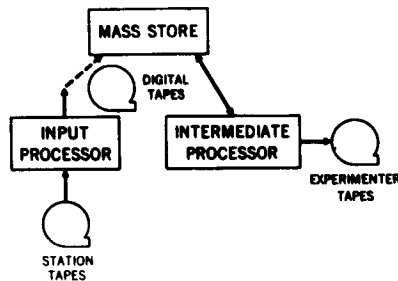


Figure 1--On-line mass storage system block diagram.

Table 1--Results of 1-hr simulation of Univac 1108 processing.

SYSTEM	JOBS COMPLETED	DATA AVAILABLE IN MILLISECONDS (REELS)
TAPE (EXISTING)	24	1
MS #1	32	50
MS #2	2	0.1
IDEAL	38	$\infty$

## **FEASIBILITY MODEL OF A VIDEO INSTRUMENTATION RECORD/REPRODUCE SYSTEM**

**J. L. Tinsley**

Instrumentation video record/reproduce systems will be required for STADAN, ERTS, and Goddard Space Flight Center data processing facilities in the early 1970's. We began our program early in 1968 by conducting parallel feasibility studies to determine the system configuration that satisfied specific performance requirements. Two companies, RCA and Ampex, both competent in video record/reproducers, were given study contracts, and the better approach, by Ampex, was chosen for a prototype video record/reproduce system. Performance evaluation with this unit will serve as a basis for specifying production-type machines to satisfy both STADAN requirements and the new requirements coming from the ERTS project. These machines will require improvements in frequency response, high data rate PCM, multispeed capability, time displacement error, tape utilization, bit error rates, and reliability (Table 1). First, to obtain perspective, let us look at the Ampex FR-600. This is not intended as a one-to-one comparison, but the FR-600 is used because many people are familiar with this machine. The Ampex FR-600 series recorders used in STADAN have 0.6-MHz frequency response. The FR-2100 offers more than a ten-to-one improvement over the FR-600. This also applies to most of the other parameters listed in Table 1.

The design goals set in 1968 for frequency response were dc to 10 MHz with a 6-MHz minimum. The frequency response obtained in the Ampex FR-2100, on the other hand, was dc to 10 MHz and dc to 10 MHz/32 for a second speed. The PCM digital performance design goals were 14 Mbit/s with 11 Mbit/s minimum. Those obtained were 16 Mbit/s. Tests were conducted to 20 Mbit/s. This was achieved by using the 10-MHz bandwidth and Miller code PCM. For multispeed, two speeds were required. Those obtained were a longitudinal speeds of 38.1 cm/s (15 ips) and 1.19 cm/s (0.47 ips) and scanning speeds (rotating head) of 50.3 m/s (1980 ips) and 1.57 m/s (61.9 ips).

The design goal for time displacement error (TDE) was 25 ns minimum; less than 15 ns was obtained. Tape utilization (packing) of 116 kbit/cm<sup>2</sup> (750 kbit/in.<sup>2</sup>) was the design goal; 85.3 kbit/cm<sup>2</sup> (9550 kbit/in.<sup>2</sup>) was obtained. A bit error rate of 1 error in 10<sup>5</sup> was the design goal. Presently it is estimated to be 1 error in 10<sup>6</sup> or an improvement by a factor of 10 over the design goal. Dual gap head assemblies were desired for improved reliability. Redundant recording eliminates tape dropouts. Manufacturing technology limits this development at this time, and dual gap heads were not incorporated in the FR-2100.

Figure 1 shows a picture of the developmental model, the FR-2100, scheduled for delivery in January 1971. In the lower left of the figure, a swept frequency response of the system is shown. The top curve is for the reproduce mode. The bottom curve shows a bypass of the tape, utilizing electronics only, that illustrates the near transparency of the tape medium. The picture on the right demonstrates a PCM non-return-to-zero at 16 Mbit/s from both off tape and electronics-to-electronics. The future plans for this system involve (1) verification of all performance parameters upon receipt of the equipment, (2) determination of the full capabilities of the digital system such as multilevel coding, and (3) determination of the reliability and head life characteristics.

In the development of such a system, one must continually look at other devices and sources to determine the present-day state of the art. This system has been five years in development, and other independent gains have been made. Some present-day performances are illustrated in Table 2. The two nearest competitors would be the Newell model AV-1500R wideband longitudinal recorder and the RCA modified TR-70. The Newell recorder is capable of a 15-MHz frequency response. This response is obtained by high speed longitudinal recording. This approach has a maximum recording time of 80 s/pass, unsuitable for continuous type recordings. The RCA TR-70 has a full 10-MHz frequency response. This should offer good competition on any new procurements. The system has been demonstrated as a laboratory setup, and some additional work will be required for a production system. The PCM digital capabilities for the Newell system are 20 Mbit/s per channel operating at 2440 cm/s (960 ips). The capability of the RCA unit should be equal to the Ampex FR-2100.

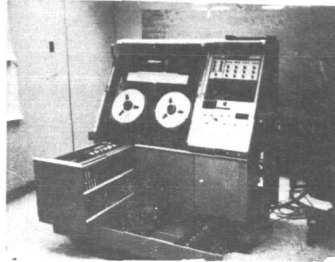
For multispeed, the Newell is supplied with the 7-speed transport at 38.1 cm/s (15 ips) to 2440 cm/s (960 ips). The multispeed capability was

demonstrated by RCA on another system. The time displacement error on the Newell recorder is of the order of 3000 ns because this is a different type of recorder, not built specifically for low TDE. The performance of the RCA is not known.

For tape utilization, the Newell provides a packing density of 124 kbit/cm<sup>2</sup> (800 bit/in.<sup>2</sup>). The RCA system should be equal to the FR-2100. For bit error rate, one error in 10<sup>5</sup> is estimated for the Newell system. The performance of the RCA machine has not been measured.

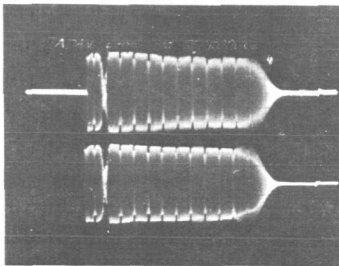
FR-2100  
Video Instrumentation  
Record/Reproduce System

to be delivered JAN., 1971



frequency response

0 ————— 10 MHz



NRZ PCM

16 Mbits/sec

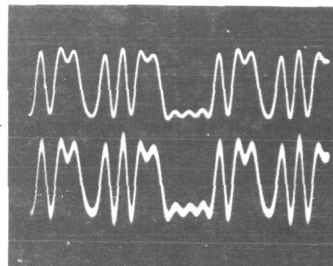


Figure 1

Table 1—Performance evaluation of AMPEX FR-2100.<sup>1</sup>

PERFORMANCE PARAMETERS	DESIGN GOALS 1968	AMPEX FR-2100, VIDEO INSTRUMENTATION RECORD/REPRODUCE SYSTEM PERFORMANCE, SEPT. 1970
a. Freq. response Analog	DC to 10MHz (6MHz - minimum)	DC-10MHz and <u>DC-10MHz</u> (2nd speed) 32
b. PCM Digital System performance	14Mbits/s (11Mbits/s)	16Mbits/s - Test conducted to 20Mbits/s. This was achieved on the 10 MHz bandwidth using Miller Code - PCM.
c. Multi-speed	2 speeds required	Longitudinal speeds-38.1cm/s and 1.19cm/s (15ips and 0.47ips) Scanning speed(rotating head) 50.3 m/s (1980ips) and 1.57m/s (61.9ips)
d. Time Displacement Error (TDE)	25ns min.	Less than 15 ns
e. Tape utilization	116kbits/cm <sup>2</sup> (750 kbits/sq.in.)	85.3kbits/cm <sup>2</sup> (550 kbits/sq.in.)
f. Bit Error Rate	1 Error in 10 <sup>5</sup>	Estimated to be 1 error in 10 <sup>6</sup> . Improvement of 10.
g. Reliability	Dual gap heads	Redundant recording to eliminate tape drop outs. Mfg technology limits this develop't at this time.

*note:* PERSPECTIVE, Ampex FR-600 series recorders used in STADAN have 0.6 MHz. freq. response. The FR-2100 offers more than a 10 to 1 improvement. This also applies to most other parameters.

Table 2—Performance evaluation of three present-day systems.

PERFORMANCE PARAMETERS	AMPEX FR-2100	NEWELL MODEL AV1500R	RCA MODIFIED TR-70
a. Frequency Response	10 MHz	15 MHz Excellent response has non continuous recording. 2,195m (7200') tape has 80 s./pass recording time.	10 MHz Good freq. response should offer competition on new procurements. System demonstrated as lab set-up. Some additional develop't req'd.
b. PCM Digital System	16Mbits/s	20 Mbits/s/channel at 2440cm/s (960ips)	Same as FR-2100
c. Multi-speed	2 speeds	7 speeds 38.10cm/s to 2440 cm/s (15ips to 960ips)	No. Capability was demon. on other system.
d. Time displacement error	Less than 15 ns	3000 ns	?
e. Tape utilization	85.3kbits/cm <sup>2</sup> (550 kbits/sq.in.)	124kbits/cm <sup>2</sup> (800kbits/sq.in.)	Same as FR-2100
f. Bit error rate	1 error in 10 <sup>6</sup>	1 error in 10 <sup>5</sup> Not confirmed	?

## ART/SRT REPORT ON APL

Cyrus J. Creveling

APL (A Programming Language) is an example of a development activity that has been carried out at GSFC with very little cost and which has accomplished a great deal to advance the activity of computer programming and utilization, although it is not strictly speaking, a formal ART/SRT effort. APL was introduced at GSFC by Dr. Edward P. Stabler of Syracuse University during the 1965 summer workshop. At that time, the language existed only as a mathematical notation for the design of computers and computer programs. It was not until a few years later, after a series of two "Higher Order Language Seminars", that we learned of a working APL system on a computer at IBM's Yorktown Heights Research Center. We began an experimental program with that computer, and since then we have interested several hundred people at GSFC in using the language.

This experimental use expanded in 1969 when it was decided to put APL on the T&DS IBM 360/95. After necessary enhancements, this system began operation in mid-1970, and its use has steadily increased since then.

There are presently 10 ports on this computer, and access is available through any of the IBM type-1050 (RITS) terminals dispersed about GSFC. Active efforts are underway to enhance this system further by providing means to input and output magnetic tape from remote locations to APL files and workspaces. The provision of these features will place APL in a position of competing directly with such well-established computer languages as Fortran and Cobol.

## **AUTOMATED DETECTION OF BACTERIA IN URINE**

**Albert J. Fleig  
Grace L. Picciolo  
Emmett W. Chappelle  
Burton N. Kelbaugh**

We have developed a method for detecting the presence of bacteria in urine which may have a substantial impact on present health care procedures. The incidence of urinary tract infections is second only to that of infections of the respiratory system. A large hospital laboratory typically examines up to 4,000 urine specimens a month. The present method of detection is to dip out a drop of urine and spread it on an agar plate (Figure 1). The plate is then capped and incubated for from 1 to 4 days. Then the plate is visually examined (Figure 2) for indication of bacterial growth, and an estimate of the quantity of bacteria present in the original specimen is made. At Johns Hopkins Hospital from four to six medical technicians are occupied full time in performing these assays. It is expensive in terms of trained personnel, space, and time required for an assay. In addition, it is a tedious, repetitive, subjective task subject to much human error.

Our method is derived from work on extraterrestrial life detection done by the former Space Biology Branch. The method utilizes the bioluminescent reaction of adenosine triphosphate (ATP) with luciferin and luciferase derived from the tails of fireflies. All bacteria contain ATP; thus, all bacterially contaminated urine will contain ATP. However, urine samples also contain red and white blood cells and skin cells which also contain ATP. Thus, it is necessary to eliminate all nonbacterial ATP before performing the bioluminescent assay.

A nonionic detergent is added to the urine sample. This detergent lyses or ruptures the cell walls of all the nonbacterial cells but does not affect the bacteria. Then potato apyrase is added, which hydrolizes or destroys all of the ATP, which has been released. Then perchloric acid is added, which inhibits the apyrase and lyses any bacterial cells present in the urine. If (and

only if) there were bacterial cells, free ATP would be present in the specimen, and the injection of luciferase and luciferin will produce a flash of light.

We have developed a device (Figure 3) which completely automates this process and are conducting preliminary trials of it at Johns Hopkins Hospital. An entire assay takes 15 minutes, and the device processes samples at this rate of one per minute. Preliminary test results have been very encouraging. In a run of several hundred specimens, we have correctly detected *every* specimen which was later found positive by the present laboratory procedure. In addition, we found indication of bacterial infection in roughly 20 percent of specimens considered negative by present methods and typically found much higher levels of infection than the present methods do, even when both approaches indicated the presence of infection.

There are several possible explanations for the difference in results from the two approaches. A fundamental difference is that our ATP assay detects bacteria in the specimen as obtained, while culture methods detect only those bacteria which will grow in the particular culture environment being used. Thus, bacteria which do not reproduce on agar, at the pH being used, in contact with oxygen, or for any of a number of other reasons will not normally be found by present hospital methods but would be with our ATP-based assay. Urine may contain bacteriostatic agents, either naturally produced (as might be the case with a low level, long term infection) or as a result of drug therapy. These bacteriostatic agents may preclude detection of the bacteria via routine culture methods but would not hinder the ATP assay. A second basic difference is that we are inferring the presence of bacteria based upon the existence of ATP in the processed urine. Thus, an erroneous positive reading would result if there are sources of ATP which are not deleted by our processing procedure. However, our studies to date indicate that this is not the case.

There are several important potential implications of the ATP assay for patient health care. First, it will be possible to reduce the number of urine specimens which must be cultured by roughly 40 percent by eliminating all specimens with negative ATP assay results, thus, reducing the personnel and space (and ultimately the cost) required for the assay. And it will be possible to return the negative result 1 day sooner which may alter medical treatment, e.g., administration of antibiotics. The device may also make it

possible to screen large numbers of patients in classes with above-normal incidence of bacterial infection, such as teenage girls, pregnant women, and diabetics. The only requirement for the above is that a thorough clinical trial should confirm that the ATP assay does not miss any cases of infection detected by present methods.

The ATP assay also provides information not presently available, and if further trials establish the correctness of our results, this may be even more important. In particular, the ATP assay may correctly detect bacteria which would be missed (or underestimated) by present methods. The ATP assay provides an accurate, replicable quantitative result in place of a subjective estimate. Although the impact of this change is impossible to predict, Lord Kelvin's observation, "...But nearly all the grandest discoveries of science have been but the rewards of accurate measurement and patient long continued labor in the minute sifting of numerical results," may apply.

There are still several steps to be completed before this technology is successfully transferred to the medical community. A thorough clinical trial is required to establish the accuracy and reliability of the assay and to resolve the discrepancies in results between the ATP assay and present standard cultural techniques. Commercial development and marketing of the device will then complete the process. As a result of discussions with the National Institute of General Medical Sciences, NIH, we have prepared a proposal for a clinical trial involving Johns Hopkins Hospital, the NIH Clinical Center, and GSFC. Several commercial firms have expressed interest in marketing the device if the clinical trials are successful.

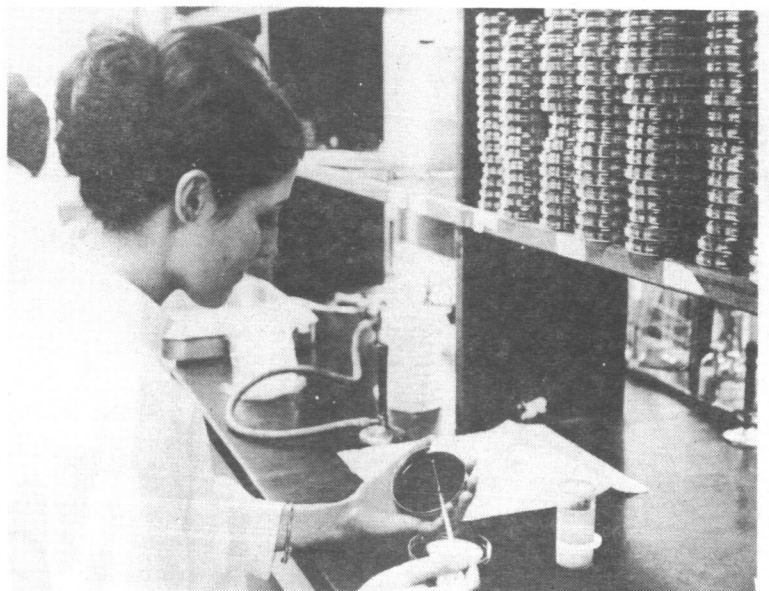


Figure 1



Figure 2

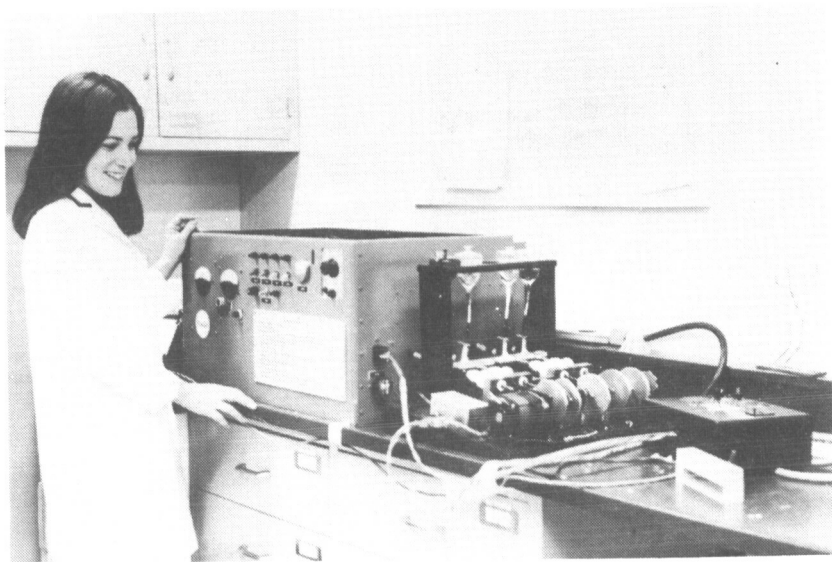


Figure 3

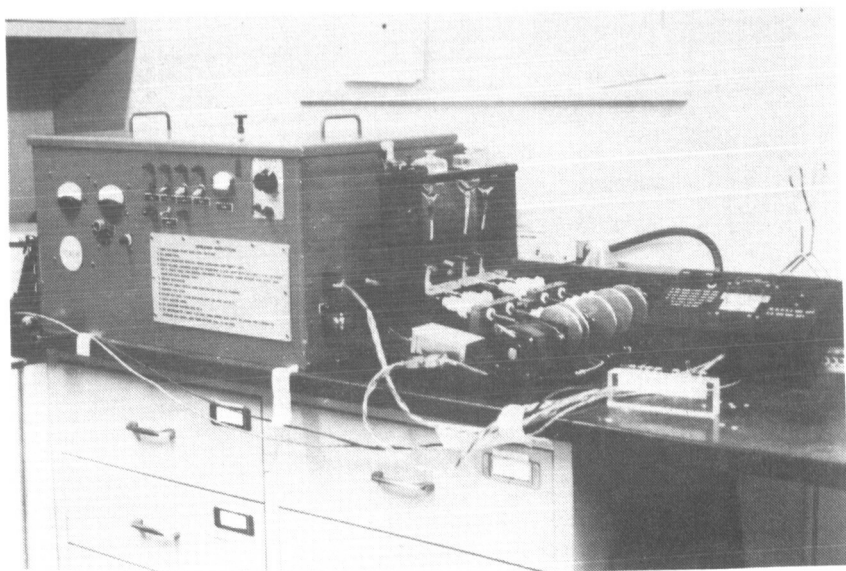


Figure 4

## THE HEART SOUND PREPROCESSOR

Wayne T. Chen

Man's concern with the health of his heart is unending, whether he journeys to the Moon or through the daily, ubiquitous traffic on his way home from work. Some improvements and innovations in bio-instrumentation have emanated from recent scientific developments in our space endeavors.

For example, the technology developed for signal and data processing has been applied to improving diagnostic techniques in the area of phonocardiography (PCG), the graphic recording of the sounds of the heart generated by the functioning of the aortic and ventricular valves. The implementation of an automatic PCG signal processing system is enhanced if the signal can be treated in the same manner as other physiological signals. With this in mind, the relatively broad bandwidth of the PCG signal (20 to 2,000 Hz) has been reduced to less than 100 Hz by the use of a heart sound envelope. The circuit transforms positive and negative PCG signals to an all positive signal, the amplitude of which is proportional to intensity. Such transformation results in a visual representation of sounds and their temporal relations similar to the aural impression of the ear. Diagnostic information related to intensity and timing is retained. The transformed signal has been obtained by full-wave rectification of the PCG signal, envelope detection of the rectified wave, and low pass filtering of the resultant envelope. This is graphically illustrated in Figure 1.

Figures 2 and 3 show examples of this process. The top trace in Figure 2 represents the frequency response of the microphone used to obtain the heart sound, and the bottom trace represents the same signal after being channeled through the preprocessor. (The traces in Figure 3 are reversed.) Figure 2 shows a normal heart, and one can see that the pattern is very symmetric and smooth, each peak representing the proper closing of a valve. The second heart pattern (Figure 3) is similar to the first. However, note the split or cusp at the peak of this pattern. This represents a split heart sound and may indicate trouble in valve closure. As one can see, if we

were to rely solely on the audio representation of this heart sound, it would be very difficult to detect this condition.

The advantages of our approach are (1) the signal eliminates sometimes false interpretations based on attempts to analyze frequency content of the phonocardiogram, (2) reduced bandwidth requires less computer core storage, (3) simpler signal pattern recognition programing techniques can be employed, and (4) quantitative rather than qualitative information may now be obtained and recorded for more objective interpretation. The low cost and small size of components make this device feasible for incorporation with a heart sound microphone as the input to a physiologic data acquisition system.

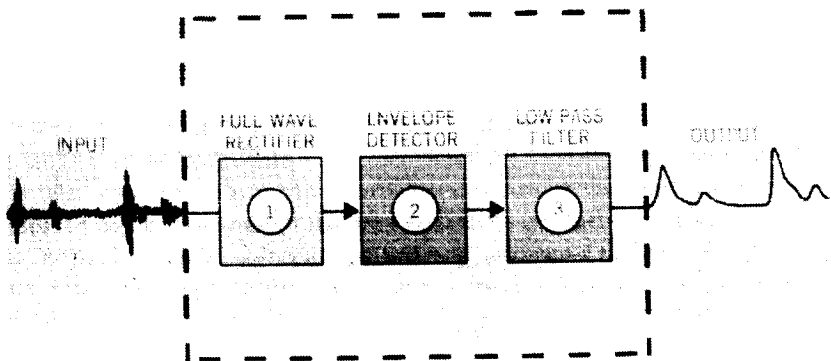


Figure 1--Heart sound preprocessor.

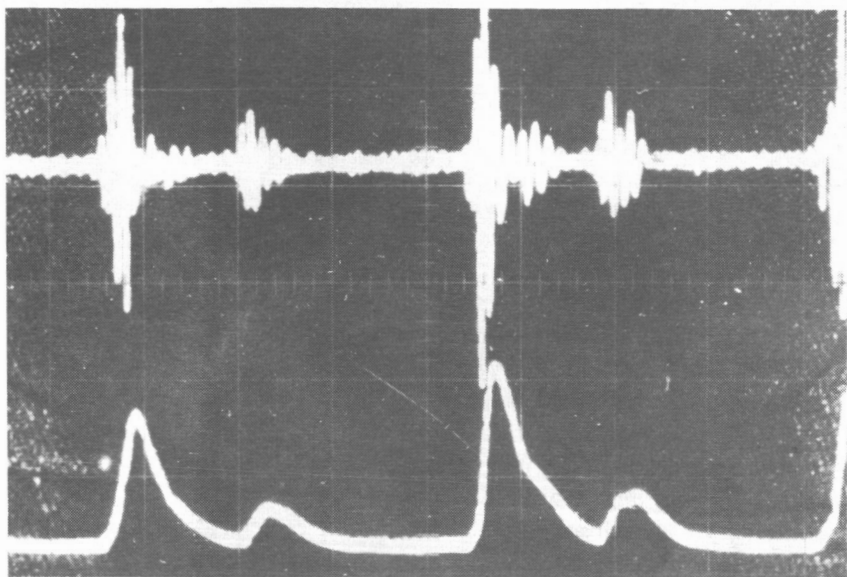


Figure 2

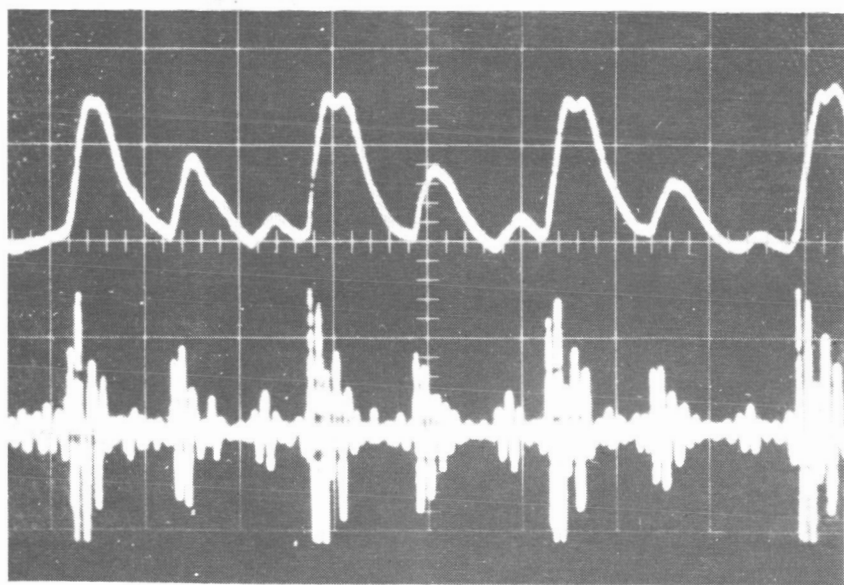


Figure 3

## LONG RANGE LASER TRAVERSING SYSTEM

Louis O. Caudill

In December 1968, the U.S. Forest Service approached Goddard Space Flight Center to see if NASA-developed laser technology could be applied to the problems involved in surveying land in areas where the direct line of sight between property corners located on one mile centers is obscured by various types of obstacles, such as terrain or vegetation. As an indication of the magnitude of this requirement, the U.S. Forest Service controls 270,000 miles of property lines consisting of more than 1,000,000 property corners, the majority of which are located on one mile centers. Maintaining these property lines requires a never-ending program of land survey. The Forest Service estimates that an instrument with a range capability of one mile and an azimuth accuracy of  $\pm 1$  minute of arc will support 95 percent of their surveying requirements at a savings in excess of \$100.00 per mile in cost.

In support of the U.S. Forest Service request, a study was carried out to determine if the concept of detecting optical scatter from a vertically oriented laser beam with a portable receiver system located up to a mile away was theoretically feasible, and if feasible, could a laser transmitter and receiver be built that would be man-portable and meet our theoretical requirements such as power output and receiver detectability. The results of the study verified the feasibility of a system which would be both man-portable and capable of detecting the optical scatter due to molecular and aerosol constituents of the atmosphere from a vertical laser beam.

Figure 1 shows the basic concept of the system. The laser transmitter, located up to one mile from the receiver, is aligned to the local gravity vertical by the use of precision bubble levels attached to the unit. The receiver is set up on a reference corner, leveled, and pointed in the direction of the laser beacon specified by compass data. The receiver is elevated to clear terrain obstacles and the transmitter is commanded to fire either upon command of the receiver operator via a radio link or in a continuous 1/5-s mode. The receiver then begins an azimuth search until the beacon is

detected. The receiver is then aligned to the laser beacon using the azimuth sensing capability built into the receiver system.

Figure 2 shows the laser transmitter and receiver units of our prototype surveying system. The laser vertical beacon consists of a ruby laser system with an energy output in excess of 150 mJ and an angular divergence of less than one mrad. The narrowness of the laser beam is basic to our azimuth accuracy. This laser divergence represents a beam width of 30.5 cm at an altitude of 457.5 m. The unit is powered by a 28-V battery pack at a maximum rate of one pulse every five seconds.

The receiver system is a modified DKM-3A astronomical theodolite with a basic instrumental accuracy of less than 0.5 arc seconds. The unit has a 2.83 arc-second optical aperture and a 50.8-cm focal length. The unit shown has an acquisition field of  $\pm 20$  arc minutes and an azimuth sensing accuracy of  $\pm 0.5$  arc minutes at a range of one mile and a receiving elevation angle of 45 deg.

The system shown in Figure 2 has been operated in the field under a variety of daylight conditions. The tests were run with the beacon and receiver separated by approximately one mile. The system was consistently able to detect the laser signal regardless of background conditions.

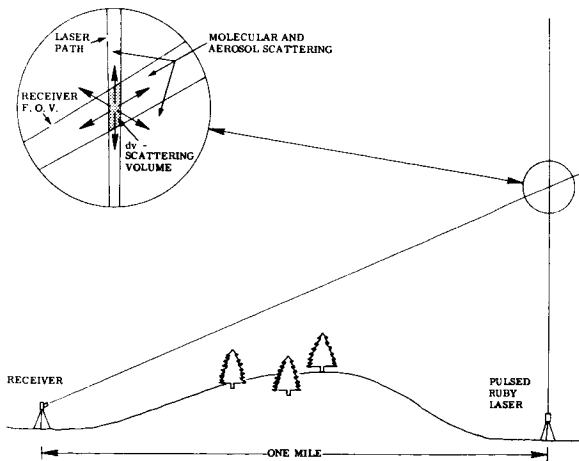
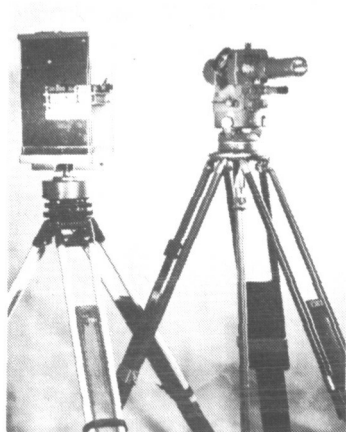


Figure 1—Laser traversing system.



## LASER TRANSMITTER

POWER OUTPUT	0.15 J
OPTICAL WAVELENGTH	6943 Å
PULSE LENGTH	≤20 ms
PULSE RATE	12/min MAX
DIVERGENCE	$0.75 \times 10^{-3}$ rad
POWER INPUT	28 V dc
WEIGHT—LASER	10.80 kg
BATTERIES	6.75 kg
TRIPOD	10.35 kg
TOTAL	27.90 kg

## RECEIVER

OBJECTIVE APERTURE	2.83"
FOCAL LENGTH	50.8 cm
ACQUISITION FOV	40'
OPTICAL BW	8 Å
SENSITIVITY OF LEVELS	10"/mm
INSTRUMENT ACCURACY	0.5'
WEIGHT—RECEIVER	11.25 kg
ELECTRONICS	4.50 kg
BATTERIES	6.75 kg
TRIPOD	9.00 kg
TOTAL	31.50 kg

Figure 2—Prototype surveying system.

## **USING THE SCANNING ELECTRON MICROSCOPE ON THE PRODUCTION LINE TO ASSURE QUALITY SEMICONDUCTORS**

**John W. Adolphsen  
and  
Robert J. Anstead**

Metallization defects introduced during batch processing of semiconductor devices have been a major problem in several GSFC flight projects in recent years. Partial discontinuities in metallization at the step in the oxide at contact windows (Figure 1) have resulted in latent failures in systems already fabricated and tested. This condition cannot be detected with an optical microscope (Figure 2). The line at the oxide step is typical of that normally seen for a good device, but here the metallization is almost completely discontinuous. By contrast, Figure 1, which is a scanning electron microscope (SEM) picture, shows that the line is not a shadowing effect and clearly describes the actual condition of the metallization.

Defects like this are not confined to a single vendor, a single point in time, or a particular device type, but rather to small geometry contact windows in both discrete transistors and integrated circuits. Users have been penalized not only by suffering latent in-system failures, but also by the eight- to nine-month procurement and delivery cycle (for devices built to high reliability specifications), with no assurance that a replacement order—or its successor—will be free of this defect.

Although the SEM is capable of detecting this metallization anomaly, its use heretofore has been confined to the laboratory. A method of determining metallization integrity has been developed that culminates in a procurement specification, which uses the SEM on the production line as a quality control tool. Batch process control of the metallization operation is monitored early in the manufacturing cycle. When bad metallization is detected, lost time is reduced to about five weeks from the 30 weeks necessary for complete manufacturing and screening tests. A paramount requirement of the method was that the disturbance to vendors' normal process flows be minimal.

There are a number of key points to the specification:

**Metallization Inspection**—The SEM is the instrumentation used to examine metallization on samples. Critical viewing parameters are specified, including magnification at 6000X and proper positioning of the sample relative to the incident electron beam.

**Sampling**—A typical single metallization run of 20 to 30 slices may yield potentially 300,000 transistor dice. Normal sampling techniques would require a sample size of over a thousand dice to be examined, but this is impractical for the SEM. Instead, since this is a batch process detection method, 15 to 25 dice are selected from specific sites in the metallization chamber. The exact number and sites are determined by order size, die size, geometrical configuration of the slice holder in the metallization chamber, number and type of metallizing source elements, and static or dynamic position of the slice holder relative to the source(s).

**Metallization Quality Evaluation**—Written and pictorial standards constitute the acceptance/rejection criteria. Judgment of metallization quality is based on many examples of good (Figure 3), bad (Figure 1), and marginal (Figure 4) metallization.

It has been demonstrated that the method is practical, its details have been worked out, and it is acceptable to vendors. It is also operational, since semiconductors have been bought to the specification. Finally, its use is being extended, as shown by current efforts to incorporate it into the Department of Defense General Specification for Micro-electronics, Mil-M-38510. Thus, the user can be assured that the type of anomaly discussed here will not be present in devices built to this specification.

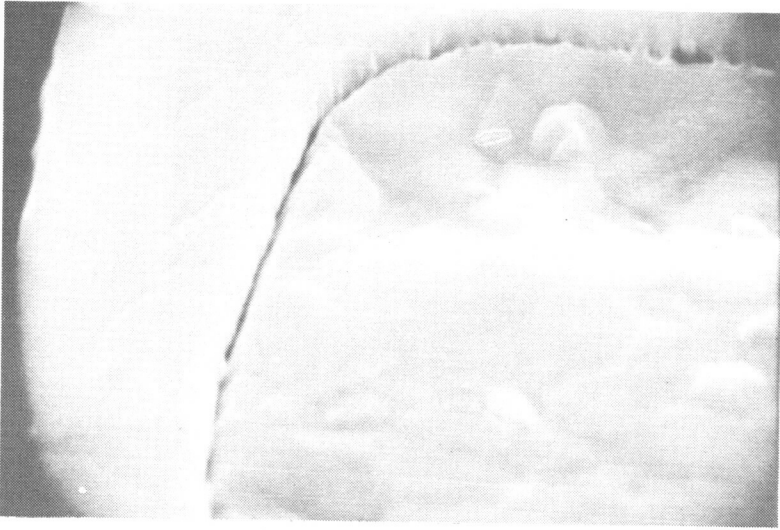


Figure 1—SEM picture of edge of contact window. Magnification is 5000X.

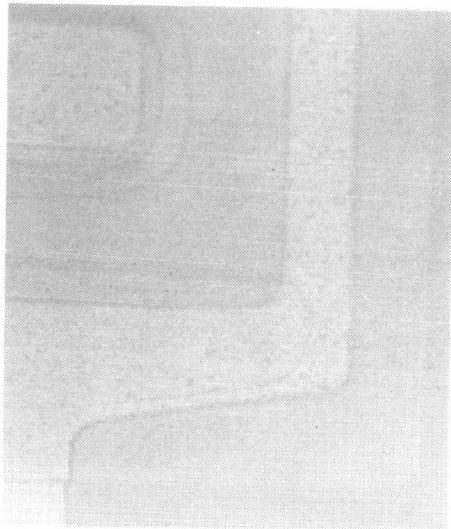


Figure 2—Optical microscope picture of transistor contact window. Metallization at  $S_1O_2$  step appears good but is discontinuous. Magnification is 400X.



Figure 3—SEM picture of good metallization. Aluminum at oxide step is smooth and continuous. Magnification is 5500X.

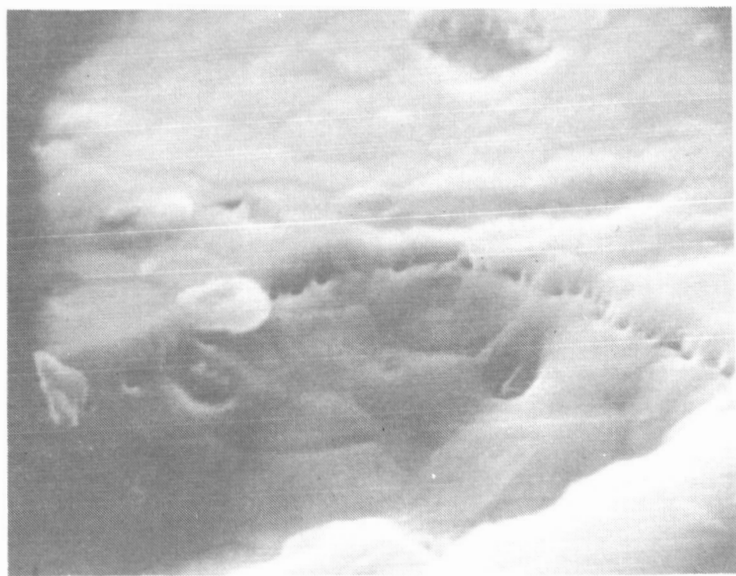


Figure 4—SEM picture of marginal metallization. A borderline case because of the number of discontinuities in aluminum at oxide step. Magnification is 5500X.

## ULTRAPRECISION TOOL POSITIONER

Ewald E. Schmidt

The original objective of the tool positioner program was to develop a linear displacement actuator for the generation of optical elements in highly stable materials. It is evident that a positioner developed for such purpose will also be suitable for actively controlling the figure of a lightweight astronomical mirror since both applications require high sensitivity and a high degree of repeatability.

While positioners that are accurate to within one-tenth of a wavelength\* have been developed, they suffer from a common disadvantage—the effective range of these positioners is limited to a few wavelengths.\* The problem then was to design a linear actuator with a range of several centimeters and more. The solution was to combine two independently functioning devices and form an improved tool positioner (Figure 1). This positioner includes front and rear sliding holders in addition to an incremental driver. Each of the two sliding holders can be independently restrained from moving along the base track by a locking mechanism, which can be, depending on the application, piezoelectric, electromagnetic, or mechanical in origin. In our unit, it is electromagnetic. By alternate locking and unlocking of the sliding holders and sequential operating of the piezoelectric incremental driver, motion of the tool positioner comparable to the movements of a caterpillar is achieved.

The advantages of this positioner over other displacement actuators are

- (1) Simplicity of construction—dimensional tolerances can be met without expensive instrumentation.
- (2) Large displacement range, which is only limited by the length of the base track.

---

\*6328 Å Ne<sup>20</sup> laser radiation.

(3) Bidirectional displacement, so that the motion of the positioner can be reversed from push to pull.

(4) Ability to work against opposing force, so that various loads can be supported by this particular positioner by varying the current applied to the electromagnets.

During calendar year 1970, an engineering model positioner was manufactured and tested. The tool positioner system includes an electronic switching circuit and a laser interferometer gage. Figure 2 shows the response of the positioning device under a 1.0-kg load. The slanted curve represents that portion of a cycle in which the incremental driver advances under a voltage increase from 0 to 900 V dc. The vertical curve reflects the behavior of the positioning device during the switchover in which the locking sequence of the holders is reversed and the voltage applied to the incremental driver drops from 900 to 0 V dc. This recycling is performed automatically by a control device at a rate up to 10 Hz. Fine positioning sensitivity is presently limited to one-eighth wavelength, which is the measuring accuracy of the laser interferometer used with this experiment.

Figure 3 shows the performance of the positioner under varying loads: no load, 0.5 kg, and 1.0 kg, over a range of about 55  $\mu\text{m}$ . The curves shown in this figure were also plotted from data acquired through the laser interferometer readout when it was operated in the manual mode. Displacements shown are those for each complete cycle. A total of 11 cycles were plotted; the range of this device, of course, is only limited by the length of the base track.

It has been demonstrated that, by combining a holding mechanism and a driving mechanism, the capabilities of an otherwise limited positioning device can be greatly extended. Displacements of more than 5 cm are possible with a sensitivity of better than  $7 \times 10^{-8}$  m. The device has an opposing force capacity of 1 kg, which can be further increased depending on the application; it is bidirectional and simple in construction.

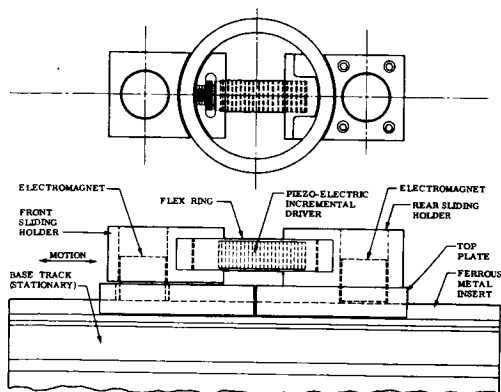


Figure 1—Positioner components.

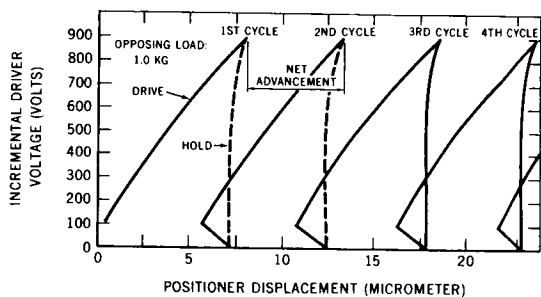


Figure 2—Cyclic variation as a function of holding and drive operation.

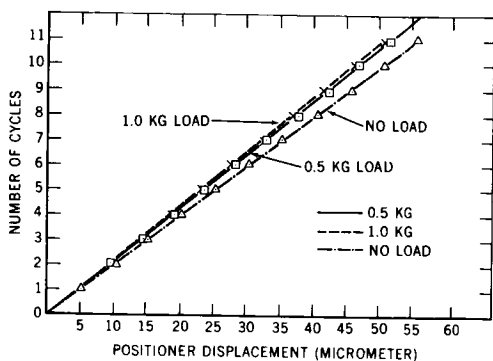


Figure 3—Positioner performance under various loads.

NATIONAL AERONAUTICS AND SPACE ADMINISTRATION  
WASHINGTON, D.C. 20546

OFFICIAL BUSINESS  
PENALTY FOR PRIVATE USE \$300

FIRST CLASS MAIL

POSTAGE AND FEES PAID  
NATIONAL AERONAUTICS AND  
SPACE ADMINISTRATION



POSTMASTER: If Undeliverable (Section 158  
Postal Manual) Do Not Return

*"The aeronautical and space activities of the United States shall be conducted so as to contribute . . . to the expansion of human knowledge of phenomena in the atmosphere and space. The Administration shall provide for the widest practicable and appropriate dissemination of information concerning its activities and the results thereof."*

— NATIONAL AERONAUTICS AND SPACE ACT OF 1958

## NASA SCIENTIFIC AND TECHNICAL PUBLICATIONS

**TECHNICAL REPORTS:** Scientific and technical information considered important, complete, and a lasting contribution to existing knowledge.

**TECHNICAL NOTES:** Information less broad in scope but nevertheless of importance as a contribution to existing knowledge.

**TECHNICAL MEMORANDUMS:** Information receiving limited distribution because of preliminary data, security classification, or other reasons.

**CONTRACTOR REPORTS:** Scientific and technical information generated under a NASA contract or grant and considered an important contribution to existing knowledge.

**TECHNICAL TRANSLATIONS:** Information published in a foreign language considered to merit NASA distribution in English.

• **SPECIAL PUBLICATIONS:** Information derived from or of value to NASA activities. Publications include conference proceedings, monographs, data compilations, handbooks, sourcebooks, and special bibliographies.

**TECHNOLOGY UTILIZATION PUBLICATIONS:** Information on technology used by NASA that may be of particular interest in commercial and other non-aerospace applications. Publications include Tech Briefs, Technology Utilization Reports and Technology Surveys.

*Details on the availability of these publications may be obtained from:*

SCIENTIFIC AND TECHNICAL INFORMATION OFFICE  
NATIONAL AERONAUTICS AND SPACE ADMINISTRATION  
Washington, D.C. 20546